Aerosol Assisted Synthesis of Nanostructured Silica

Proefschrift

ter verkrijging van de graad van doctor
aan de Technische Universiteit Delft,
op gezag van de Rector Magnificus prof. dr. ir. J.T. Fokkema,
voorzitter van het College voor Promoties,
in het openbaar te verdedigen op dinsdag 13 mei 2008 om 12:30 uur

door

Raghuraman PITCHUMANI

Master of Technology in Process Engineering and Design
Indian Institute of Technology (IIT), Delhi

geboren te Hyderabad, India.

Dit proefschrift is goedgekeurd door de promotoren:
Prof. dr. ir. M.-O. Coppens
Prof. dr. sc. tech. A. Schmidt-Ott

Samenstelling promotiecommissie:

Rector Magnificus	Technische Universiteit Delft, voorzitter
Prof. dr. ir. M.-O. Coppens	Technische Universiteit Delft, promotor
Prof. dr. sc. tech. A. Schmidt-Ott	Technische Universiteit Delft, promotor
Prof. dr. A. Sayari	University of Ottawa
Prof. dr. ir. K. P. de Jong	Universiteit Utrecht
Prof. dr. F. Kapteijn	Technische Universiteit Delft
Dr. ing. J. J. Heiszwolf	Albemarle Catalysts B.V.
Dr. ir. J. C. M. Marijnissen	Technische Universiteit Delft
Prof. dr. S. J. Picken	Technische Universiteit Delft, reservelid

ISBN: 978-90-9023028-3

To Amma, Appa
and
my late grandmother

Preface

In view of increasing energy demands, one of the most important industrial processes is fluid catalytic cracking (FCC), which breaks down heavier oil fractions into more desirable light fractions, including gasoline and olefins. An FCC unit is part of a traditional oil refinery, but also plays a major role in refineries based on other feedstocks, including renewable ones like biomass. As crude oils become heavier and feedstocks more complex, the FCC process will only rise in importance.

The catalyst is the heart of the FCC process, and is, not surprisingly, quite remarkable in itself. The severe conditions encountered in the process (800 °C, steam) make it essential that it possesses tremendous hydrothermal stability, and retains its activity over extended periods of operation. For about half a century, the major active component of an FCC catalyst has been a zeolite.

Zeolites are microporous aluminosilicates. They occur in nature, and have been known for about 250 years. However, their naturally occurring forms are, at present, of limited value, due to presence of undesired impurities. They are not optimized for catalytic applications either. It was only with the advent of synthetic zeolites, from 1948 on, that this class of porous materials began to play an important role in catalysis. Some of these synthetic zeolites exhibit unique properties with respect to both activity and selectivity. Activity is mostly determined by the Brønsted and the Lewis acid sites, and by metals that may be incorporated. Selectivity is guided by the zeolite micropores that may range in size from 3 Å to more than 12 Å. The introduction in 1962 of synthetic faujasites (zeolites X and Y) on an industrial scale in fluidized catalytic cracking of heavy petroleum distillates was a landmark innovation [1]. The new zeolite catalysts were orders of magnitude more active than the amorphous silica-alumina catalysts, and also brought about a significant increase in the yield of gasoline, the most valuable product from FCC units. It was estimated that this yield enhancement alone accounts for an added value on the order of several billions of US dollars per year, which can be attributed to zeolite catalysts [2]. Apart from oil refining and petrochemistry, the application of zeolites in environmental catalysis and fine chemical synthesis is also steadily increasing [3-5].

Despite these broad applications and advantages, the micropores of the zeolites may in some cases limit the catalytic performance of zeolites. The reason is the restricted molecular transport inside the crystals, induced by the similar size of the diffusing hydrocarbons and the micropore diameter. This becomes even more severe when the reacting molecules are bulky, as in the case of FCC, resulting in lowered activity and undesirable coke formation, leading to blockage of the pores and a reduction of the available active surface area. This requires us to address the issue of accessibility. One way to minimize the diffusion limitations is the reduction of the intracrystalline diffusion path length. Hereby, reactants can enter and reaction products are released more rapidly. Furthermore, the increased number of micropore entrances per gram of zeolite (increased external zeolite surface area) should also result in increased activity [6].

An alternate way to prepare materials with enhanced accessibility would be to design materials with pore network architectures composed of both micropores and mesopores, or, in other words, to introduce hierarchical porosity. The IUPAC classifies pores on the basis of their size as micropores ($<$ 2 nm), mesopores (between 2 and 50 nm) and macropores ($>$ 50 nm). An optimal network of micropores, mesopores and macropores reduces transport limitations of reactants and products, resulting in high reaction rates.

The discovery in 1992 by researchers at Mobil Oil of ordered mesoporous materials, which they named MCM-41 [7], opened a new direction to tackle the problem of diffusion limitations encountered in reactions. MCM-41 is synthesized using the cationic surfactant cetyl trimethyl ammonium bromide (CTAB) as the structure-directing agent. The resulting materials contain a hexagonal array of uniform channels around 3 nm in diameter, with extremely high surface areas above 700 m^2/g. Even though it is possible to expand the pore size using different swelling agents, such as TMB, the relatively thin pore walls of MCM-41 hinder their hydrothermal stability. In 1998, Stucky and co-workers synthesized a mesostructured silica material, termed SBA-15 [8], using a tri-block co-polymer, P123 ($EO_{20}PO_{70}EO_{20}$; EO is ethylene oxide, PO is propylene oxide) as structure-directing agent. SBA-15 materials have special features, such as large mesopores and a relatively high hydrothermal stability owing to their thick pore walls, making them particularly attractive as heterogeneous catalyst supports. The sol-gel synthesis of these mesoporous materials involves silica-surfactant self-assembly. The materials can be tuned in a variety of morphologies, depending on the synthesis conditions. Experiments are usually carried out in a batch reactor, and require several days to obtain the ordered materials. Furthermore, due to the batch nature of the synthesis, the final product morphology is often irregular.

An aerosol driven process could address the above issues. Evaporation induced self-assembly (EISA) has been utilized to produce nanostructured materials as thin films, using a rapid dip-coating or spin-coating process, during which solvent evaporation enriches the concentration of silicate and surfactant, inducing co-assembly into mesostructured, defect-free surfactant-silicate thin films [9]. This concept was combined with aerosols by Brinker and co-workers [10], who proposed an aerosol driven EISA process to continuously synthesize solid, well-ordered spherical particles with stable pore mesostructures of hexagonal and cubic topology, as well as layered (vesicular) structures, using different structure-directing agents. This process allows the synthesis of nanostructured materials in a process time of several seconds, much shorter than the conventional sol-gel approach. The EISA route combines the simplicity of the sol-gel process with the efficiency of surfactant self-assembly, allowing rapid synthesis of mesostructured thin films, particles, and arrays with controlled morphology and mesostructure [11]. The process is continuous and scalable making it industrially attractive and viable. Particles can be synthesized over a wide size range by controlling the operating conditions. The particles are generally spherical, which frequently has advantages for subsequent powder handling and processing. The non-equilibrium feature of the EISA process allows the incorporation of various non-volatile components, such as functional organic molecules, particles and polymers within the self-assembled mesostructures, providing a general and flexible approach for nanocomposite fabrication [12]. An interesting feature from the perspective of material synthesis is that the method enables uniform incorporation of the chemical species (that can be dissolved or dispersed into a precursor solution) into every synthesized particle.

The main goal of this thesis is to synthesize mesoporous silica supports using the continuous aerosol driven EISA method, which could be candidates for catalytic applications requiring enhanced transport, mainly for use in FCC catalysis. Due to the high hydrothermal stability of SBA-15, we utilized its structure directing agent, block co-polymer P123 ($EO_{20}PO_{70}EO_{20}$), for synthesizing these nanostructured materials. This led us to first investigate and familiarize ourselves with the sol-gel synthesis of mesoporous silica, and we present interesting results on this subject in the first two chapters. The outline of the thesis is as follows.

Chapter-1 describes nanostructured, mesoporous SBA-15 synthesized in the presence of a weak acid, H_3PO_4. The uniqueness of the materials was observed through the broad variety of morphologies that could be generated by tuning a single parameter, namely the stirring rate during the low temperature hydrothermal treatment. Morphologies in the form of free standing films (at the air-liquid interface) and a hierarchical porous cake under static conditions were observed. Long bundles composed of threads joined together were obtained under slow stirring conditions, while short fibers were obtained under fast stirring. These mesoporous materials had a high surface area and well ordered, uniform pores.

Chapter-2 investigates the diffusion properties of the fibers and bundles of SBA-15 using Pulsed Field Gradient (PFG) NMR measurements. The structural differences in the morphologies of these distinct samples could be observed in the transport behaviour of the diffusing molecules used in the study. The diffusion coefficients were determined in both principal directions: parallel to the mesopore channels, and in a direction perpendicular to them. Using this data it was possible to observe distinct diffusive properties that well matched the internal structure and the external morphology of these nanostructured materials.

Chapter-3 gives an account of the development of the aerosol equipment for continuous synthesis of nanostructured silica. The chapter details the different atomizers used in this study, namely the ultrasonic atomizer, the TSI 3076 atomizer and the Collison atomizer for generation of aerosols from a liquid precursor. Furthermore, a tubular reactor was also fabricated in-house, where the liquid aerosol is transformed into the final product, which is collected on a membrane filter. All the equipment parts were required to be retrofitted/modified in-house to satisfy the experimental needs and overcome any problems faced to ensure a smooth functioning of the aerosol equipment.

A preliminary study on the synthesis of mesoporous silica using the aerosol process is described in Chapter-4. This Chapter discusses initial synthesis experiments of mesoporous silica particles, performed using different atomizers, and using organosilicate precursors and P123 as a templating agent.

Chapter-5 handles the aerosol assisted synthesis of nanoporous silica in greater detail. The synthesis in general involves a large number of experimental parameters. In order to explore this high dimensional experimental space, a factorial design of experiments was employed to study the effect of important variables, namely the precursor composition and the tubular reactor temperature, on the textural properties of the final product. A rigorous statistical methodology was employed to identify the significant variables, in other words to narrow down to those variables which have the maximum effect on the BET surface area and total pore volume of the products. Furthermore, a regression analysis was performed to quantify the effect of these variables on the texture of the final particles, and the results were represented in the form of contour plots.

Chapter-6 deals with the synthesis of mesoporous silica-alumina materials using industrial raw materials. With the help of a laboratory spray drier, nanosized silica and alumina were assembled using P123 as a templating agent. The resultant mesoporous silica-alumina materials exhibited remarkable stability under severe steaming conditions. The activity of these samples was also investigated using pulse probe molecule experiments.

The extension of the aerosol process to produce mesoporous ZSM-5 composites is presented in Chapter-7. This first involved the synthesis of nanosized ZSM-5 particles using a batch sol-gel scheme. These nanocrystals were then incorporated into a mesoporous silica framework (templated by the non-ionic surfactant, P123), resulting in a mesoporous ZSM-5 composite. These composites with a hierarchical porous structure (micro- and mesoporosity) are interesting candidates for the catalytic cracking of bulky molecules.

References

1. J. Weitkamp, Solid State Ionics 131 (2000) 175.
2. J. E. Naber, K. P. de Jong, W.H.J. Stork, H. P. C. E. Kuipers, M.F.M. Post, in: J. Weitkamp, H.G. Karge, H. Pfeifer, J. Hlderich (Eds.), Zeolites and Related Microporous Materials: State of the Art 1994, Studies in Surface Science and Catalysis, Vol. 84, Elsevier, Amsterdam, 1994, p. 2197, Part C.
3. A. Corma, Chem. Rev. 95 (1995) 559.
4. C. Perego, P. Ingallina, Green Chem. 6 (2004) 274.
5. J. Ĉejka, B. Wichterlová, Catal. Rev. 44 (2002) 375.
6. S. van Donk, A. H. Janssen, J. H. Bitter, K. P. de Jong, Catal. Rev. 45 (2003) 297.
7. J. S. Beck, J. C. Vartuli, W. J. Roth, M. E. Leonowicz, C. T. Kresge, K. D. Schmitt, C. T-W. Chu, D. H. Olson, E. W. Sheppard, S. B. McCullen, J. B. Higgins, J. L. Schlenkert, J. Am. Chem. Soc. 114 (1992) 10834.
8. D. Zhao, J. Feng, Q. Huo, N. Melosh, G. H. Fredrickson, B. F. Chmelka, G. D. Stucky, Science 279 (1998) 548.
9. Y. Lu, B. F. McCaughey, D. Wang, J. E. Hampsey, N. Doke, Z. Yang, C. J. Brinker, Adv. Mater. 15 (2003) 1733.
10. Y. Lu, H. Fan, A Stump, T. L. Ward, T. Rieker, C. J. Brinker, Nature 398 (1999) 223.
11. J. E. Hampsey, S. Aresnault, Q. Hu, Y. Lu, Chem. Mater. 17 (2005) 2475.
12. Y. Lu, H. Fan, N. Doke, A. D. Loy, R. A. Assink, D. A. LaVan, C. J. Brinker, J. Am. Chem Soc. 122 (2000) 5258.

Raghuraman Pitchumani

Contents

List of Figures

List of Tables

Chapter 1

Tuning of Nanostructured SBA-15 Silica using Phosphoric Acid

1.1 Introduction

SBA-15 is a mesoporous SiO_2 with a hexagonal arrangement of channels with diameters in the range of 5-30 nm [1]. Its advantages include high thermal stability and relatively thick silica walls with a network of micropores and/or mesopores in the walls in addition to well-ordered mesopores. The porosity of the walls depends on parameters such as the synthesis temeperature [2,3]. SBA-15 is synthesized using a non-ionic surfactant P123 (block co-polymer $EO_{20}PO_{70}EO_{20}$, where EO is ethylene oxide and PO is propylene oxide) in the presence of strong acids like HCl. The critical micelle concentration of P123 in pure H_2O is 0.03 w/v % at 25 °C [4]. It has been observed that the addition of ethanol to the system decreases the size of the micelles [5,6].

Since the pioneering work reported by researchers at Mobil [7], such surfactant templated mesoporous materials have found several applications in catalysis, gas sensing, separation and optics [8]. The synthesis process of mesoporous materials like SBA-15 involves the formation of organic-inorganic composites by a self-assembly process, where the organic phase is organized on a mesoscopic scale and serves as a template for the inorganic component. Different mesostructures and pore sizes can be obtained by adjusting the synthesis conditions and nature of the surfactant. Mesoporous materials in the form of films [9], monoliths [10], spheres [11], rod-like structures [12], fibers [13] and crystals [14] have been obtained in block co-polymer templating systems. Mesoporous films have been grown at air-water and mica-water interfaces through an interfacial silica-surfactant self-assembly process [15,16]. Zhao *et al.* [17] reported the formation of continuous mesoporous silica films with large periodic cage and pore structures using poly-(ethylene oxide) non-ionic surfactants as structure directing agents in a dip-coating

---

This chapter is based on the following publications:
R. Pitchumani, W. Li, M.-O. Coppens, Catalysis Today 105 (2005) 618.
R. Pitchumani, W. Li, M.-O. Coppens, Stud. Surf. Sci. Catal. 156 (2005) 83.

process. The films exhibited high thermal stability upon calcination at 450 °C and were crack free for a thickness less than 1 µm. The thickness of the film was varied uniformly by adjusting the dip-coating rate or the coating solution concentration. These mesostructured films might find use, in addition to catalysis, as membranes for biomolecular separations, sensors, ordered ceramic matrix composites and mesostructured composites [15]. Highly ordered mesoporous SBA-15 fibers over hundreds of microns in length, with a uniform diameter, were grown using tetra-methyl orthosilicate (TMOS) under acidic conditions [11]. Ordered and optically transparent mesoporous silica fibers were synthesized in a two-phase system at room temperature and have been demonstrated to have potential as high-surface area optical waveguides [18]. Yang *et al.* [13] employed a simple process for making mesoporous fibers with large and accessible pores. These fibers were uni-axially aligned and possessed either 3D hexagonal cage or 2D hexagonal channel structures.

In the present study, we utilize a simple approach to selectively synthesize unique morphologies of SBA-15 from a mixture that is similar to the one conventionally used [1], except that it includes a weak acid H_3PO_4 instead of the strong acid HCl. By simply controlling the stirring rate, shapes of a broader variety than when using HCl are obtained from an identical starting mixture.

1.2 Experimental

1.2.1 Material Synthesis

A sol-gel process was employed to produce the materials. Different samples were prepared from the same initial aqueous solution. 3.0 g of Pluronic P123 were dissolved in 5.0 g of phosphoric acid (85 wt.%) and 60 ml of deionized water at 40 °C to obtain a clear solution. 8.0 ml of tetra ethyl orthosilicate (TEOS) was quickly added to this mixture, while stirring at 40 °C with a magnetic stirrer. Excess water was added to make up the solution to 80 ml. The molar composition of the starting solution was TEOS : P123 : H_3PO_4 : H_2O = 1.0 : 0.015 : 1.23 : 111.1.

Three sets of experiments were performed. In the first set, stirring (at 500 rpm) was stopped 2 minutes after the addition of TEOS and the mixture was subsequently kept under static conditions at 40 °C for 48 h. In the second and third set of experiments the solution was stirred, either vigorously (423 rpm) or slowly (134 rpm) at 40 °C for 24 h. The solid products obtained from the three batches were transferred to autoclaves and aged at 100 °C for 24 h. The resulting products were recovered by filtration, washed with deionized water, and dried in an oven at 80 °C. To remove the organic template, the samples were calcined at 250 °C for 3 h and then at 550 °C for 7 h using a heating rate of 5 °C/min.

1.2.2 Material characterization

Powder X-ray diffraction (XRD) patterns of products obtained from the first set of experiments were recorded using a Bruker-AXS D5005 diffractometer with a Co Kα X-ray source (λ_{Co} = 0.179026 nm). XRD patterns of products produced from the other sets were recorded using a

Bruker-AXS D8 Advance X-ray diffractometer equipped with a Vantec position sensitive detector using Co Kα radiation (λ_{Co} = 0.179026 nm). Scanning electron microscopy (SEM) images were obtained with a JEOL JSM-6500F microscope. Transmission electron micrographs (TEM) were recorded using a Philips CM30T electron microscope with a LaB_6 filament as the electron source, operated at 300 kV. Samples were mounted on a microgrid carbon polymer, which was fixed on a copper grid. A specimen of the film was prepared by an ultrathin microtoming method, in which the film sample was embedded in an epoxy resin; thin slices were cut parallel to the film surface and then placed on the grid.

Nitrogen adsorption-desorption isotherms were measured using a Quantachrome Autosorb-6B sorption analyzer. Prior to the isotherm measurements, the samples were degassed at 350 °C overnight.

The phosphorus content in the calcined samples was determined from X-ray fluorescence (XRF) measurements done on a Philips PW1480 spectrometer. The concentrations were calculated with the semi quantitative program UniQuant5®.

1.3 Results and Discussion

Figure 1.1 shows SEM images of the materials synthesized under static conditions. Initially, freestanding, transparent films were produced at the air-water interface.

Subsequent ageing and calcination resulted in a film with a smooth, crack free continuous surface having a uniform thickness of 40 µm (as seen in Figure 1.1a). It was also observed that thin rods extended from the surface of the film and into the solution. On reaching a certain length, these rods got detached from the film surface.

A white precipitate was formed as well. Calcination of the aged sample resulted in a cake-like structure as shown in Figure 1.1b. Close observation of the cake indicated that it was composed of a closely packed network of particulate grains (inset of Figure 1.1b). The void existing between these grains (inter-particle space) provides macroporosity (in addition to the mesoporosity) resulting in a hierarchical porous material.

Materials prepared under vigorous stirring conditions resulted in fiber-like morphologies. Figure 1.2 shows SEM images of fibers of length over 100 µm in length and a width of 10 µm. Close examination of these fibers indicated that the fibers were made up of several individual segments coupled together along their length (Figure 1.2b). Products synthesized under slow stirring conditions had a unique morphology in the form of bundles as shown in Figure 1.3 (c) and (d), several hundred µm in length and with a width of at least 50 µm. The bundles are composed of long thin thread-like structures fused together (Figure 1.3b).

Figure 1.4 shows the X-ray diffraction patterns (XRD) of the different morphologies obtained by changing the stirring rate. The XRD patterns of fibers, bundles and cakes show sharp peaks corresponding to (100), (110) and (200) reflections indicating highly ordered mesoporous SBA-15 with a 2D hexagonal symmetry (p6mm) [19].

In comparison, the absence of the (110) reflection for the film suggests that the pore channels are aligned parallel to the film surface. Similar observations have been made by Zhao *et al.* [17] who synthesized mesoporous SBA-15 films on polished silicon wafers and confirmed the

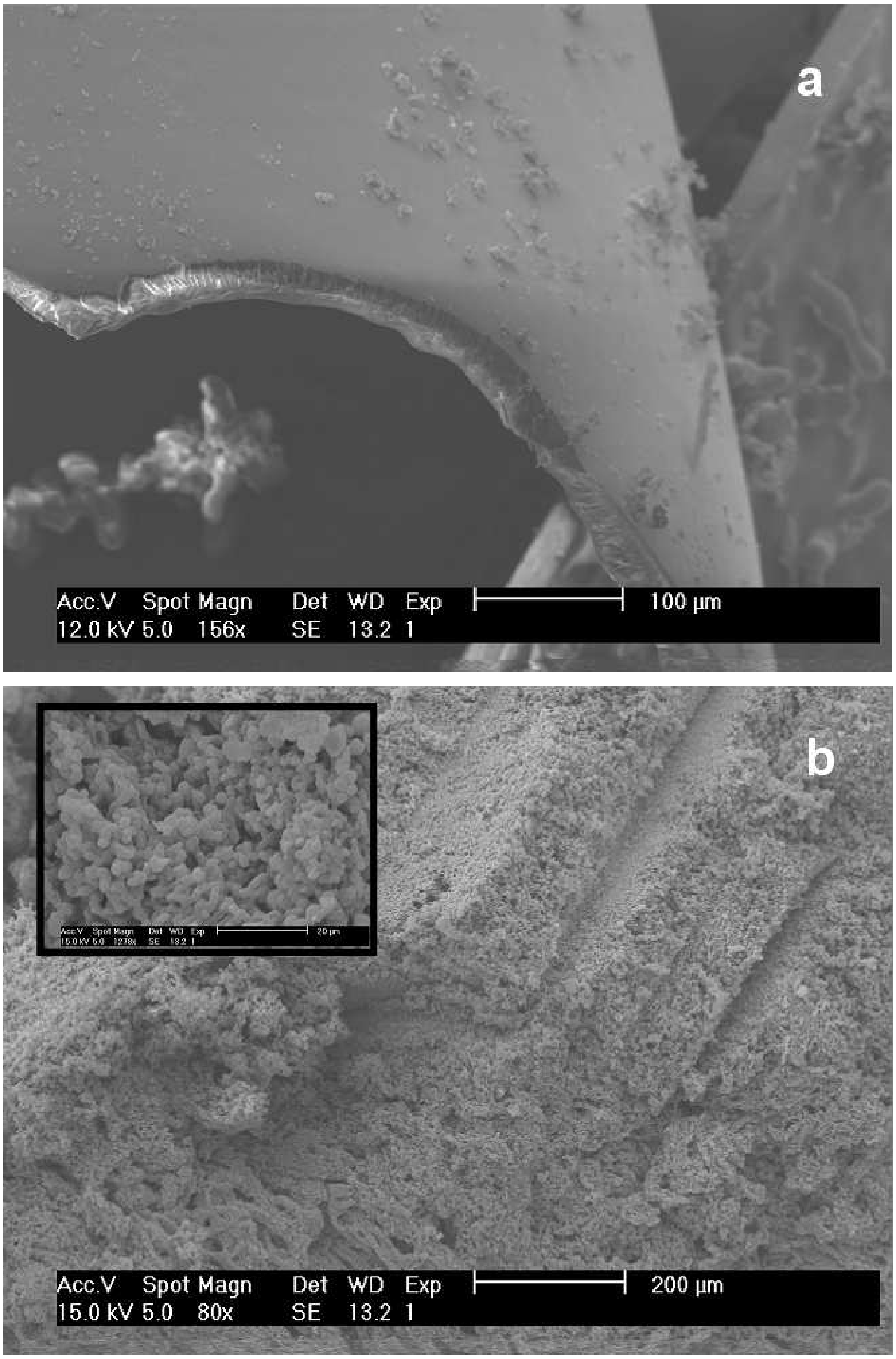

Figure 1.1: SEM of calcined (a) film and (b) cake

orientation of the pore channels from TEM images. The cell parameter of films, cakes, fibers and bundles (calculated using the formula $a = 2d_{100}/\sqrt{3}$, d_{100} is the interplanar spacing) is 11.4, 10.4, 10.6 and 10.6 nm respectively.

The calcined film has a Brunauer-Emmett-Teller (BET) surface area of 833 m^2/g, a pore volume

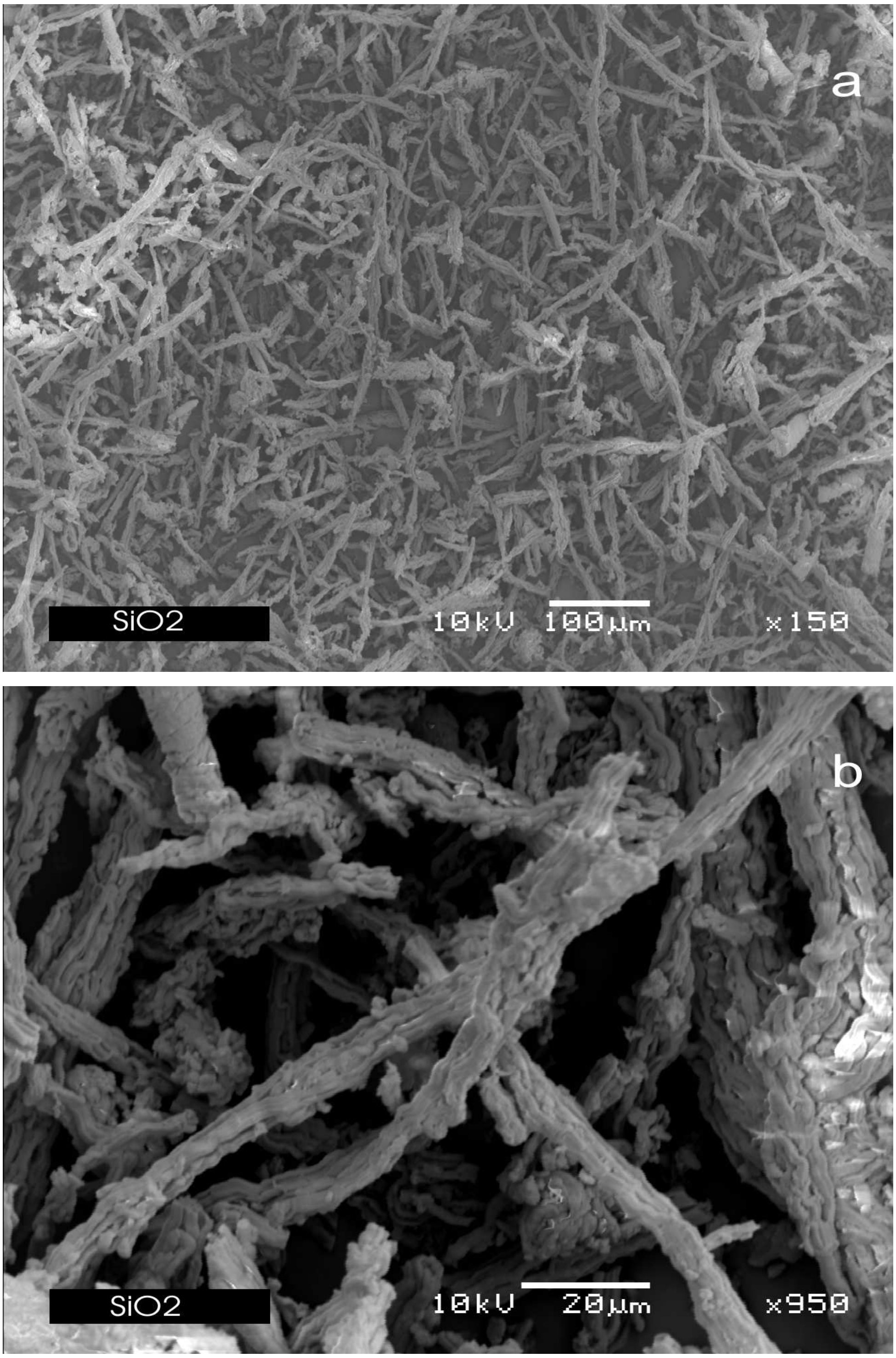

Figure 1.2: (a) and (b) SEM images of SBA-15 fibers

of 0.88 cm^3/g and an average pore size of 8.0 nm calculated by using the Barrett-Joyner-Halenda (BJH) model applied to the adsorption branch of the isotherm. The calcined cake has a BET surface area of 827 m^2/g, a pore volume of 1.04 cm^3/g and a BJH pore size of around 8.0 nm.

The N_2 adsorption-desorption isotherms (Figure 1.5) of calcined silica fibers and bundles are

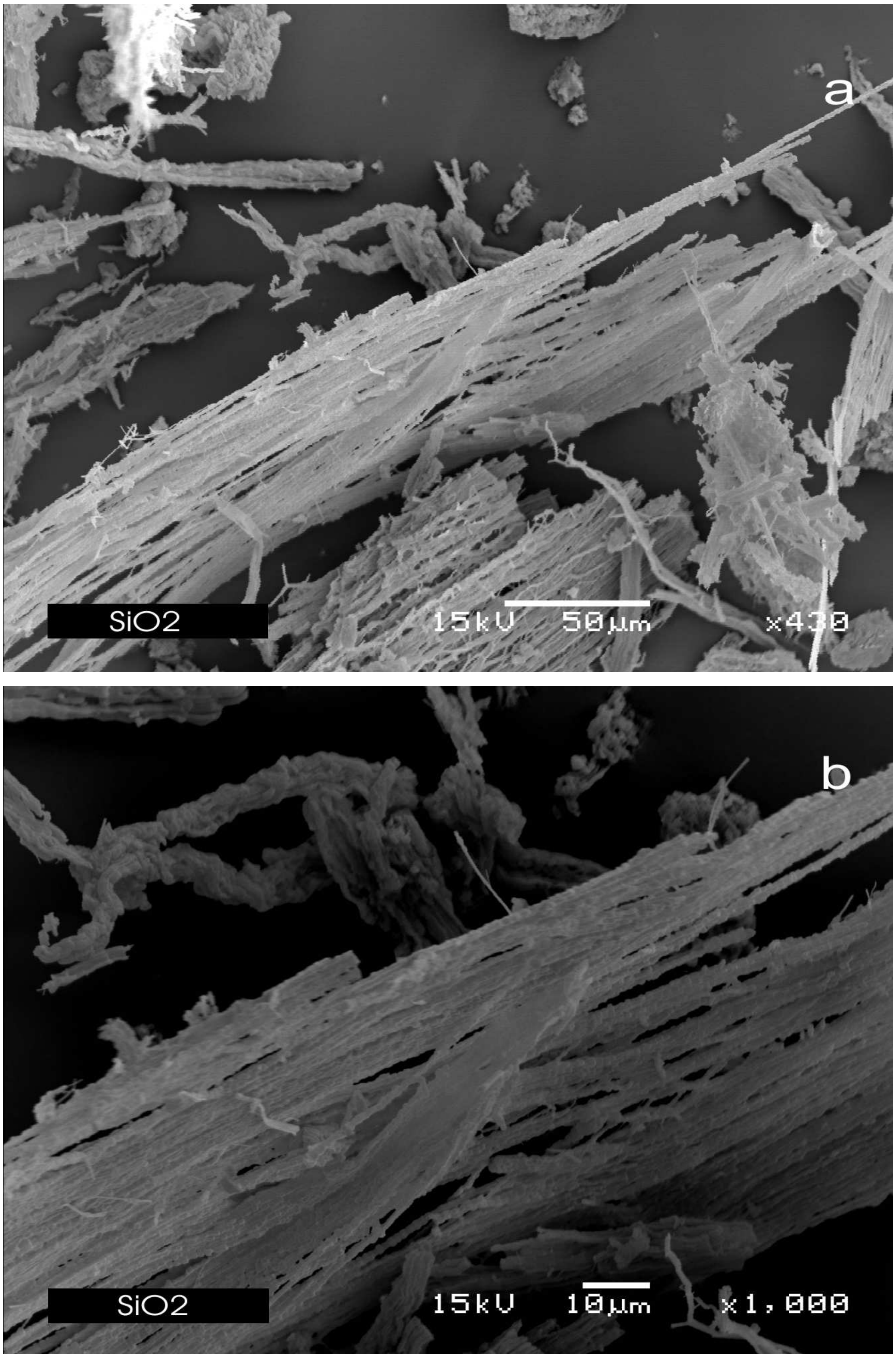

Figure 1.3: (a) and (b) SEM images of SBA-15 bundles

type IV with a clear type H1 hysteresis loop. The isotherms and corresponding pore size distributions (inset of Figure 1.5a and b) indicate the presence of a narrow pore size distribution in both fibers and bundles. The fibers have a BJH pore size of 8.0 nm (calculated from the adsorption isotherm), a BET surface area of 626 m^2/g and a pore volume of 0.83 cm^3/g. The bundles have a slightly larger pore size of 8.8 nm, a much higher BET surface area of 968 m^2/g

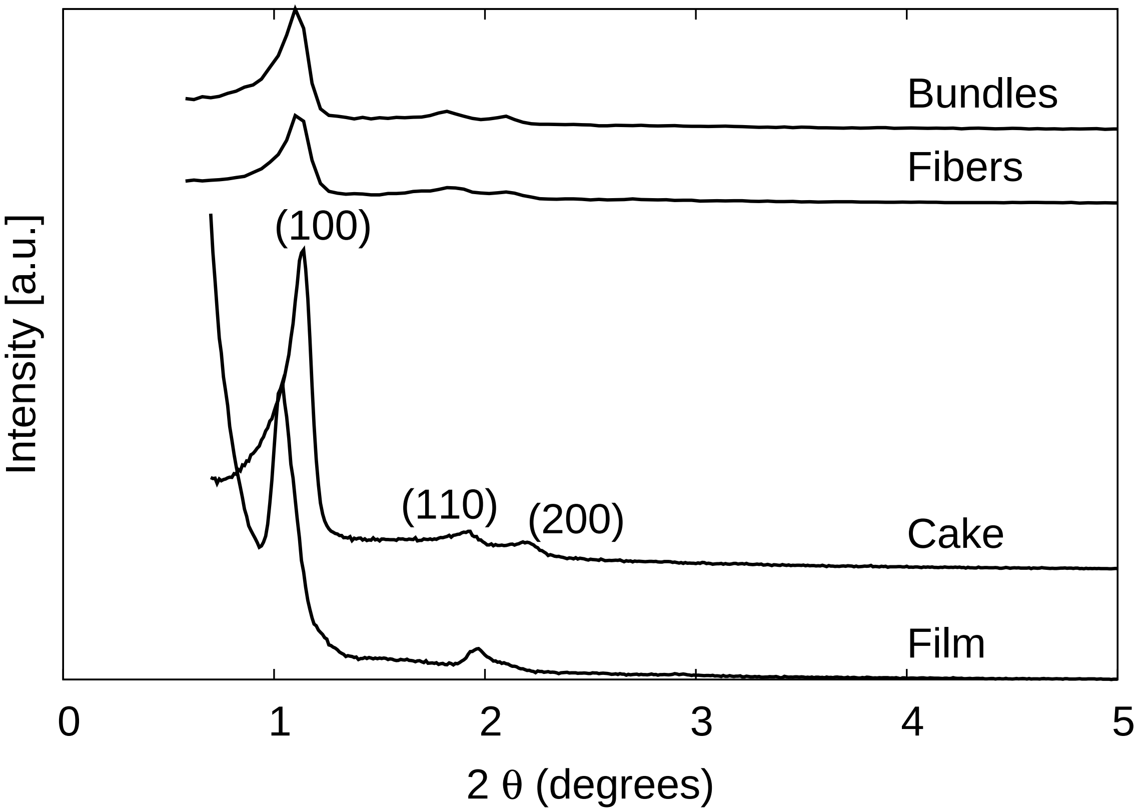

Figure 1.4: X-ray diffraction patterns of different samples

and a pore volume of 1.3 cm^3/g.

Insight into the pore structure of the mesoporous silica bundles is revealed by TEM (Figure 1.6). Well-ordered hexagonal arrays of pores were found in the bundle cross-section (Figure 1.6b). Figure 1.6a shows the high structural order, with parallel nanochannels of a uniform diameter that follow the long axis of the bundles with high fidelity. A TEM image of the top view of the microtomed film (Figure 1.7) shows that the channels run predominantly parallel to the film surface. This is in agreement with the observed XRD pattern (Figure 1.4).

The stirring rate can thus be used effectively to tune the morphology of SBA-15. The different shear rate associated with different stirring conditions influences the shape and aggregation of micelles, as well as the interfacial growth of the silica-surfactant mesophase, resulting in distinct morphologies. Note again that the starting composition was identical in all experiments. It is not clear yet how the H_3PO_4 affects the morphology.

Table 1.1: XRF measurements of fibers and bundles

Sample	Si/P [mol/mol]	
	Initial Gel (Calculated)	Calcined (XRF measurements)
Fibers	0.81	190.1
Bundles	0.81	18.0

X-ray fluorescence measurements of the fibers and bundles indicated the presence of phospho-

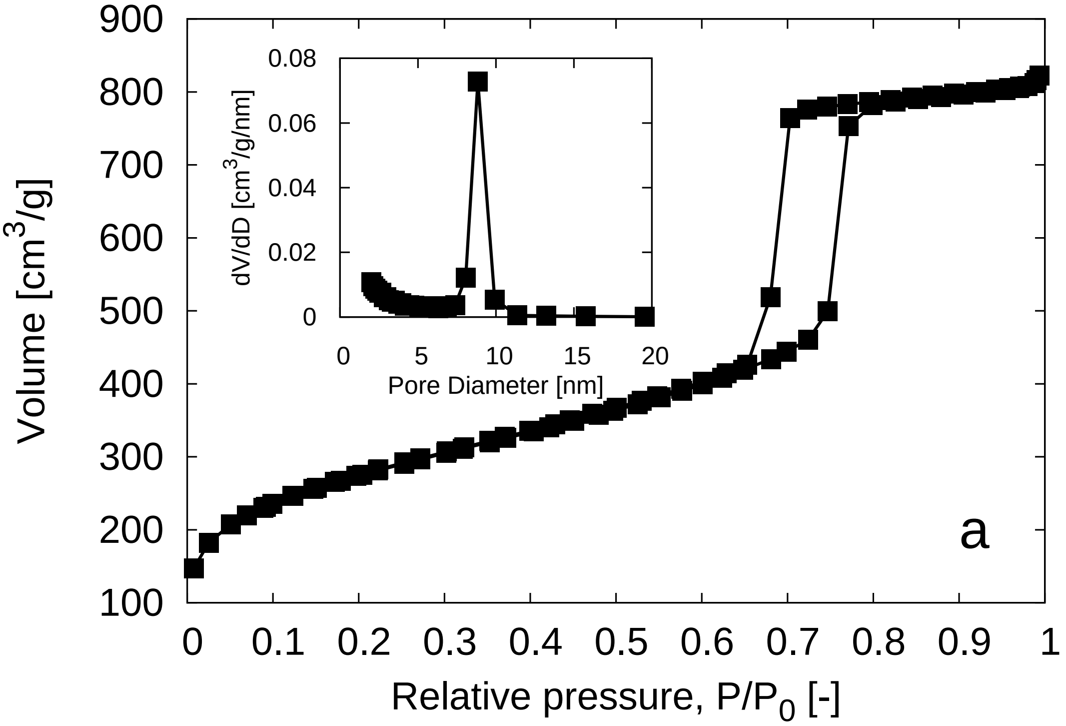

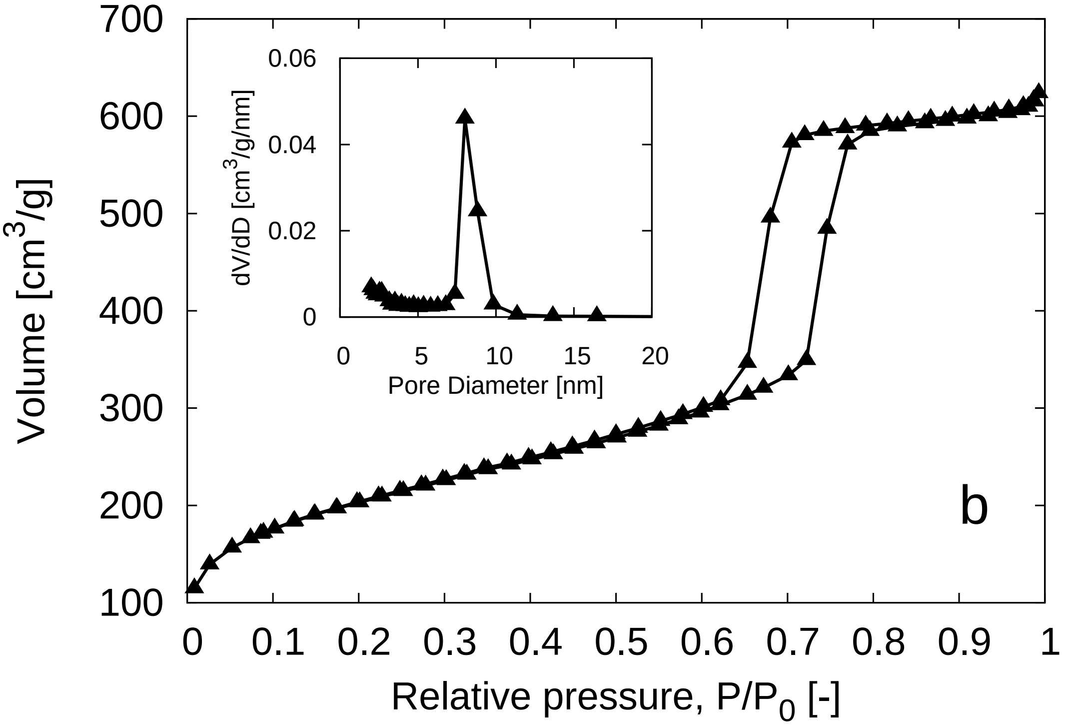

Figure 1.5: N_2 adsorption-desorption isotherms and (inset) pore size distributions of (a) fibers and (b) bundles calculated using the BJH model from the adsorption branch of the isotherms

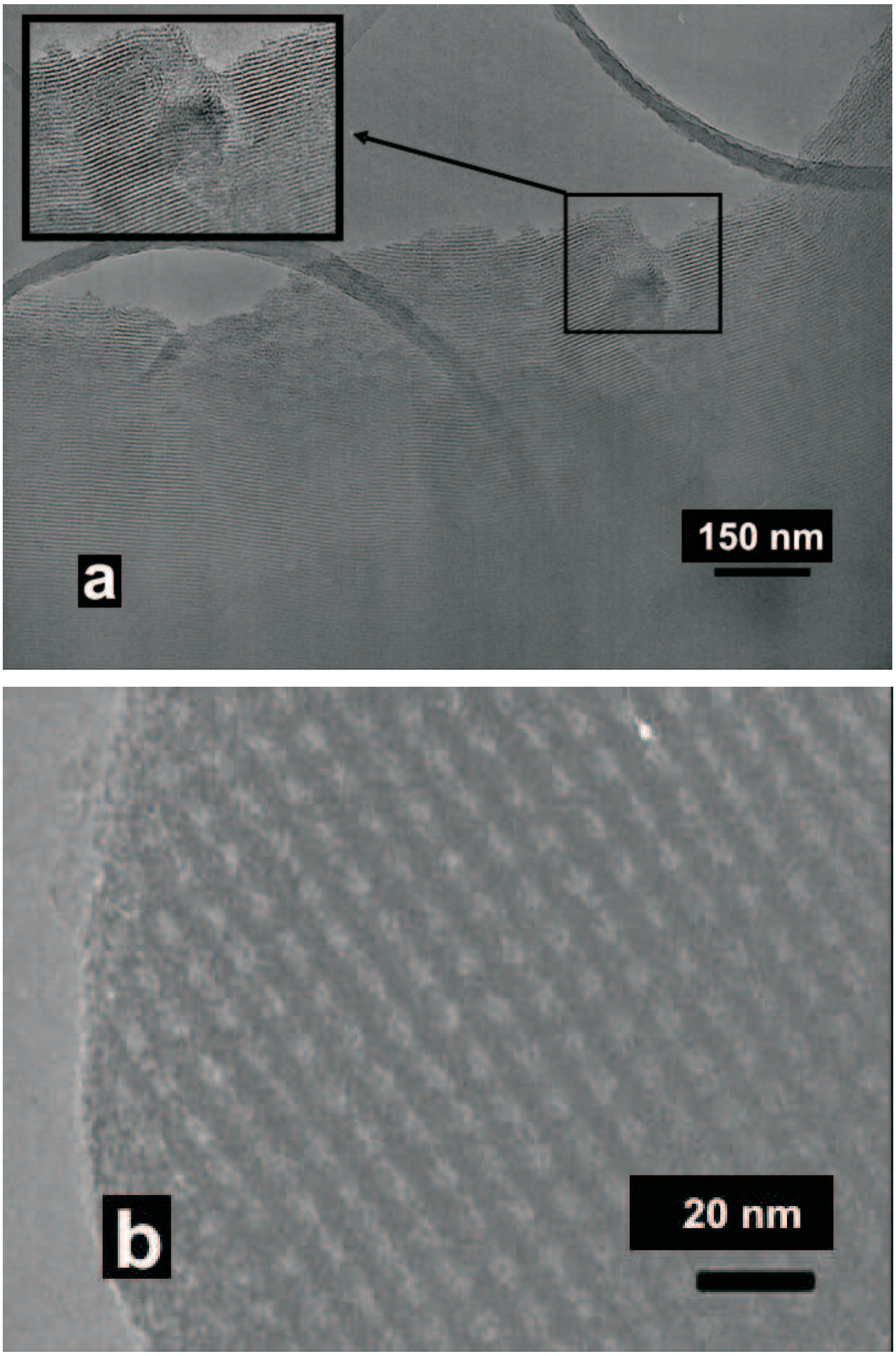

Figure 1.6: TEM images of calcined silica bundles along directions (a) [1 1 0] and (b) [1 0 0]

rus in the silica framework even after calcination at 550 °C (Table 1.1). The phosphorus content in the bundles was more than 10 times that present in the fibers. The generation of Brønsted acidity is proposed due to interaction of the H_3PO_4 with the silica species during hydrolysis to form $P-O-Si$ bonds. Although the hydroxyl groups of phosphoric acid can be removed by dehydration during high temperature calcination, the hydroxyl groups can also be restored after

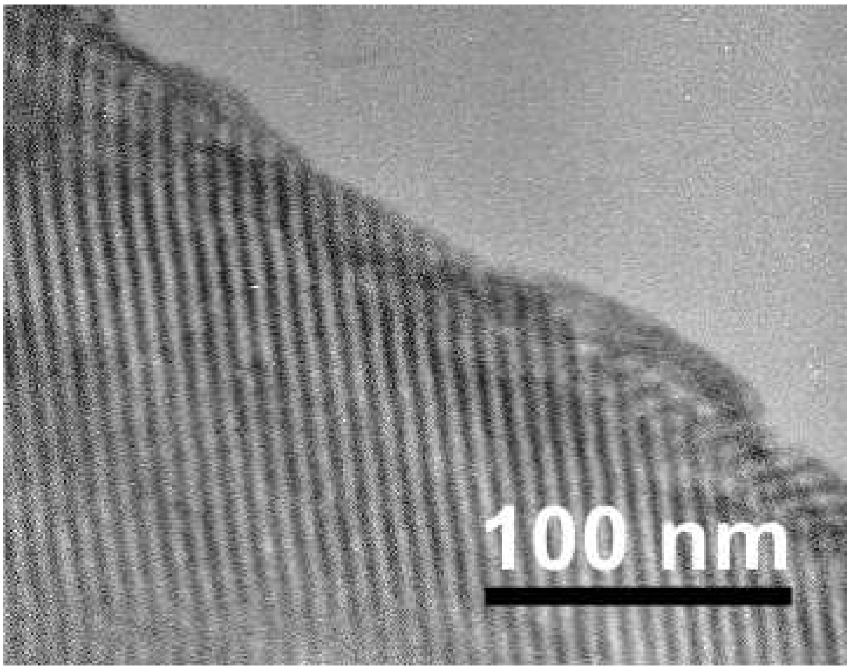

Figure 1.7: TEM image of mesoporous SBA-15 film (topview)

adsorption of moisture from the air. These restored hydroxyl groups on phosphorus have the ability to donate protons, producing mainly Brønsted acid sites on the surface of SBA-15. This improves the overall acidity of SBA-15 and could be used as a promising selective catalyst for specific reactions that need only Brønsted acidity, for instance dehydration of isopropanol [20]. Phosphorus containing catalysts have been shown to improve the activity for selective oxidation of hydrocarbons [21] and improve hydrothermal stability of the mesoporous framework [22].

1.4 Conclusions

In summary, we successfully synthesized distinct morphologies (films, cakes, fibers and bundles) of highly ordered mesoporous SBA-15 in the presence of weak acid (H_3PO_4) by simply changing the stirring rate. XRF measurements indicated the presence of phosphorus in the silica framework generating additional Brønsted acid sites. TEM images of the bundles revealed parallel nanochannels oriented along the long axis of the bundles.

References

1. D. Zhao, Q. Huo, J. Feng, B. F. Chmelka, G. D. Stucky, J. Am. Chem. Soc. 120 (1998) 6024.
2. A. Sayari, Y. Yang, Chem. Mater. 17 (2005) 6108.
3. A. Galarneau, H. Cambon, F. Di Renzo, R. Ryoo, M. Choi, F. Fajula, New J. Chem. 27 (2003) 73.
4. P. Alexandridis, J. F. Holzwarth, T. A. Hatton, Macromolecules 27 (1994) 2414.

5. P. Alexandridis, L. Yang, Macromolecules 33 (2000) 5574.
6. A. G. Denkova, E. Mendes, M.-O. Coppens, J. Phys. Chem. B 112 (2008) 793.
7. C. T. Kresge, M. E. Leonowicz, W. J. Roth, J. C. Vartuli, J. S. Beck, Nature 359 (1992) 710.
8. P. Selvam, S. K. Bhatia, C. G. Sonwane, Ind. Eng. Chem. Res. 40 (2001) 3237.
9. H. Miyata, T. Nama, M. Watanabe, K. Kuroda, Chem. Mater. 14 (2002) 766.
10. H.F. Yang, Q. H. Shi, B. Z. Tian, S. H. Xie, F. Q. Zang, Y. Yan, B. Tu, D. Y. Zhao, Chem. Mater. 15 (2003) 536.
11. D. Zhao, J. Sun, A. Li, G. D. Stucky, Chem. Mater. 12 (2000) 275.
12. P. Schmidt-Winkel, P. D. Yang, D. I. Margolese, B. F. Chmelka, G. D. Stucky, Adv. Mater. 11 (1999) 303.
13. P. D. Yang, D. Y. Zhao, B. F. Chmelka, G. D. Stucky, Chem. Mater. 11 (1998) 2033.
14. C. Z. Yu, B. Z. Tian, J. Fan, G. D. Stucky, D. Y. Zhao, J. Am. Chem. Soc. 124 (2002) 4556.
15. H. Yang, N. Coombs, I. Sokolov, G. A. Ozin, Nature 381 (1996) 589.
16. H. Yang, A. Kuperman, N. Coombs, S. M.- Afara, G. A. Ozin, Nature 379 (1996) 703.
17. D. Zhao, P. Yang, N. Melosh, J. Feng, B. F. Chmelka, G. D. Stucky, Adv. Mater. 10 (1998) 1380.
18. Q. Huo, D. Zhao, J. Feng, K. Weston, S.K. Buratto, G.D. Stucky, S. Schacht, F. Schth, Adv. Mater. 9 (1997) 974.
19. D.Y. Zhao, J.L. Feng, Q.S. Huo, N. Melosh, G.H. Fredrickson, B.F. Chmelka, G.D. Stucky, Science 279 (1998) 548.
20. S. Kawi, S.C. Chen, P.L. Chew, J. Mater. Chem. 12 (2002) 1582.
21. L. Hagey, H. de Lasa, Chem. Eng. Sci. 54 (1999) 3391.
22. L.M. Huang, Q.Z. Li, Stud. Surf. Sci. Cat. 129 (2000) 93.

Chapter 2

Tracing Pore Connectivity and Architecture in Nanostructured Silica SBA-15

2.1 Introduction

Novel synthesis routes have led to an impressively large spectrum of nanoporous materials of different composition, pore architecture, and shape. In many cases, appropriate fluid transport properties are essential for their technical application [1,2]. Hence, in addition to the well-established methods of textural characterization [3], diffusion measurements are often indispensable to completely characterize these materials. In many cases, the mechanisms and structural properties thus identified as rate limiting for overall mass transfer deviate dramatically from those expected on the basis of the “textbook” structure of these materials.

The present chapter deals with the application of the pulsed field gradient technique of nuclear magnetic resonance (PFG NMR) to diffusion studies in nanoporous silica SBA-15 [4]. The materials under study were synthesized following the original procedure described in [5], which includes the weak acid $\mathrm{H_3PO_4}$ instead of HCl. By simply controlling the stirring rate of one and the same starting mixture, a simple route was found to generate particle shapes of a broad variety. It shall be demonstrated that the structural differences associated with two different morphologies of the SBA-15 specimens under study, namely isolated fibers and bundles, are nicely reflected by the transport properties of guest molecules.

This chapter is based on the following publication:
S. Naumov, R. Valiullin, J. Kärger, R. Pitchumani, M.-O. Coppens, Micropor. Mesopor. Mater. 110 (2008) 37.

2.2 Experimental

Figure 2.1 shows SEM images of the two SBA-15 specimens studied here. Their textural properties are given in Table 2.1. Nitrobenzene was used as an NMR probe molecule. Prior to introduction into the NMR sample tubes (7.5 mm O.D., 10 mm filling length), the SBA-15 material was activated by heating (24 h at 323 K) under evacuation. After activation, the bulk nitrobenzene was added in excess to the evacuated probe material at a temperature of 297 K.

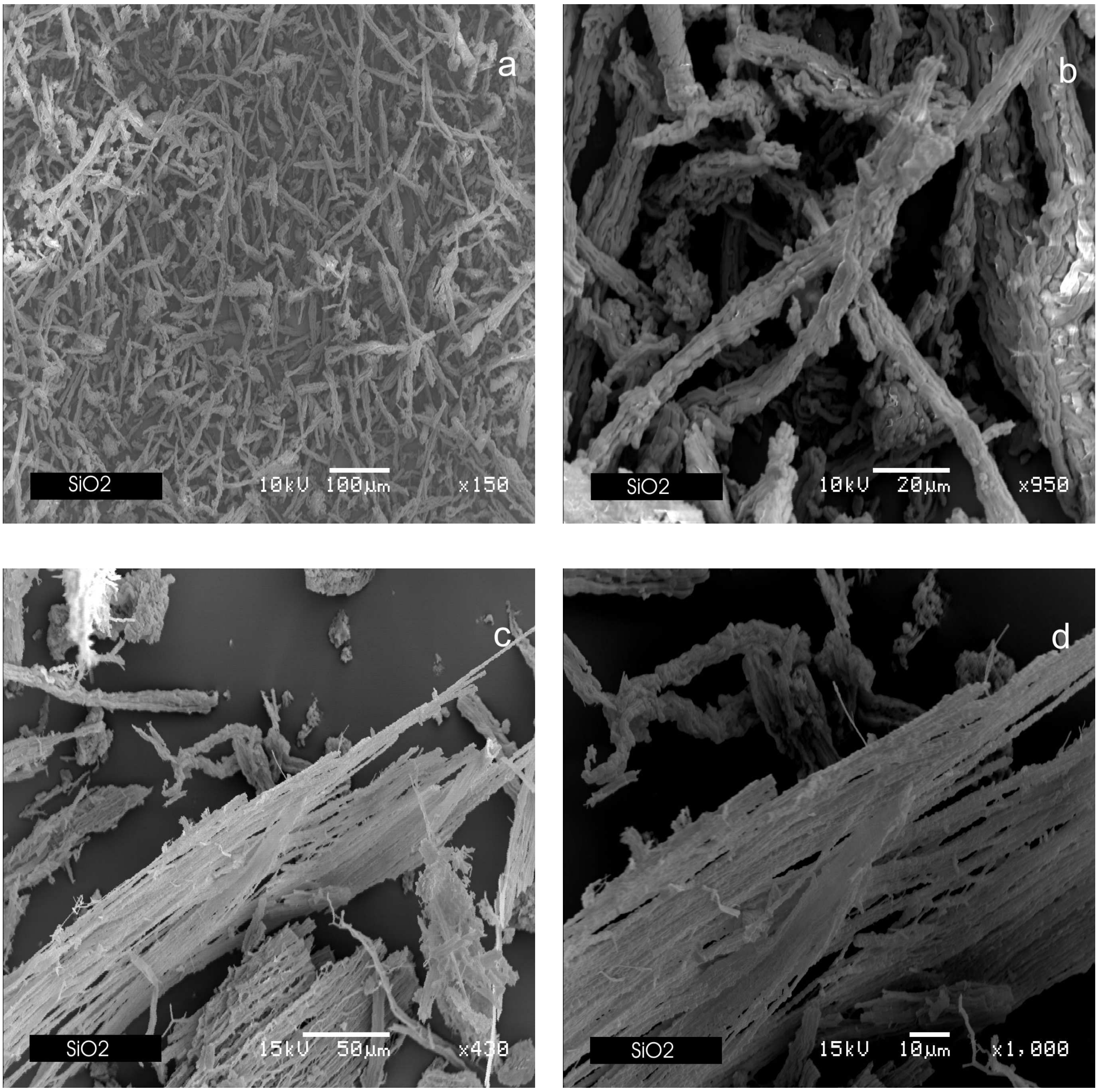

Figure 2.1: SEM images of SBA-15 fibers (a and b) and bundles (c and d) [5]

All diffusion measurements were performed at 253 K, i.e., considerably below the melting point of bulk nitrobenzene (T_{melt} = 278 K). In this way, the space outside of the mesopores is essentially blocked by the phase of frozen nitrobenzene, while the pore space - owing to the melting-point depression [6,7] - is still accommodated by liquid nitrobenzene. The diffusion behavior of the molecules within this liquid phase was studied in our experiments. The self diffusion coefficient of nitrobenzene in bulk is 2×10^{-9} m^2/s [8].

Table 2.1: Textural properties of SBA-15

Morphology	S_{BET} [m^2/g]	V_t [cm^3/g]	d_{BJH} [nm]	V_μ [cm^3/g]	S_{meso} [m^2/g]	a [nm]	t [nm]
Fibers	968	1.26	8.8	0.15	629	10.6	1.8
Bundles	626	0.83	8.0	0.092	421	10.6	2.6

S_{BET} - BET surface area, V_t - total pore volume, d_{BJH} - BJH pore diameter obtained by applying the BJH model to the adsorption branch of the isotherm, V_μ - micropore volume, S_{meso} - mesopore surface area, a - cell parameter, t - pore wall thickness ($t = a - d_{BJH}$).

The PFG NMR diffusion measurements have been performed on an NMR spectrometer at 400 MHz with a home-built gradient unit [9]. The measurement, based on the sequence of radio frequency and gradient pulses, generates an NMR signal, the so-called spin echo of resonant nuclei (^{1}H). Dependent on gradient duration δ, gradient strength g and observation time t, the spin echo amplitude $M(\delta g, t)$ becomes sensitive to the translational motion of molecules in the probe (diffusion). Assuming that the pulsed field gradients are applied along the z-axis in the laboratory frame of reference, the echo attenuation factor [10,11] is given by:

$$\psi(\delta g, t) = \frac{M(\delta g, t)}{M(\delta g = 0, t)} = \int P(z, t) e^{-\imath(\gamma \delta g) z} dz \tag{2.1}$$

The diffusion propagator $P(z, t)$ denotes the probability that during the observation time t the molecules are displaced over a distance z in the field gradient direction. The gyromagnetic ratio is $\gamma = 2.67 \times 10^8$ T^{-1}s^{-1} for the probed ^{1}H nuclei. According to Equation (2.1), the spin echo attenuation, $\psi(\delta g, t)$ can be used to monitor the self-diffusion process. In the case of normal unrestricted self-diffusion, the averaged propagator is a Gaussian and the spin echo attenuation is described by a mono-exponential decay:

$$\psi(\delta g, t) = e^{-(\gamma \delta g)^2 D_z t} = e^{-D_z q^2 t} \tag{2.2}$$

with $q = \gamma \delta g$. In complex systems, the averaged propagator may deviate from a Gaussian. In PFG NMR, these deviations allow us to determine additional characteristic parameters which influence self-diffusion under the given constraints.

For systems with an anisotropic pore structure, as in the case of both SBA-15 silica samples, we expect the propagation to be dependent on the direction of propagation within the system. The self-diffusivity parallel to the direction of the 1-D channel (D_{par}) should be much larger than the self-diffusion coefficient perpendicular to it (D_{perp}). Thus, displacements along the channels are much less inhibited by transport resistances than displacements perpendicular to the channel axis. The latter may result from defects in the channel walls or the channel ends.

2.3 Results and Discussion

Figure 2.2 provides a typical representation of the signal attenuation in the PFG NMR experiments. It notably deviates from the simple Equation (2.1), which predicts an exponential decay, and, therefore, a straight line in a logarithmic plot. However, in view of the sample anisotropy, such a deviation is to be expected, as Equation (2.1) is valid for isotropic diffusion only.

PFG NMR signal attenuation in the case of anisotropic diffusion in a powder sample (i.e., with crystals oriented in all directions with equal probability) satisfies the following equation in a spherical coordinate system [12,13]:

$$\psi(\delta g, t) = \frac{1}{4\pi}\int_0^{2\pi}\int_0^{\pi} e^{\{-(\gamma\delta g)^2 t(D_{xx}\cos^2\theta + D_{yy}\sin^2\theta\cos^2\phi + D_{zz}\sin^2\theta\sin^2\phi)\}}\sin\theta d\theta d\phi \qquad (2.3)$$

where the quantities D_{xx}, D_{yy} and D_{zz} indicates the principal elements of the diffusion tensor. Due to rotational symmetry of the system under study, in our case Equation (2.3) simplifies to (again with $q = \gamma\delta g$):

$$\psi(q, t) = \frac{1}{2}\int_0^{\pi} e^{\{-q^2 t(D_{par}\cos^2\theta + D_{perp}\sin^2\theta)\}}\sin\theta d\theta \qquad (2.4)$$

where D_{par} and D_{perp} are the self-diffusivities as introduced above. Since the host particles within our sample tube may assume all directions with equal probability, Equation (2.4) may be finally transformed into:

$$\psi(q, t) = \frac{\sqrt{\pi}}{2}e^{-q^2 t D_{perp}}\frac{\text{erf}\left(\sqrt{q^2 t(D_{par} - D_{perp})}\right)}{\sqrt{q^2 t(D_{par} - D_{perp})}} \qquad (2.5)$$

Figure 2.2 displays those representations of Equation (2.5) which provide the best fit to the experimental data. The values for D_{par} and D_{perp} used in the fit are shown in the inset.

Figure 2.3 presents a complete survey of the self-diffusivities D_{par} and D_{perp} and their dependence on the observation time as resulting from the PFG NMR signal attenuation curves for the different observation times considered. In addition to the observation times t, in the abscissa we have also indicated the mean square displacements $\langle s_{par}^2\rangle$ in the mesopore channel direction and perpendicular to it. These displacements are related to the corresponding self-diffusivities D (D_{par} and D_{perp}, respectively) by Einstein's equation [14]:

$$\langle s^2\rangle = 2Dt \qquad (2.6)$$

The following summarizes our main findings:

1. Irrespective of a pronounced diffusion anisotropy over the considered temporal and spatial scales (as indicated in the abscissa), diffusion is by far not ideally one-dimensional. This suggests (as in the case of water in the MCM-41 sample studied in [15]) the following:

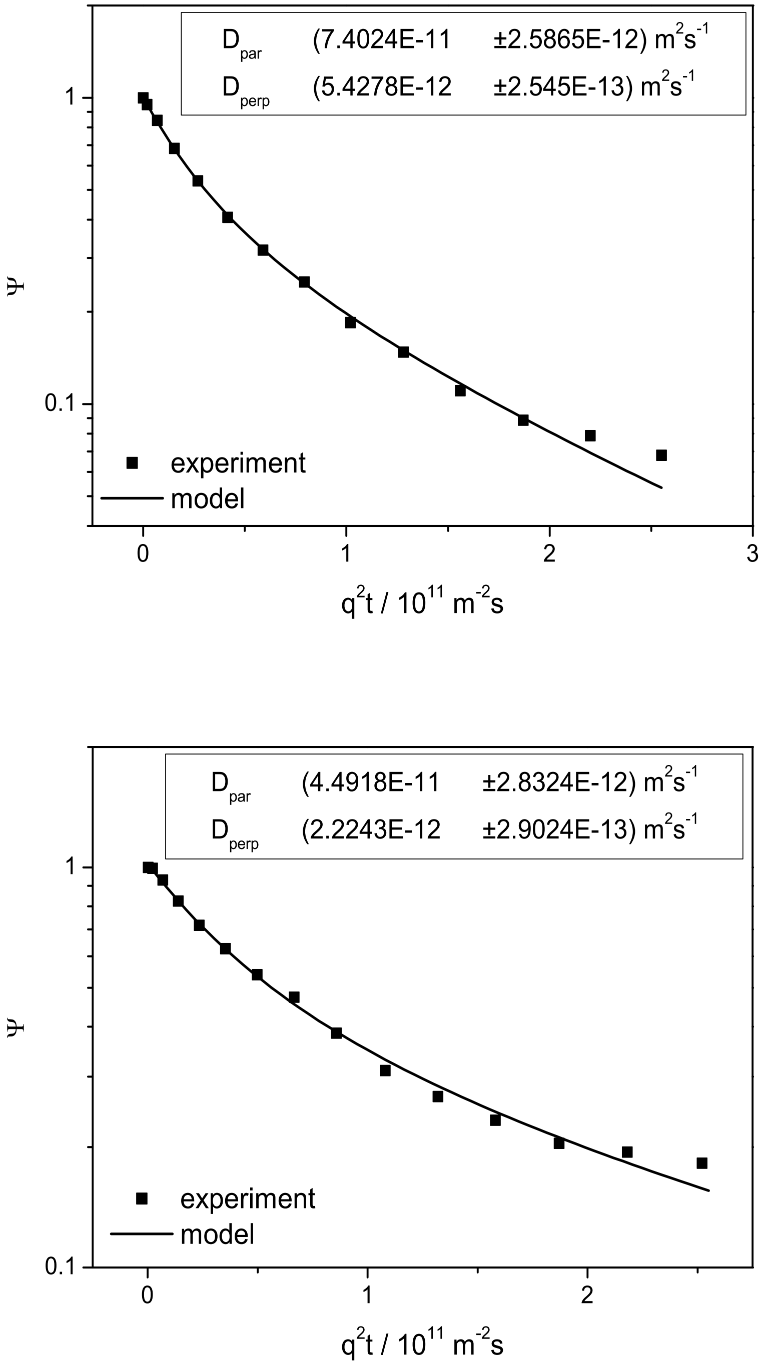

Figure 2.2: Spin echo attenuation for nitrobenzene in SBA-15 fibers. The solid lines represent the best fits of the analytical solution (Equation (2.5)), with the parameters as indicated in the inserts. Top panel: Observation time t = 5 ms, bottom panel: Observation time t = 300 ms

(a) Displacements in the channel direction within the bundles are described with a constant diffusivity. This means that over the observed displacements of 4 µm, molecular transport in the longitudinal direction is not affected by additional transport

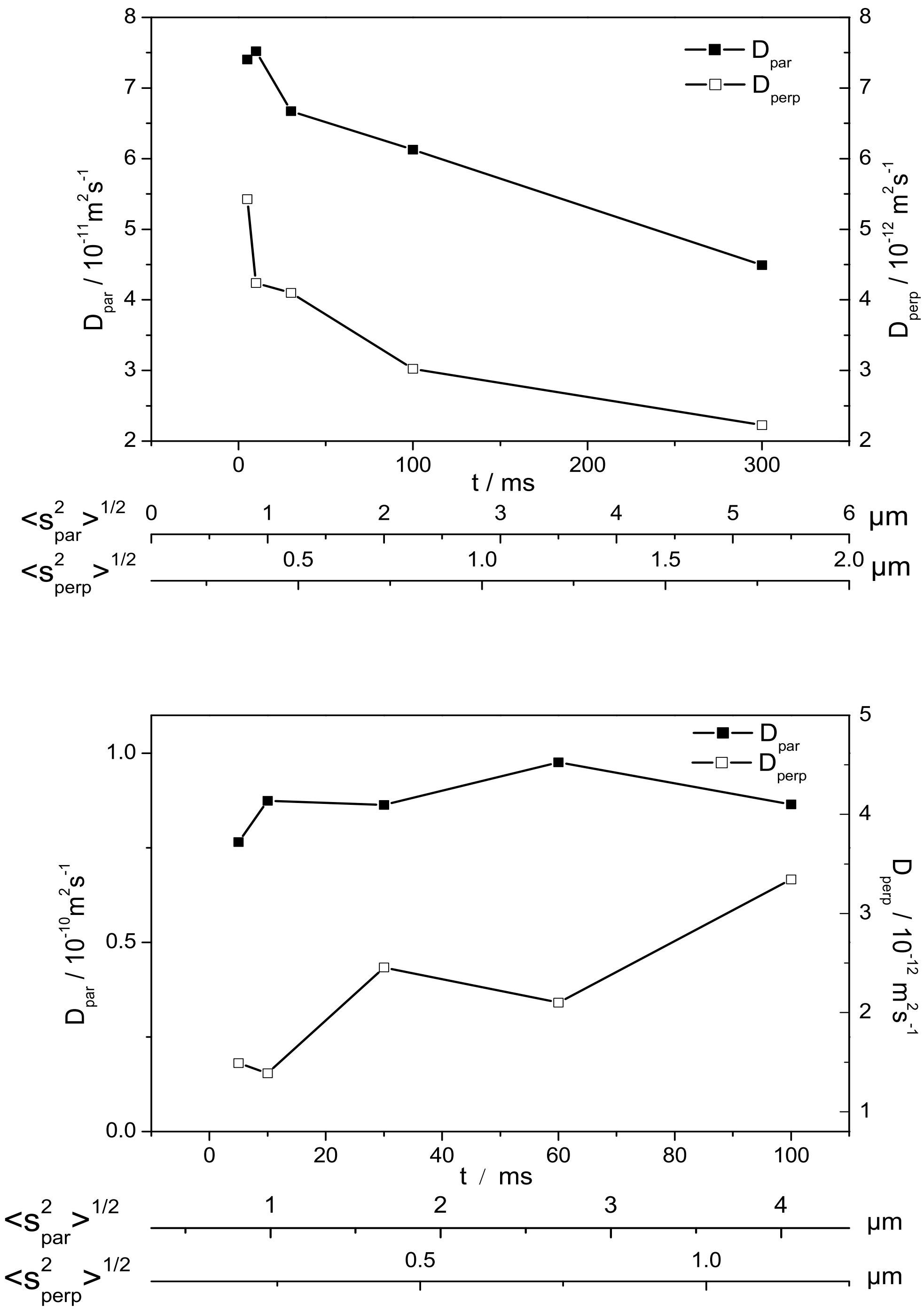

Figure 2.3: Self-diffusivities D_{par} and D_{perp} as a function of diffusion (i.e., observation) time for SBA-15 fibers (top) and bundles (bottom). For an illustration of the distances over which these diffusivities have been measured, the abscissa displays the values of the mean-square displacements $\langle s^2_{par} \rangle$ and $\langle s^2_{perp} \rangle$, resulting from an average value of the diffusivities in the respective directions by application of Equation (2.6)

resistances that might confine the propagation.

   (b) However, the channel walls are, to some extent, permeable. Indeed it is known that the walls of SBA-15 are microporous [16,17].

   (c) The length of individual channel segments is small in comparison with displacements in the channel direction (up to 5 µm for the abscissa in Figure 2.3) so that, at the end of each channel segment, the molecules may move into a direction perpendicular to the channel direction or through the segment ends.

2. Additionally, in the bundles there is a tendency that displacements perpendicular to the mean channel direction proceed at a rate increasing with increasing observation time. This finding suggests the absence of a perfect channel structure over distances of the order of these displacements (1 µm), which facilitate propagation perpendicular to the mean channel direction.

3. In the fibers, both diffusivities are found to (slightly) decrease with increasing observation time. This points to some confinement and, hence, to a retarded propagation over longer distances, in contrast to what is observed with the bundles. The lateral extension of the fibers is far below that of the bundles, therefore it could be expected that in the case of the fibers the external frozen phase will lead to spatial confinement within much narrower dimensions than in the bundles. This agrees with the experimental findings.

2.4 Conclusions

Differences in SBA-15 silica morphology lead to specific differences in the propagation pattern of guest molecules, as revealed by PFG NMR, using nitrobenzene as the probe molecule. Nitrobenzene was used in excess, so that inside the NMR sample tubes, the host particles were surrounded by a bulk phase of the guest molecules. Thus, by selecting a temperature below the melting point of the bulk (253 K) and above that of the guest in the host mesopores, molecular propagation, as traced by PFG NMR, is essentially confined to the individual host particles. In both types of particles (fibers and bundles), the Brownian motion of molecules in the pores was found to be anisotropic, and characterized by a rotationally symmetrical diffusion tensor. The diffusion coefficient in the direction of the axis of symmetry (D_{par}) is one to two orders of magnitude larger than that in a direction perpendicular to it (D_{perp}). The quantity D_{par} is therefore referred to as the diffusion coefficient in the channel direction, while D_{perp} describes the rate of propagation perpendicular to the channel axis, due to either a finite permeability of the channel walls or to deviations from an ideal structure with infinitely extended straight channels. PFG NMR is unable to discriminate between these options, but it is known that the mesopore walls of SBA-15 are microporous.

With increasing observation time, D_{par} in bundles of SBA-15 “threads” is found to be constant. This indicates that, over the covered displacement range (up to 4 µm), there are no particularly pronounced transport resistances slowing down the rate of molecular propagation along the SBA-15 nanopores.

The rate of propagation in the perpendicular direction, which is one and a half orders of magnitude slower, is found to increase with increasing propagation time. This suggests the existence of defects, which facilitate the escape of guest molecules out of the threads constituting a bundle. In contrast to this behavior, in the fiber-like particles the diffusivity in directions perpendicular to the nanopores is found to decrease with increasing observation times, and, hence, with increasing displacements. This behavior may be related to the smaller size of the silica particles constituting a fiber, which results in stronger confinement of the fluid phase inside the silica pores. Variation in size of the guest molecules as well as of the amount of the excess guest phase between the particles would enable to trace the exchange rates between the different parts of the hierarchical pore space of a nanostructured material.

This novel option of pore space exploration, namely “porometry by diffusion”, should enhance our understanding of structured nanoporous materials.

References

1. T. J. Barton, L. M. Bull, W. G. Klemperer, D. A. Loy, B. McEnaney, M. Misono, P. A. Monson, G. Pez, G. W. Scherer, J. C. Vartuli, O. M. Yaghi, Chem. Mater. 11 (1999) 2633.
2. P. Selvam, S. K. Bhatia, C. G. Sonwane, Ind. Eng. Chem. Res., 40 (2001) 3237.
3. F. Schüth, K. Sing, J. Weitkamp (Eds.), Handbook of Porous Solids, Wiley-VCH, (2002).
4. D. Y. Zhao, Q. S. Huo, J. L. Feng, B. F. Chmelka, G. D. Stucky, J. Am. Chem. Soc. 120 (1998) 6024.
5. R. Pitchumani, W. Li, M.-O. Coppens, Catal. Today 105 (2005) 618.
6. C. L. Jackson, G. B. McKenna, J. Chem. Phys. 93 (1990) 9002.
7. C. Alba-Simionesco, B. Coasne, G. Dosseh, G. Dudziak, K. E. Gubbins, R. Radhakrishnan, M. Sliwinska-Bartkowiak, J. Phys.: Condens. Matter 18 (2006) R15.
8. R. Valiullin, István Furó, J. Chem. Phys. 116 (2002) 1072.
9. F. Stallmach, P. Galvosas, Spin echo NMR diffusion studies, Annu. Rep. NMR Spectrosc. 61 (2007) 51.
10. J. Krger, W. Heink, J. Magn. Reson. 51 (1983) 1.
11. P. Callaghan, Principles of Nuclear Magnetic Resonance Spectroscopy, Clarendon Press, 1991.
12. J. S. Waugh (Ed.), Advances In Magnetic Resonance, Academic Press, Inc., 1988.
13. J. Krger, H. Pfeifer, W. Heink, Adv. Magn. Reson. 12 (1988) 1.
14. K. Hahn, J. Krger, J. Phys. A: Math. Gen. 28 (1995) 3061.
15. F. Stallmach, J. Krger, C. Krause, M. Jeschke, U. Oberhagemann, J. Am. Chem. Soc. 122 (2000) 9237.
16. M. Kruk, M. Jaroniec, C. H. Ko, R. Ryoo, Chem. Mater. 12 (2000) 1961.
17. C. M. Yang, B. Zibrowius, W. Schmidt, F. Schuth, Chem. Mater. 15 (2003) 3739.

Chapter 3

Description of a Continuous Aerosol Reactor Setup for the Synthesis of Nanostructured Silica

3.1 Introduction

As discussed in Chapter 1, mesoporous silica was synthesized using a batch process that lasted several days to achieve ordered materials. Furthermore, the batch process has inherent disadvantages of heterogeneity in morphology of the final product. In order to overcome these limitations, a continuous reactor based on aerosols was designed and constructed.

There are at least two routes for the preparation of ultra fine particles by aerosol processes. The first involves gas-to-particle conversion and the second is the liquid-to-solid particle conversion. In gas-to-particle conversion, particles are generated by cooling a supersaturated vapor, involving the use of methods called physical vapor deposition (PVD) or "evaporation-condensation method" and chemical vapor deposition (CVD) [1]. PVD involves the evaporation of a solid or liquid which is the source of the vapor. Eventually, in the cooling stage, nucleation and condensation of the saturated vapor take place and solid particles are formed. In CVD, the vapor evaporated from the solution precursors is thermally decomposed or reacts with another precursor vapor or a surrounding gas. Finally, the solid particles are formed by nucleation, condensation and coagulation. Liquid-to-particle conversion (i.e., spray pyrolysis) is a representative "break-down" method for aerosol processing [2]. The spraying method is often classified as a liquid-phase method because solutions or sols are used. This method has been used to prepare numerous types of functional particles. In comparison to the gas-to-particle conversion route, the spraying method is a simple and low-cost process. Multi-component materials are also easily prepared by this route.

Suh and Suslick [3] used an inexpensive high-frequency ultrasound generator from a household humidifier to produce porous silica particles that are porous on the nanometer scale. By using two heated furnace zones, polymerization of organic monomers in the presence of silica colloid was initiated, which created, *in situ*, a composite of silica with an organic polymer, followed by a second heating to pyrolyze and remove the polymer. The final product was obtained by passing the aerosol exiting the furnace into water filled bubblers. It was shown that, in a single flow process, ferromagnetic cobalt nanoparticles can be easily encapsulated in the porous silica, and the resulting nanospheres are extremely resistant to air oxidation.

A variety of aerosol reactors is available for production of ultrafine powders. These are flame reactors [4], furnace reactors [5], gas condensation methods, plasma reactors [6], and laser ablation [7], to name a few.

The group of Prof. Kikuo Okuyama in Japan has reported impressive results using a tubular aerosol reactor, a method that we also used in this thesis. Using the spray-pyrolysis method, they prepared various functional fine particles, such as metal oxide superconductors [8], metal sulfides [9] and some rare-earth-doped oxide phosphor materials [10]. Iskander *et al.* [11,12] synthesized porous silica particles with controllable pore sizes by a spraying a precursor consisting of silica and polystyrene latex (PSL) nanoparticles and leading the droplets through a heated tubular reactor. The pores on the surface of the particles, left after burning away the template particles, were observed to be arranged into a hexagonal packing, and the pore size was controlled by changing the template (PSL) particle size.

The present chapter deals with the development of the aerosol apparatus, which was eventually used to synthesize nanostructured silica particles.

3.2 Experimental Setup

The aerosol experimental setup used in the present work essentially consists of an aerosol generator, possibly followed by a silica gel drier, a heated tubular reactor, and a particle collector. Figure 3.1 shows a schematic diagram of the setup used for nanostructured particle production in this thesis.

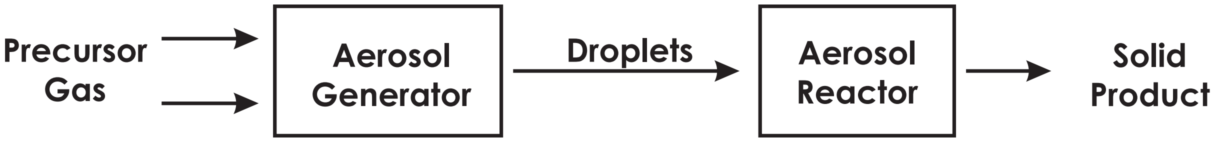

Figure 3.1: Schematic of an aerosol particle production process

Liquid precursor and a carrier gas are fed into the generator, and the liquid is disintegrated into fine droplets, which are then carried (by the gas) into the heated aerosol reactor. The final product is collected on a particle filter. Details of each part of the setup will be described in due course. The main feature of this process is that it is continuous with a process time of only a few seconds.

The particle size distribution of the final product can be controlled by controlling the droplet size distribution of the atomizer. Hence the final product depends upon the atomizer performance and its correct use. Several atomizers were tested; some required modifications to be used for our purpose.

3.2.1 Atomizers/Nebulizers

Nebulizers are devices that were originally invented for inhalation therapy. The initial work on water jets, and the concept of liquid jet disintegration and droplet formation go back to Bidone in 1829 [13] and Savart in 1833 [14]. In earlier times, the device was known as an apparatus for the pulverization of liquids. Compressed air is used to drive the apparatus by exerting pressure on a liquid, and atomization occurs at the end of a tube that has a small orifice.

The earliest nebulizers that were developed were based on three different basic principles:

- In the first type, a liquid jet impinges on a plate or an opposite jet to produce fine droplets.
- In the second type, air is turbulently mixed with the liquid to be atomized, which induces atomization.
- In the third type, compressed air is mixed with liquid in such a way that it sucks the liquid into the air stream, which is suddenly expanded at the exit of the nozzle.

The drop size and drop size distribution depend upon various design parameters like nozzle diameter and tube diameter, and operating parameters such as air pressure, liquid properties such as density, viscosity, slurry concentration and surface tension. Every commercial nebulizer has to be tuned or retrofitted for the suspension or slurry that needs to be atomized.

Several atomizers were used for the experiments in the present work. They are discussed below.

Ultrasonic nebulizer

The spray generator in this case was an ultrasonic particle generator with a 2.4 MHz resonator (Sonaer Inc., Model 241PG MHz). It transforms low-viscosity liquids into fine droplets. It uses the miniature 2.4 MHz model 241 Teflon-coated ultrasonic nebulizer unit shown in Figure 3.2.

The nebulizer mainly consists of a piezoelectric transducer that vibrates at a very high frequency. This produces ultrasonic waves that travel through the liquid and breaks the liquid surface into a fine mist (aerosol). The unit is fully microprocessor based, allowing the user to program operating parameters into the unit, handling a wide variety of applications for reproducible particle generation. On the front panel is an LCD display where the user can change the rate at which particles are generated from 0 to 100 % of the full output capability, in 5 % increments. A 304 stainless steel T-junction for air inlet and aerosol outlet is fastened on the nebulizing element with Teflon O-rings and clamps. A cylindrical metal reservoir is provided for the liquid precursor, and is connected to the nebulizing chamber with teflon tubes and an actuated valve. The nebulizing chamber is equipped with an external teflon optical sensor for keeping the liquid level to the correct height by regulating the flow of liquid from the reservoir, thus preventing damage to the nebulizing element, should the unit run dry. The microprocessor handles all the functions of the 241PG, including timed operation where particles can be made in preprogrammed amounts.

The nebulizer as obtained from the manufacturer had certain limitations for the present experimental needs. No aerosol was observed leaving the outlet on operating the atomizer with

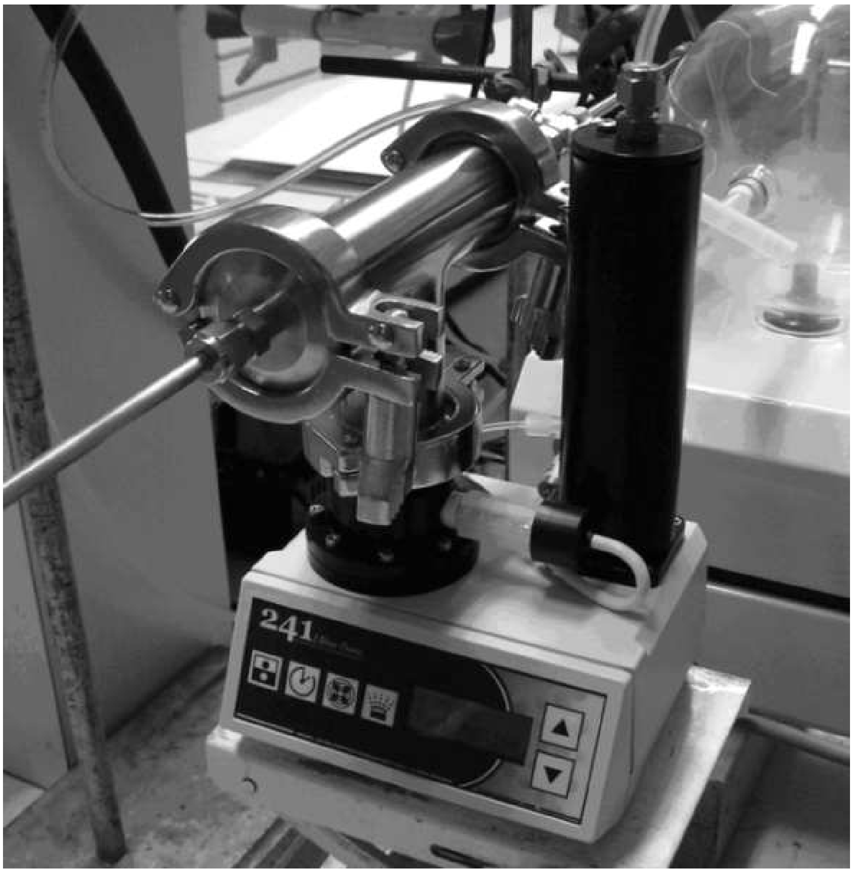

Figure 3.2: Ultrasonic nebulizer

compressed air, even though a mist was formed. A pair of blind flanges was fitted with 6 mm stainless steel tubing. These were attached to the T-junction with O-rings and stainless steel clamps, and served as inlet and outlet for the carrier gas and the generated aerosol, respectively. It was observed that on operating the atomizer with liquid, the incoming air was incapable of transporting all of the fine mist of droplets generated from the liquid surface. This was due to the fact that the air coming into the T-junction followed the path of least resistance by flowing in a straight line. The path of the incoming air needed to be diverted close to the liquid surface in the nebulizing chamber for efficient transportation of the droplets by the air in the form of an aerosol, and to allow for sufficient dilution of the generated droplets (to minimize agglomeration). This was achieved by manufacturing a stainless steel tube with one end connecting the air inlet, while the other end was welded to an L-junction and placed inside the nebulizer T (shown in Figure 3.3).

The end of the L-junction allowed fixing of small metal tubes held together by O-rings for an air-tight connection. These tubes could be easily detached and replaced. A tube of 7 cm in length was used for all the experiments.

Furthermore, it was also observed that the compressed air fed to the atomizer bypassed the air outlet, and instead passed through the liquid inlet of the nebulizing chamber, leading to bubbling of the liquid in the precursor reservoir. As a result, there was no generation of aerosol. This problem was solved by equalising pressures at the nebulizer inlet and the space above the liquid in the reservoir by connecting an air line to the top of the reservoir (shown in Figure 3.3). The

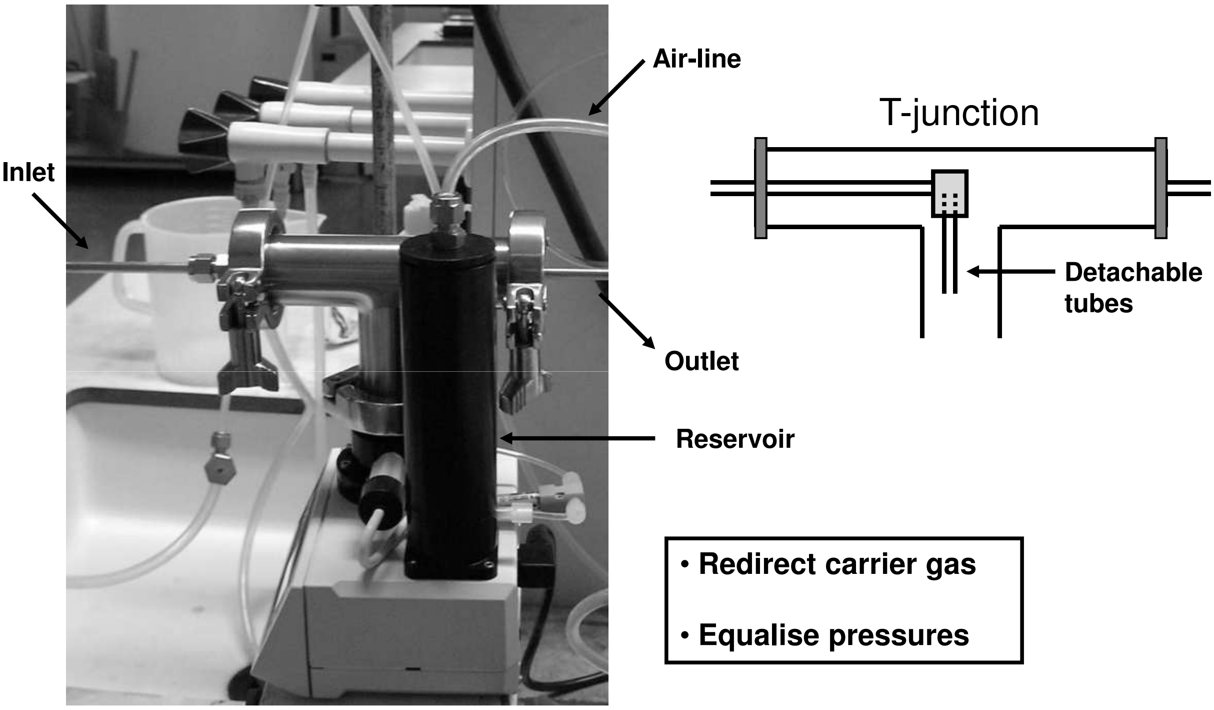

Figure 3.3: Retrofitted parts of the Ultrasonic nebulizer

final configuration allowed continuous generation of aerosol.

Reasons for switching from Ultrasonic to TSI atomizer

Earlier experiments using colloidal nanoparticle solutions performed with the Sonaer 241PG Ultrasonic nebulizer were successful. Nearly spherical nanoparticle agglomerates were obtained using a colloidal nanosilica solution (nominal particle size = 7 nm) with a surface area of 133 m^2/g (see APPENDIX-A). However, using a precursor solution consisting of tetra-ethyl orthosilicate and surfactant, led to foam production (due to vigorous agitation of the surfactant during the nebulization process), and no product was produced. The foaming problem was solved by adding ethanol to the precursor. However, the resulting solution could not be nebulized. In this case, on operating the nebulizer, only a fountain of coarse droplets was generated and no fine mist was produced. Another precursor solution was prepared with just sufficient ethanol to prevent foaming but led to the same result. Possible reasons for this occurrence could be the strong influence of precursor viscosity and surface tension on the nebulization process. The ultrasonic atomization process involves a generation of waves by a piezoelectric crystal vibrating at a very high frequency, which leads to cavitation, resulting in the production of fine droplets. The chemical composition utilized alters the liquid surface tension and viscosity, affecting the cavitation process, and hindering the production of fine droplets. Hence, it was decided to use an atomizer with a different working principle - the TSI 3076 Atomizer.

TSI 3076 Atomizer

The TSI 3076 Atomizer is shown in Figure 3.4. Compressed air expands through an orifice to form a high-velocity jet. Liquid is drawn into the atomizing section through a vertical passage and is then atomized by the jet. The droplets impinge on the wall, where large ones are removed, and impaction causes the formation of small droplets. Excess liquid is drained at the bottom of the atomizer assembly block. A fine spray leaves the atomizer through a fitting at the top.

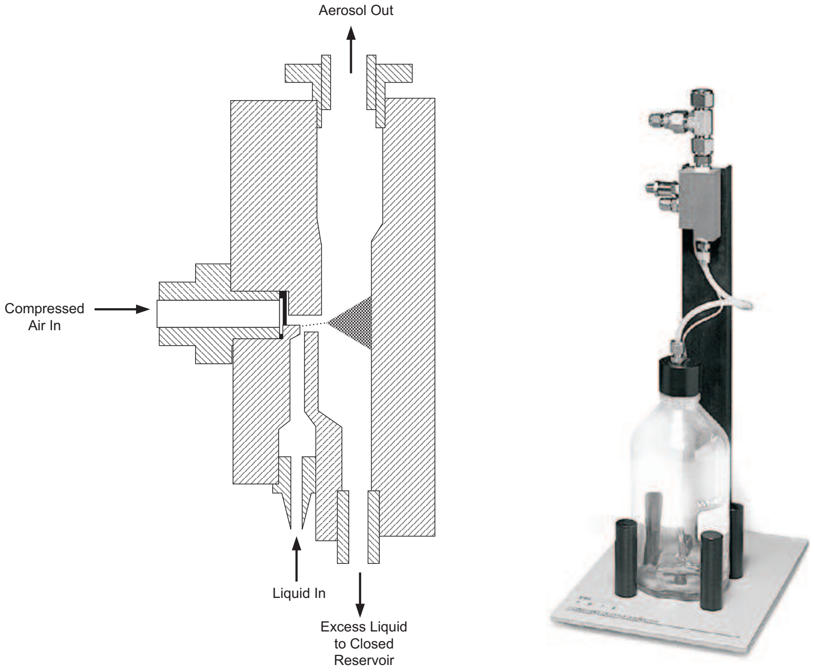

Figure 3.4: TSI 3076 Atomizer [15]

BGI Inc. Collison Atomizer

In spite of the successful operation of the TSI 3076 atomizer, we found it difficult to repeatedly clean some parts of the equipment, due to the difficulties to access them.

We then switched to the BGI Inc. Collison atomizer, which operates on a similar principle, but has a much simpler design, as shown in Figure 3.5 (a) and (b). The device consists of a nozzle head, connected to the incoming compressed gas via a vertical hollow stem. A glass jar serves as the precursor reservoir, and there is an outlet for the aerosol. The nozzle head consists of six symmetrically placed holes, while in Figure 3.5 (b) only two are shown for the purpose of illustration. At the bottom of the nozzle piece are uniform holes, which are drilled through till the nozzle exit.

When compressed gas is passed through the device and is about to leave the nozzle, it creates a negative pressure gradient, and liquid is sucked in through the bottom of the nozzle head. The liquid mixes with the gas and exits through the nozzle as a fine jet. This jet impacts the wall of the glass jar and the coarse droplets are returned to the reservoir while the fine aerosol (gas carrying a fine mist of droplets) leaves the atomizer exit. It is of paramount importance that the nozzle is immersed in the liquid at all times to ensure continuous operation. Furthermore, the liquid level should not be too high to avoid interference with the forming jet.

The present configuration of the Collison atomizer had to be modified for continuous operation. A fine tube was attached from the top lid of the atomizer to a slit made in the nozzle head, as shown in Figure 3.6. This tube was connected to a 1/8" Swagelok connector in the atomizer lid. Liquid was subsequently fed through from a syringe pump (shown in Figure 3.6) using 60 ml BD Plastipak syringes. A metal sleeve at the bottom of the nozzle provided additional length to contact the precursor liquid.

The 6-jet atomizer generates nearly 8 l/min of aerosol at a pressure of 1 barg. Two liters per minute were passed through the reactor, and remaining excess aerosol was fed to an aerosol collector (conical flask filled with water to collect any solid matter) and then released into the fumehood.

In order to generate aerosol at low flow rates, another nozzle head was constructed in-house, based on a design by May [17]. This has a single opening for a single jet with a flow rate of 2.0 l/min operated at 1.0 barg inlet pressure.

3.2.2 Diffusion Drier

In certain experiments an in-house built diffusion drier was used to dry the droplets at room temperature. The diffusion drier consists of a cylindrical Perspex tube housing with a coaxial wire screen cylinder placed in the center. The annular space between the cylinder and the housing is filled with silica gel. One end of the silica gel drier can be opened to feed the silica gel and can be easily tightened with O-rings for a gas tight connection. As the wet aerosol flows through the inner cylinder, water vapor diffuses through the wire screen and into the silica gel. Particle loss from the aerosol is minimal, since the particles have a much smaller diffusion coefficient than the water molecules. When the gel becomes saturated with moisture, its color changes from orange to colorless, indicating that it needs to be regenerated. This can be carried out in an oven at 120°C.

3.2.3 Aerosol Reactor

A tubular oven (Model Carbolite) served as a basis for the aerosol reactor. Basically, the reactor is a hollow tube in ceramic, quartz or glass, placed inside a tubular furnace with a heated length of 100 cm. The furnace has a maximum operating temperature of 1000 °C. The furnace is divided into three zones and the temperature of each zone can be maintained using a temperature controller. Two ceramic discs (99.7 % $\mathrm{Al_2O_3}$, diameter = 104 mm, thickness = 10 mm, GIMEX technische keramiek B.V.) were modified to act as supports for the ceramic tube. Concentric circular discs of diameter 30 mm were cut out from the ceramic discs. The discs were also machined to fit within the tubular furnace.

Furthermore, each of the discs were cut into equal halves and fitted with metal strips for connecting to the furnace. The tube to be heated was placed within the tubular furnace, and parallel to its axis, with the help of these ceramic discs as supports. Three different kinds of tubes were used in the experiments.

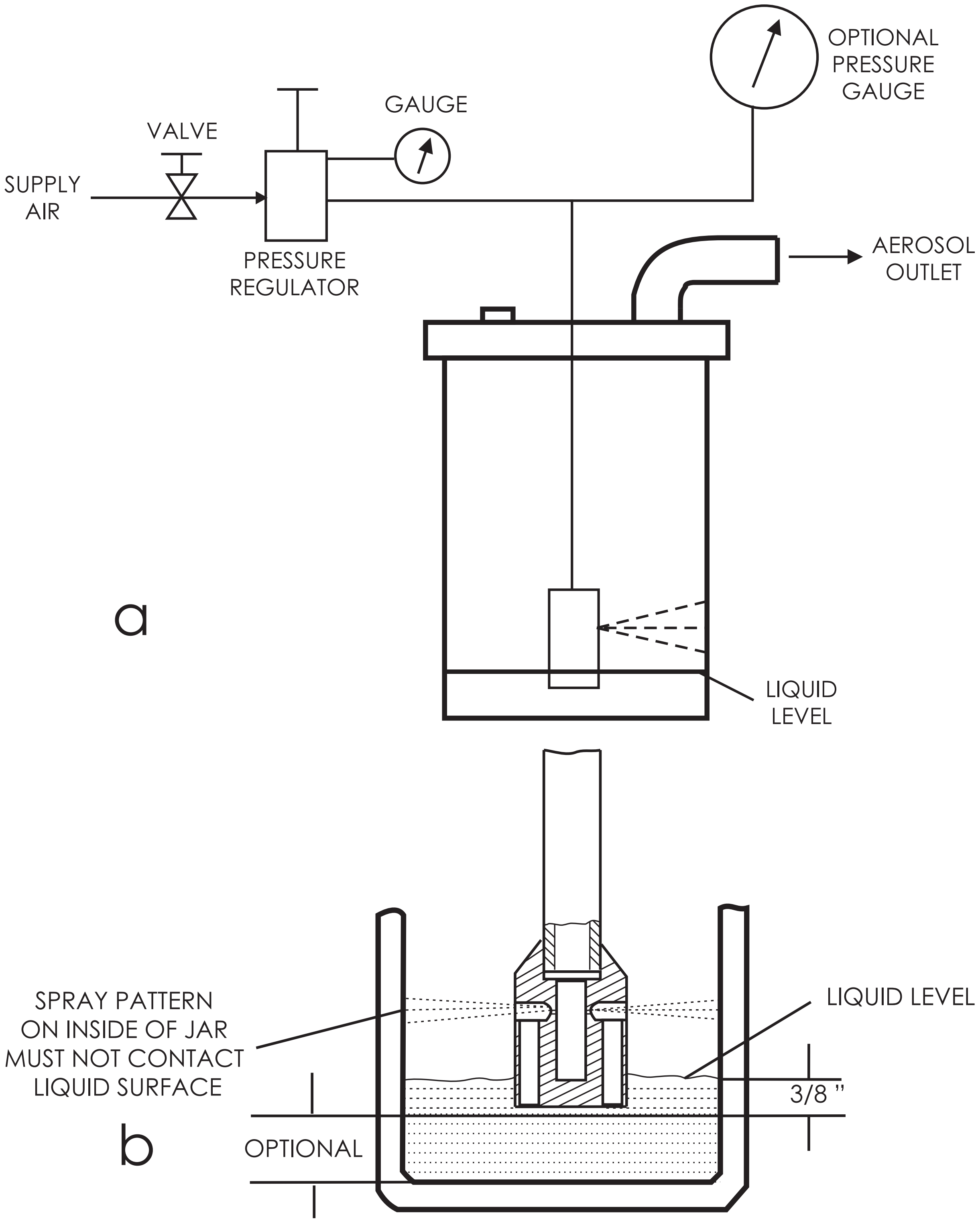

Figure 3.5: (a) and (b) BGI Inc. Collison atomizer [16]

Ceramic tube

A ceramic tube (70-75 % porous Al_2O_3) with a length of 120 cm and an inner diameter of 2.0 cm was procured from GIMEX technische keramiek B.V. The ends of the ceramic tube were

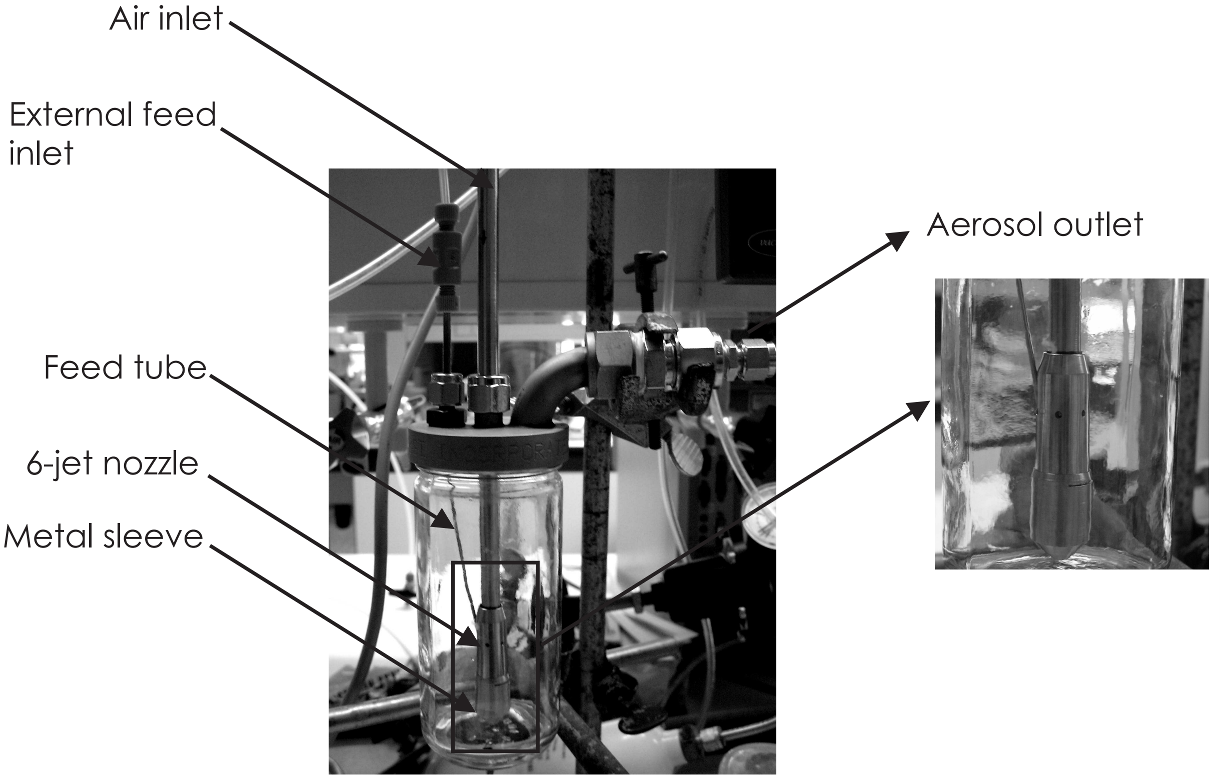

Figure 3.6: Collison atomizer with external feed connection

fitted with CF metal flanges (Hositrad B.V.), and the interface was sealed with a chemically setting cement (Sauereisen No. 29, Permacol B.V.). The inlet flange was connected with 6 mm stainless steel tubing for aerosol entry, and the flange at the other end had an opening for aerosol exit (connecting to 6 mm S.S. tubing) and for placing a thermocouple within the ceramic tube in the axial position.

Quartz/Glass tube

A quartz tube, 110 cm in length with an inner diameter of 2.0 cm, and glass flanges at its ends, was used as well. The ends of the tube were connected to the rest of the setup with KF 40 clamps. In another set of experiments a glass tube of similar dimensions was also used.

Thermocouple

A temperature profile probe with custom specifications was procured from OMEGA®. It consists of 6 k-type thermocouples with the sensing ends placed at different positions enclosed inside a stainless steel protective casing. The length of the probe was nearly 110 cm, and output leads were provided for connections to a thermocouple A/D card (Measurementcomputing®) to record the temperature online in an MS®Excel file. This allowed continuous monitoring of the axial temperature profile in the aerosol reactor. The thermocouple was placed in the axial position with the help of three ceramic supports screwed on to the thermocouple.

3.2.4 Collection filter

The resulting fine particles exiting the reactor were collected on an in-house made stainless steel aerosol filter. It consists of a Whatman®grade membrane filter (retention size of 0.45 µm) placed on a porous ceramic plate. The stainless steel housing of the filter was wrapped with a heating tape with which the temperature was kept at 80 °C.

Table 3.1 gives a brief summary of the operating conditions in the aerosol equipment.

Table 3.1: Operating conditions of aerosol equipment

Gas flow rate [l/min]	2.0
Residence time in diffusion drier [s]	9.0
Residence time in aerosol reactor [s]	9.4
Typical production capacity [mg/h]	160

3.3 Conclusions

Several atomizers were utilized to generate aerosols for nanostructured silica production. In the course of experimentation, it was observed that the Collison atomizer was best suited for the experiments as compared to the TSI atomizer and the ultrasonic nebulizer. Furthermore, an aerosol equipment consisting of an aerosol generator, aerosol reactor and collection filter was successfully constructed in-house with suitable modifications for the continuous production of nanoporous silica.

References

1. K. Okuyama, D. D. Huang, J. H. Seinfeld, N. Tani, Y. Kousaka, Chem. Eng. Sci. 46 (1991) 1545.
2. K. Okuyama, I. W. Lenggoro, Chem. Eng. Sci. 58 (2003) 537.
3. W. H. Suh, K. S. Suslick, J. Am. Chem. Soc. 127 (2005) 12007.
4. G.D. Ulrich, Combust. Sci. Tech., 4 (1971) 47.
5. H.G. Schiebel, J. Posrstendorfer, J. Aerosol Sci. 14 (1983) 113.
6. M. Suzuki, M. Kagawa, Y. Syono, T. Hirai, J. Mater. Sci. 27 (1992) 679.
7. H. Gleiter, Prog. Mater. Sci. 33 (1989) 223.
8. N. Tohge, M. Tatsumisago, T. Minami, K. Okuyama, M. Adachi, and Y. Kousaka, J. Am. Ceram. Soc. 74 (1991) 2112.
9. K. Okuyama, I.W. Lenggoro, N. Tagami, S. Tamaki, and N. Tohge, J. Mater. Sci. 32 (1997) 1229.
10. Y.C. Kang, S.B. Park, I.W. Lenggoro, and K. Okuyama, J. Mater. Res. 14 (1999) 2611.
11. F. Iskandar, Mikrajuddin, and K. Okuyama, Nanoletters 2 (2002) 389.
12. F. Iskandar, Mikrajuddin, and K. Okuyama, Nanoletters 1 (2001) 231.
13. G. Biodne, Imprimerie Royale Turin, (1829) 1.

14. F. Savart, Ann. Chim. Phys. 53 (1833) 337.
15. Instruction manual, TSI 3076 Constant output atomizer (2005).
16. Instruction manual, BGI Inc. Collison nebulizer (2002).
17. K. R. May, J. Aerosol Sci., 4 (1973) 235.

Chapter 4

Preliminary Studies on the Production of Nanostructured Porous Silica by Evaporation-Induced Self-Assembly of Aerosols

4.1 Introduction

Surfactant templated nanostructured materials have attracted considerable attention, owing to their unique properties such as a controllable pore structure, a high surface area and a narrow pore size distribution, which make these materials potential candidates for applications in heterogeneous catalysis, chromatography, controlled drug release, and optical applications [1-2].

Ordered mesoporous materials with well-defined pore sizes [3], such as MCM-41 and SBA-15 [4], have been widely synthesized via self-assembly of cationic or non-ionic surfactants and oligomeric silica under batch conditions. The process is usually conducted over a period of several days to obtain a high degree of order of the pores in the final inorganic material. A novel, rapid synthesis approach [5], namely, aerosol-assisted evaporation-induced self-assembly (EISA), allows the production of mesostructured particles within a process time of only several seconds, much shorter than the conventional approach. The EISA route combines the simplicity of the sol-gel process with the efficiency of surfactant self-assembly, allowing rapid synthesis of mesostructured thin films, particles, and arrays with controlled morphology and mesostructure [6,7]. The process is continuous and scalable. Particles can be synthesized over a wide size range by controlling the operating conditions. The particles are generally spherical, which frequently has advantages for subsequent powder handling and processing. The non-equilibrium feature of the EISA process allows the incorporation of various non-volatile components such as

---

This chapter is based on the following publication:
R. Pitchumani, A. Schmidt-Ott, M.-O. Coppens, *Proceedings of the* 5^{th} *World Congress on Particle Technology*, Florida, USA, April 2006

functional organic molecules, particles and polymers within the self-assembled mesostructures, providing a general and flexible approach for nanocomposite fabrication [8]. An interesting feature from the perspective of material synthesis is that the method enables the uniform incorporation into every synthesized particle of chemical species that can be dissolved or dispersed into a precursor solution.

Figure 4.1 shows the schematic diagram of the mechanism of formation in the EISA process. Starting with aerosol dispersion of the precursor solution using an atomizer, solvent evaporation creates a radial gradient of surfactant concentration within each droplet that steepens in time [9]. This enrichment of the surfactant induces silica-surfactant self-assembly. The radial concentration gradient and presence of the liquid-vapor interface (which serves as a nucleating surface) promotes silica hydrolysis and condensation reactions forming structured powders. Subsequent calcination of the powder for surfactant removal leads to mesostructured particles with a high surface area. The process is continuous and scalable, and the product particle size distribution can be controlled by tuning the operating conditions. This aerosol scheme generates precursor droplets with a size of several micrometers, each with an identical composition, making this approach particularly attractive for the uniform incorporation of active metal species in the silica framework [5,10].

Here, we report on the aerosol synthesis of porous silica particles with large mesopores of a controlled size using micelles of a non-ionic block copolymer surfactant as a template.

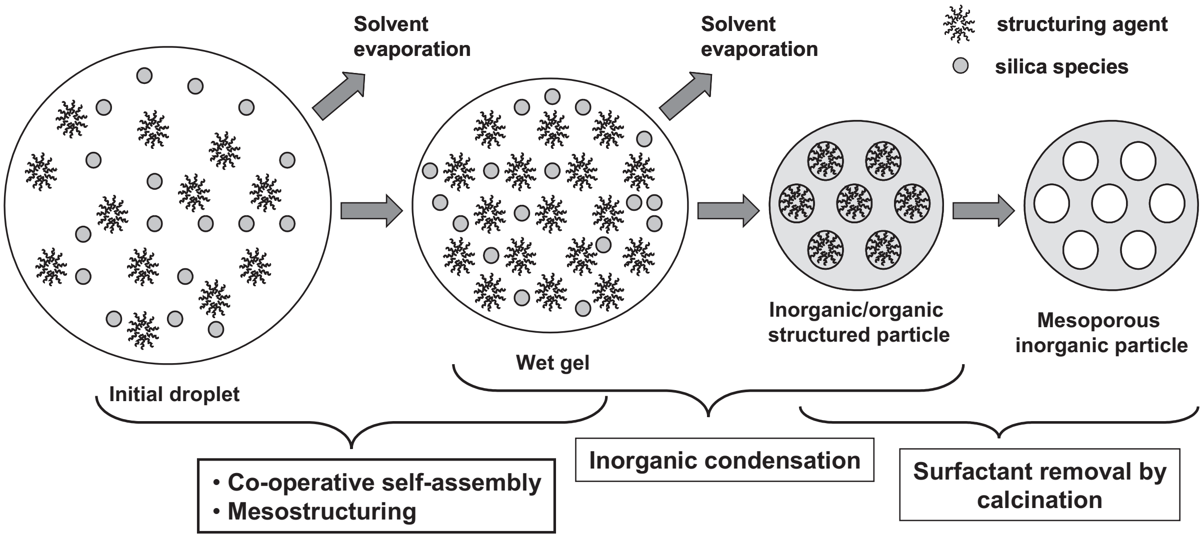

Figure 4.1: Schematic diagram of the EISA process (adapted from [7])

4.2 Experimental

4.2.1 Experimental setup

The schematic arrangement of the spray pyrolysis apparatus is shown in Figure 4.2. An atomizer produces a constant stream of fine droplets. Two models were used, a TSI 3076 atomizer (operated at 1.5 barg) and a BGI Inc. Collison nebulizer (operated at 1.0 barg), as described in chapter 3 (section 3.2.1). Droplets were transported by a carrier gas through a silica gel drier, followed by a three-zone tubular furnace. The obtained powder was collected on a filter maintained at 60-80 °C by a heating tape to prevent condensation of water vapor. The flow rate of the carrier gas (air) through the tubular reactor was kept constant at 2.0 l/min by using a mass flow controller and pump installed after the collection filter.

4.2.2 Synthesis Procedure

The precursor solution for the aerosol experiments was composed of a silica source (tetraethoxy silane, TEOS), a non-ionic surfactant (tri-block copolymer $\mathrm{EO_{20}PO_{70}EO_{20}}$, P123), HCl, deionized water and ethanol (EtOH). A typical solution was prepared by first dissolving P123 in a mixture of ethanol and water (pH adjusted to pH = 1.2 using HCl). TEOS was then added, and the mixture was stirred at room temperature for 1 h to obtain a homogeneous solution. The precursor solution remained clear throughout the duration of aerosol generation.

The molar composition of the starting solution and the corresponding furnace temperatures used for the experiments are given in Table 4.1. The temperature set points of the furnace heating zones were increased in steps to ensure a gradual heating of the incoming droplets. The powders obtained were calcined at 250 °C for 3 h and then at 550 °C for 7 h using a heating rate of 5 °C/min to remove the organic template. Samples obtained using the TSI atomizer are denoted by prefix “T” and those produced using the Collision nebulizer are denoted by prefix “C”. Experiments were also performed in the absence of the silica gel drier (for *eg.* sample C-H-2-ND).

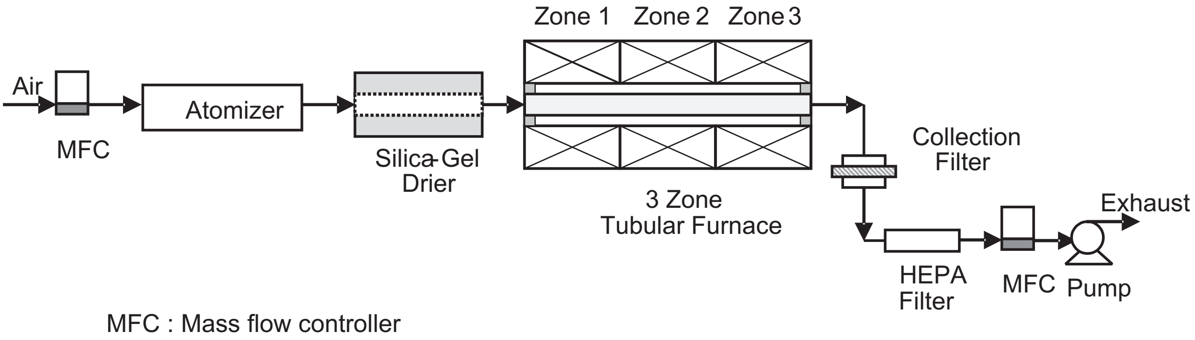

Figure 4.2: Experimental apparatus

4.2.3 Material characterization

The calcined samples were analyzed using nitrogen adsorption and desorption. The isotherms were measured using a Quantachrome Autosorb-6B sorption analyzer. Prior to the isotherm measurements, the samples were degassed at 350 °C overnight.

Powder X-ray diffraction (XRD) patterns of products obtained were recorded using a Bruker D8 Discover diffractometer with a Cu Kα X-ray source (λ_{Cu} = 0.154 nm).

Scanning electron microscopy (SEM) images of samples were obtained with a JEOL JSM 6500F microscope.

High resolution transmission electron micrographs (HRTEM) were made using a Philips CM30T electron microscope with a LaB_6 filament as the electron source, operated at 300 kV. Samples were mounted on a microgrid carbon polymer, which was fixed on a copper/nickel grid.

4.3 Results and Discussion

There are several operating variables involved in the production of nanostructured particles. Hence experiments were conducted to discover the variables to be studied in more detail in the next Chapter. The most important characteristics, such as surface area, pore volume and pore diameter were estimated for the particles produced.

Table 4.1 shows the experiments conducted to find the effect of different nebulizers and the use of the silica gel drier. As mentioned earlier, two types of nebulizers, namely a TSI 3076 atomizer (T) and a Collison atomizer (C), were used.

Table 4.1: Effect of P123/TEOS, the type of nebulizer, and the silica gel drier

Ref.	P123/TEOS [-]	S^a_{BET} [m^2/g]	V^b_t [cm^3/g]	d^c_{BJH} [nm]	Remarks
T-H-1	0.008	248	0.46	11.1	TSI atomizer
T-H-2	0.010	266	0.60	11.1	TSI atomizer
C-H-1	0.010	291	0.70	11.1	Collison atomizer
C-H-2-ND	0.010	290	0.70	12.8	Collison atomizer without drier

Conditions kept constant:
EtOH/TEOS =30, H_2O/TEOS = 40, HCl/TEOS = 0.0525,
T_1 = 150 °C, T_2 = 250 °C, T_3 = 350 °C,
Note: ^{a} BET surface area, ^{b} total pore volume, ^{c} BJH pore diameter.

By increasing the P123/TEOS ratio from 0.008 to 0.01, one sees a minor increase in surface area of 18 m^2/g while there is a substantial increase in pore volume from 0.46 to 0.60 cm^3/g. It is also observed in Table 4.1 that the particles produced with the Collison nebulizer have a slightly higher surface area compared to those synthesized using the TSI atomizer, even though the difference in pore volume is small. An additional experiment performed in the absence of the silica gel drier resulted in particles with nearly the same BET surface area of 290 m^2/g, but with an increase in the BJH pore size to 12.8 nm. The Collison atomizer was used in subsequent experiments, because of its simple construction and because it can be easily cleaned, in contrast to the TSI atomizer.

The effect of the furnace temperature on the textural properties was also studied. The furnace is divided into three zones, and temperatures were adjusted as shown in Table 4.2. T_1 stands for the temperature in the first or initial zone, T_2 for that in the middle zone and T_3 for the temperature in the final zone of the furnace.

It can be inferred from Table 4.2 that the temperature of the furnace has a significant effect on surface area and pore volume. Surface area, pore volume and average pore diameter all increase

Table 4.2: Effect of furnace temperature

Ref.	T_1 [°C]	T_2 [°C]	T_3 [°C]	S_{BET} [m^2/g]	V_t [cm^3/g]	d_{BJH} [nm]	Remarks
C-H-3-ND	80	90	100	85	0.14	7.3	Collison atomizer without drier
C-H-4-ND	50	150	250	269	0.56	11.2	Collison atomizer without drier
C-H-2-ND	150	250	350	290	0.70	12.8	Collison atomizer without drier

Conditions kept constant:
P123/TEOS = 0.01, H_2O/TEOS = 40, EtOH/TEOS = 30, HCl/TEOS = 0.0525.

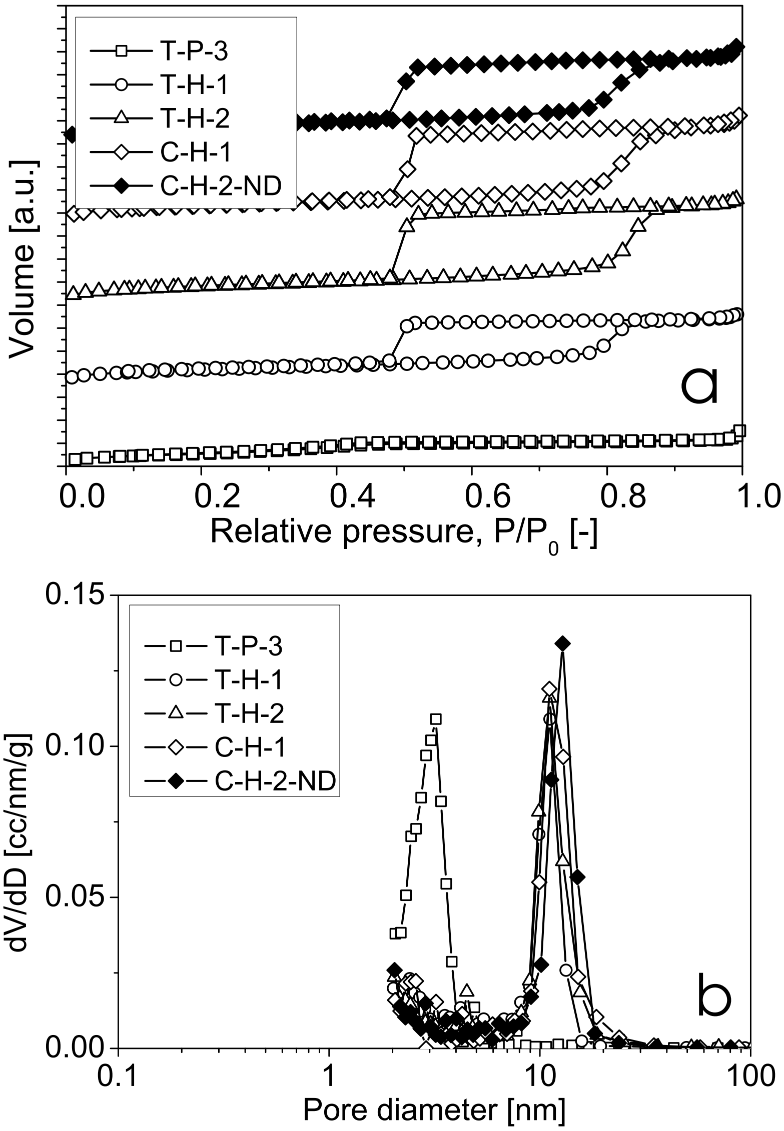

Figure 4.3: (a) N_2 adsorption/desorption isotherms, and (b) pore size distributions of samples (obtained by applying the BJH model to the adsorption branch of the isotherm)

upon increasing the temperature in the furnace.

Figure 4.3 shows the N_2 adsorption/desorption isotherms and the corresponding pore size distributions of the synthesized materials, estimated using the BJH method on the adsorption isotherms. The solutions prepared using a strong acid (HCl) led to particles with nitrogen adsorption isotherms of type IV with a large hysteresis of type H1 [11]. The hysteresis in the isotherms is typical of non-cylindrical pore systems with a pore opening that is smaller than the inner diameter of the pore [12]. An experiment performed with a weak acid (H_3PO_4, ref. no. T-P-3) led to very low surface area silica.

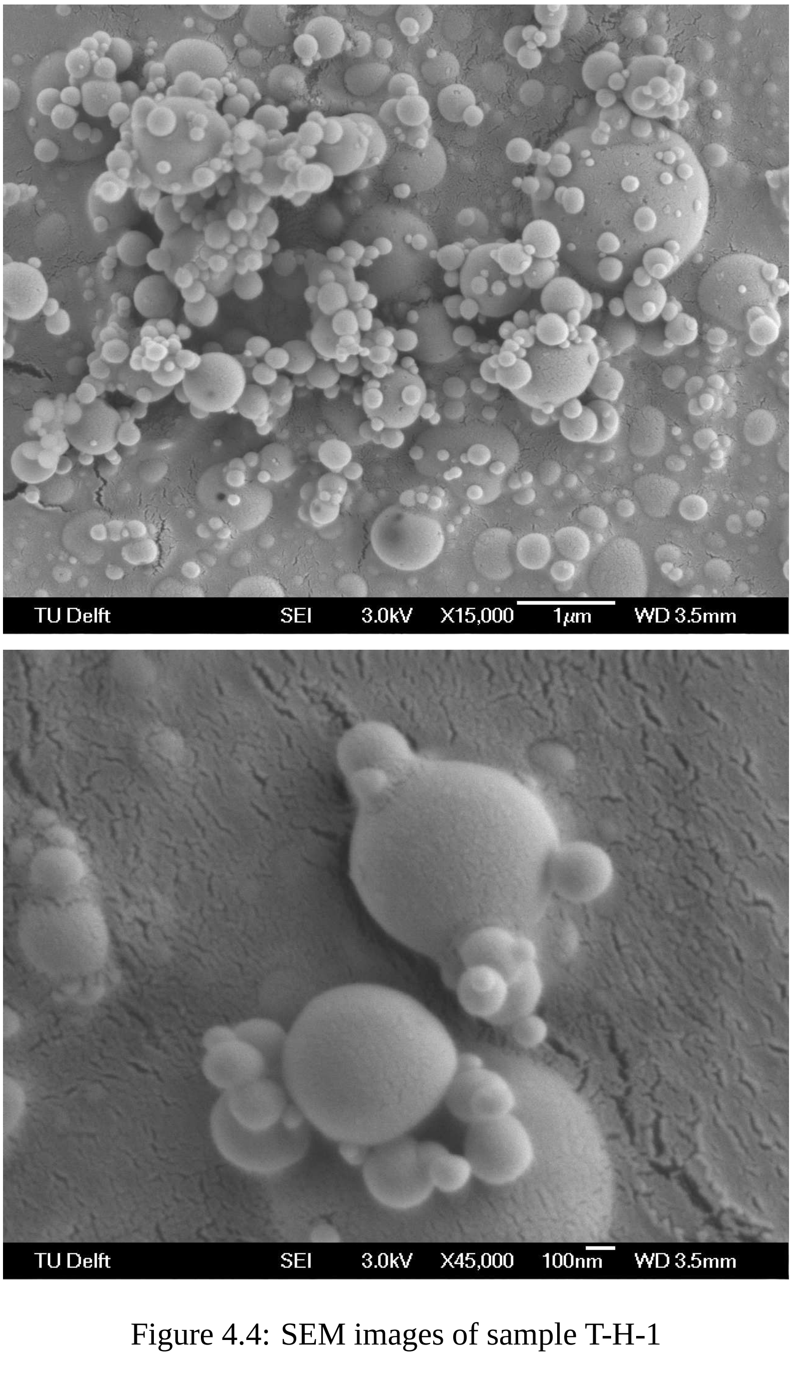

Figure 4.4: SEM images of sample T-H-1

SEM images of the powders show smooth spherical particles in the size range of 0.05 - 1.5 µm, independent of the atomizer used. Figure 4.4 shows sample T-H-1, as a representative example. The broad distribution in particle size is due to the polydisperse nature of the initial droplet distribution generated by the atomizers. If desired, it could be narrowed by using other spraying methods, but this is not the immediate objective of this work.

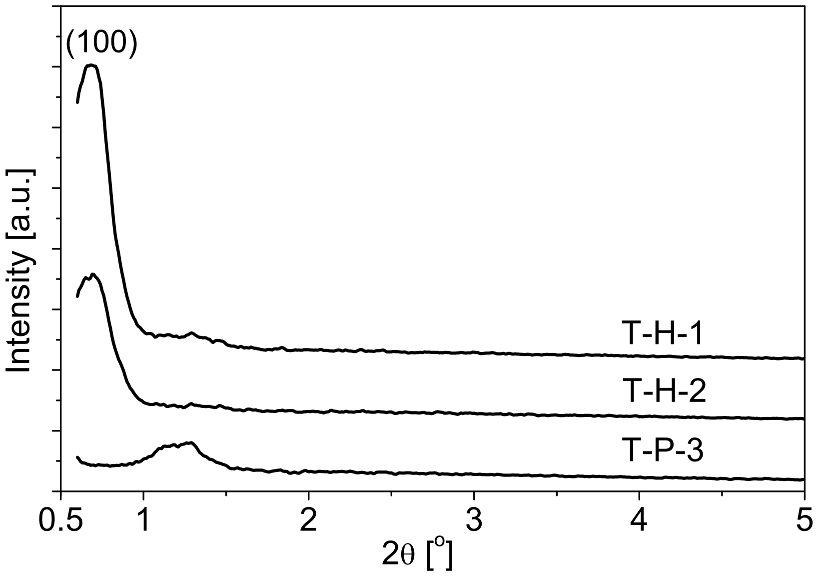

Figure 4.5: XRD patterns of samples T-P-3, T-H-1 and T-H-2

XRD analysis of particles generated from solutions containing HCl (T-H-1 and T-H-2) exhibit a strong peak corresponding to a (100) reflection with a d-spacing of 13 and 12.8 nm, respectively (Figure 4.5). Hampsey *et al.* [6] observed a similar strong (100) peak (in addition to a weak (200) reflection) in the diffraction patterns of mesoporous metal-$\mathrm{SiO_2}$ particles synthesized using the aerosol process. The sample prepared using a precursor containing phosphoric acid (T-P-3) showed a single weak diffraction peak indicating a low degree of ordering of the pore channels.

The internal pore structure of the particles is further revealed by TEM images (Figure 4.6). The core of the spherical particles seems to consist of a wormlike structure, surrounded by a silica skin [13]. The presence of micropores in the silica skin may lead to delayed desorption of $\mathrm{N_2}$ at low relative pressures (see Figure 4.3a). The TEM image of sample C-H-2-ND (Figure 4.7) shows two distinct pore structures within a single particle. The inner core consists of disordered pores, while, at the edges, the pores seem to be aligned parallel to the surface due to the spherical nature of the particles. Should this model be correct, core-shell, mesostructured particles synthesized in this way might serve as excellent delivery devices for controlled drug release schemes and for encapsulation of active metal nanoparticles. TEM images have to be interpreted with care: it is very difficult to ascertain the three-dimensional structure of complex particles from two-dimensional projections. Three-dimensional TEM can be more revealing, although, also here, the interpretation is based on the reconstruction of a three-dimensional image from two-dimensional projections. Preliminary 3D TEM “videos”, in collaboration with Ziese and Zandbergen (not shown here), display areas of local order, with, for the investigated particles, locally approximately parallel, curved pore bundles packing the interior of the spheres, and the outermost pores parallel to the sphere’s surface.

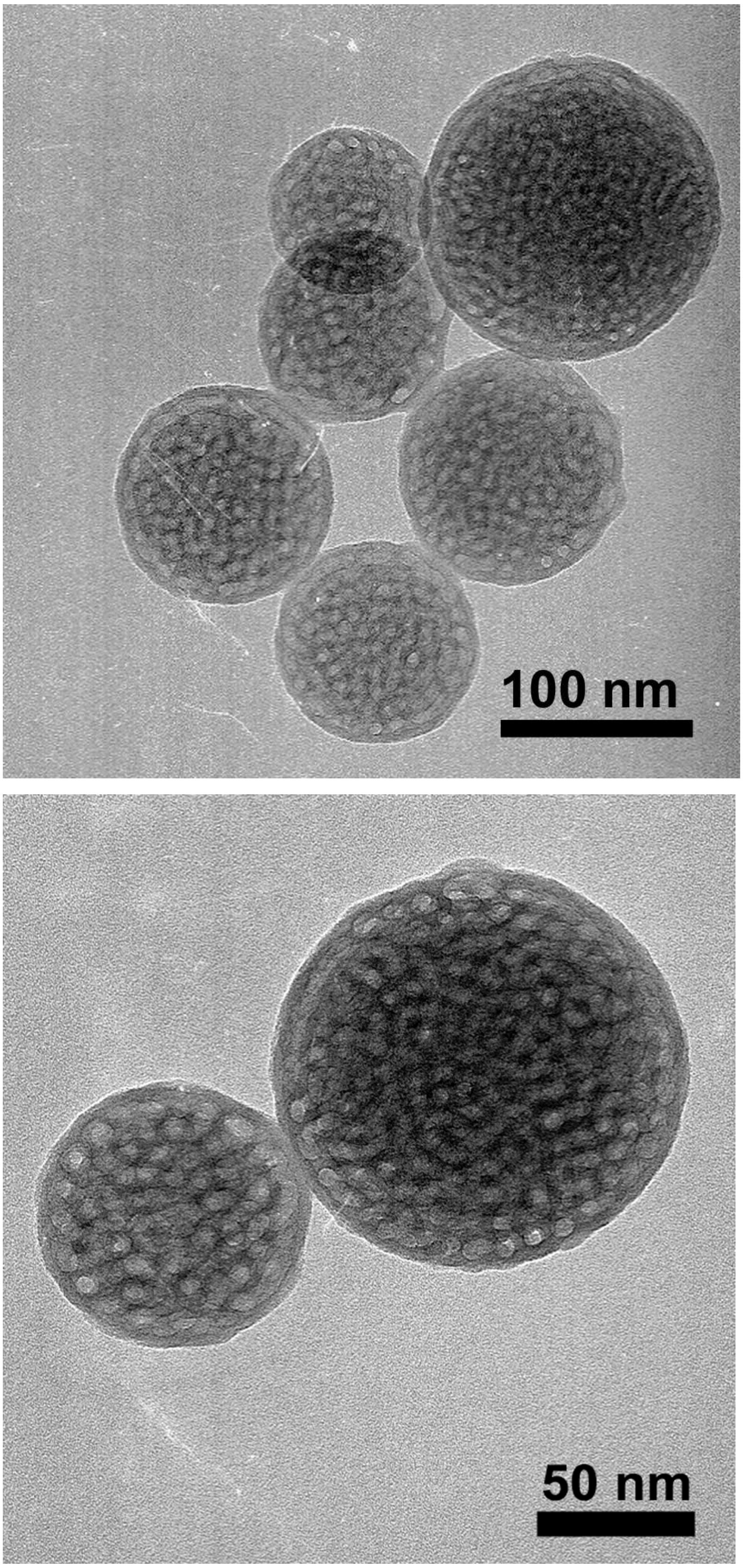

Figure 4.6: TEM images of particles (T-H-1)

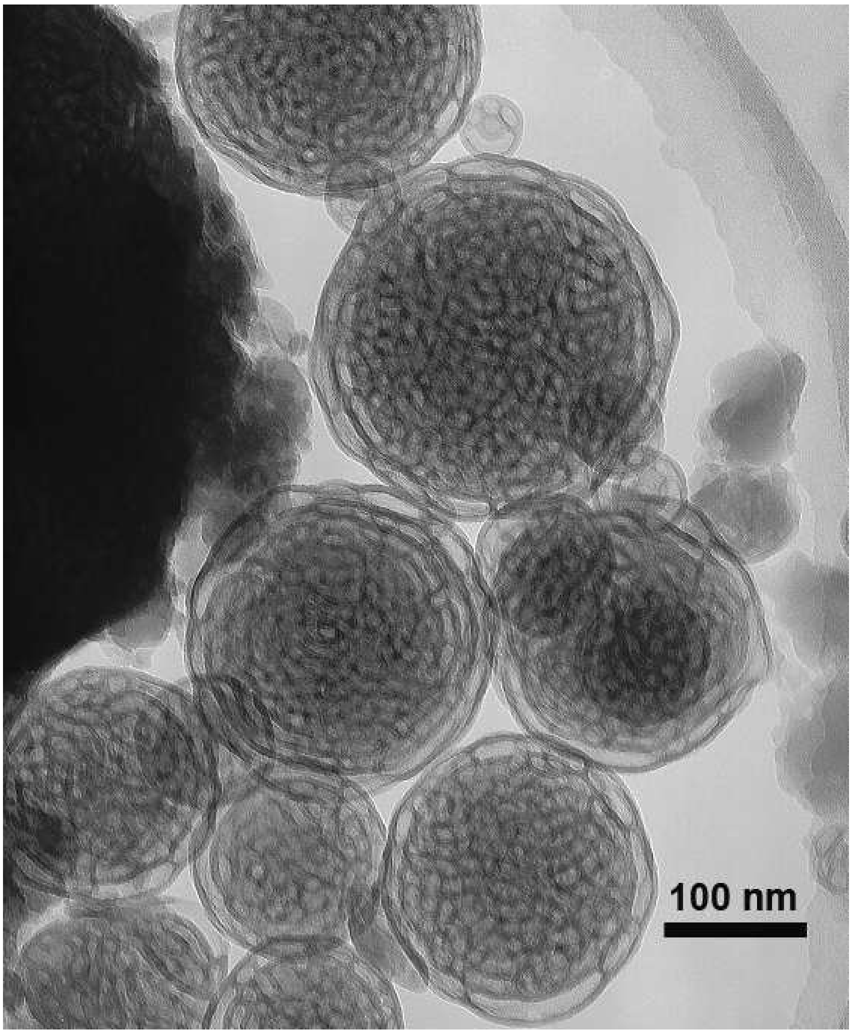

Figure 4.7: TEM image of mesoporous silica (C-H-2-ND)

4.4 Conclusions

Spherical nanoporous silica particles with a large pore size were synthesized through an aerosol-assisted process. The robust nature of this continuous aerosol process can be exploited to produce hierarchical porous materials with a tunable pore network. The present preliminary study indicates that it is necessary to adopt a more rigorous experimental procedure to fully understand the effect of the different experimental conditions on the textural properties of the synthesized particles. The next Chapter presents more experimental results, and discusses the use of a statistical factorial design methodology to investigate which combinations of variables affect the texture.

References

1. H. Fan, F. Van Swol, Y. Lu, C. J. Brinker, J. Non-Crys. Solids 285 (2001) 71.
2. M. T. Bore, S. B. Rathod, T. L. Ward, A. B. Datye, Langmuir 19 (2003) 256.

3. C. T. Kresge, M. E. Leonowicz, W. J. Roth, J. C. Vartuli, J. S. Beck, Nature 359 (1992) 710.
4. D. Zhao, J. Feng, Q. Huo, N. Melosh, G. H. Fredrickson, B. F. Chmleka, G. D. Stucky, Science 279 (1998) 548.
5. Y. Lu, H. Fan, A. Stump, T. L. Ward, T. Rieker, C. J. Brinker, Nature 398 (1999) 223.
6. J. E. Hampsey, S. Aresnault, Q. Hu, Y. Lu, Chem. Mater. 17 (2005) 2475.
7. N. Baccile, D. Grosso, C. Sanchez, J. Mater. Chem. 13 (2003) 3011.
8. Y. Lu, H. Fan, N. Doke, A. D. Loy, R. A. Assink, D. A. LaVan, C. J. Brinker, J. Am. Chem Soc. 122 (2000) 5258.
9. C. J. Brinker, Y. Lu, A. Sellinger, H. Fan, Adv. Mater. 11 (1999) 579.
10. M. T. Bore, R. F. Marzke, T. L. Ward, A. K. Datye, J. Mater. Chem. 15 (2005) 5022.
11. M. Kruk, M. Jaroniec, Chem. Mater. 13 (2001) 3169.
12. P. I. Ravikovitch, A. V. Neimark, Langmuir 18 (2002) 9830.
13. H. Fan, F. Van Swol, Y. Lu, C. J. Brinker, J. Non-Crys. Solids 285 (2001) 71.

Chapter 5

Statistics-Aided Optimal Design of a Continuous Aerosol-Based Synthesis of Nanostructured Silica Supports

5.1 Introduction

Mesoporous materials with tunable pore sizes in the range of 2-50 nm have attracted great interest among the scientific community, owing to their potential applications in catalysis, adsorption, chromatographic and membrane separation, controlled drug release, and optics. Vinu *et al.* [3] have recently reviewed new methods for the synthesis of new families of nanostructured materials. Ordered mesoporous materials with well-defined pore sizes, such as MCM-41 [4] and SBA-15 [5,6], are typically synthesized via self-assembly of cationic or non-ionic surfactants and oligomeric silica under batch conditions. The process is usually conducted over a period of several days to obtain a high degree of order in the final inorganic framework.

An alternate, rapid synthesis approach, namely aerosol-assisted evaporation-induced self-assembly (EISA), was introduced by Lu *et al.* to produce mesostructured particles within a process time of only a few seconds [7]. This approach has been used to synthesize spherical particles with well-ordered mesopores in a hexagonal, cubic, and vesicular topology, using different structure directing agents as templates [8-10]. The process is continuous and scalable, and the product particle size distribution can be controlled by tuning the operating conditions. This aerosol scheme generates precursor droplets with a size of several micrometers, each with an identical composition, making this approach particularly attractive for the uniform incorporation of active metal species (e.g. Al, Zr) in the silica framework [7,11] or deposited in the form of nanoparticles in the mesoporous silica pore structure [12]. Another advantage is the ability to easily synthesize spherical particles. Brinker and co-workers [13] utilized this aerosol method to demonstrate the rapid synthesis of continuous, mesostructured thin films with easily

---

This chapter is based on the following publications:
R. Pitchumani, A. Schmidt-Ott, M.-O. Coppens, J. Nanosci. Nanotech. (2008) *(accepted)*.

controllable mesostructures on large-scale planar and non-planar substrates as compared with the dip-coating or spin-coating processes. Bore *et al.* [14] used spherical mesoporous silica particles prepared by EISA as templates to form Pt nanowires suitable for gas phase catalytic reactions.

The sol-gel synthesis of SBA-15 involves the use of a tri-block copolymer, P123 ($EO_{20}PO_{70}EO_{20}$) as a template. P123 is a non-ionic surfactant, consisting of blocks of ethylene oxide (EO) and propylene oxide (PO). This surfactant forms cylindrical micelles, which act as a template. Apart from the fact that SBA-15 can be synthesized in a variety of morphologies [15-19], it has special features such as tunable large mesopores, and relatively high hydrothermal stability [20] owing to thick pore walls, making it particularly attractive as heterogeneous catalyst support [21]. Hence, we selected this template for our present experiments. However, despite the attractiveness of the EISA method to generate mesostructured silicas using P123 as the structuring agent, systematic studies on the effects of experimental conditions are lacking. Conventional studies typically involve varying a single parameter, keeping all other conditions constant. Such a methodology, however, requires a large number of experimental trials, since so many experimental parameters could be varied. For example, to investigate a system with 4 experimental parameters each at 4 conditions requires 256 (= 4^4) experiments. Observed trends in product properties resulting from an arbitrary or poorly chosen subset of these conditions could be misinterpreted as a general variation over the entire range of conditions. This problem can be overcome by using a factorial experimental design to conduct the experiments [22,23]. A 2-level, 4-parameter factorial design requires only 16 (= 2^4) experimental trials, and these data could be effectively processed using appropriate statistical procedures to derive useful information, such as identifying the important variables with respect to a particular property, and the sensitivity of the property to those variables. Tagliabue *et al.* [24] employed a factorial design strategy with a stepwise linear discriminant analysis to investigate the effect of seven variables on the formation of MFI zeolite. They identified the $SiO_2 : Al_2O_3$ ratio as the most influential synthesis variable. A factorial design methodology has also been applied to study the alcoholysis transformation promoted by cutinase on NaY zeolite, involving a large number of parameters, such as temperature, buffer molarity, pH of the enzyme solution, and alcohol concentration, so as to determine the main effects and their interactions [25].

In the present work, we study the synthesis of mesostructured silica particles using P123 as the only structure-directing agent, by employing a factorial design methodology to determine the significance of furnace temperature and precursor composition (P123/TEOS, H_2O/TEOS, and EtOH/TEOS ratios) on the textural properties of the products.

5.2 Experimental

5.2.1 Experimental apparatus

The aerosol apparatus schematically shown in Figure 5.1 was used to synthesize the mesoporous particles. The equipment consists of three main components - an aerosol generator, a heated tubular reactor and a collection filter.

A 6-jet Collison atomizer (BGI Inc., USA) was modified for continuous aerosol generation. The

Collison atomizer consists of a 6-jet nozzle attached to a metal stem immersed in a reservoir of liquid to be sprayed. When compressed gas is passed through the gas inlet, the gas expands as it leaves the nozzle outlet creating a reduction in static pressure. This pressure reduction sucks liquid from the reservoir, which is carried along with the expanding gas in the form of a high velocity spray. The spray impacts the glass wall, and the coarse droplets return to the reservoir while the fine droplets exit the atomizer outlet in the form of an aerosol. Six symmetric jets (one for each nozzle) emanate from the atomizer and impact the glass wall. To provide a constant flow of liquid to the atomizer, an external feed adapter was fabricated in-house and connected to the nozzle through a thin metal tube. Liquid was fed to the reservoir with the help of an infusion pump (AITECS) operated at constant flow. This ensured that the nozzle was kept immersed in a layer of liquid at all times for uninterrupted operation.

A tubular furnace (VCTF-7, Vecstar Ltd.) with a heated length of 1 m was retrofitted to be used as an aerosol reactor. A quartz tube with I.D. 20 mm was fabricated and placed in the centre of the tubular furnace with the help of ceramic supports. The ends of the quartz tube were interfaced with KF flanges (Hositrad B.V.) fitted with connections for aerosol inlet and exit. The KF flanges were fastened with clamps along with O-rings for a leak tight connection.

The particles from the aerosol were collected using a particle filter. The filter consists of a membrane filter paper (Whatman^{TM}) placed on a porous disk enclosed inside a metal housing. The housing was heated with the help of a heating tape controlled by a temperature controller. A constant flow in the aerosol reactor was maintained by means of a mass flow controller (MKS Instruments) and a membrane pump at the end of the collection filter.

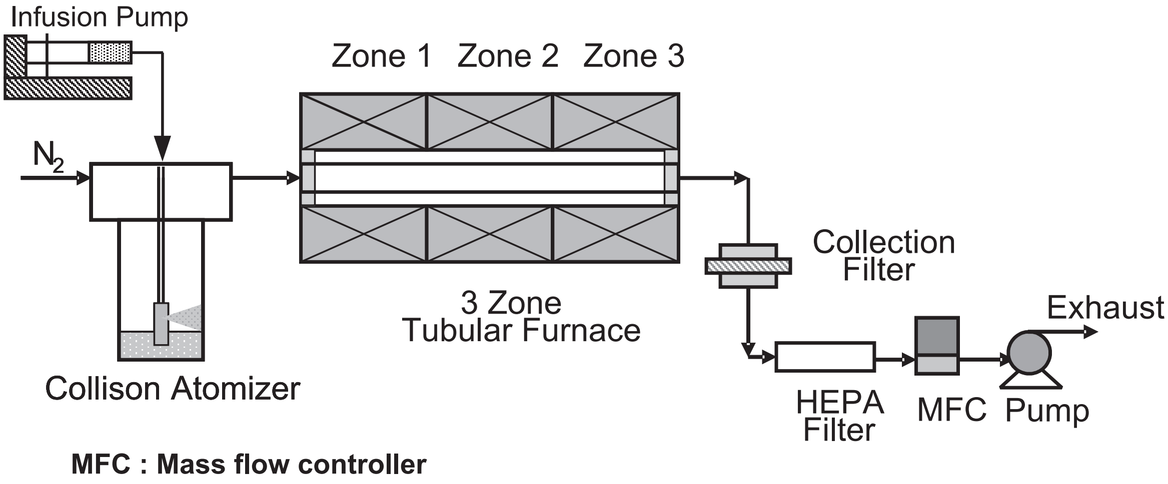

Figure 5.1: Aerosol equipment for production of mesoporous silica particles

5.2.2 Precursor preparation

The precursor solution for the aerosol experiments was composed of a silica source, tetra-ethoxy silane (TEOS), a non-ionic surfactant, Pluronic P123 tri-block copolymer ($EO_{20}PO_{70}EO_{20}$), HCl , deionized water and ethanol (EtOH) at room temperature. A typical solution was prepared by first dissolving P123 in a mixture of ethanol and water. The pH of H_2O was brought to

1.2 using HCl. TEOS was subsequently added and the mixture was stirred for 1 h at room temperature to obtain a homogeneous solution.

5.2.3 Experimental procedure

A sufficient amount of precursor solution was transferred to the glass jar of the Collison atomizer, such that the nozzle was partially immersed without obstructing the jet formation. The remaining liquid was transferred to a 50 ml syringe and placed in the infusion pump. Nitrogen as a carrier gas at 1.0 barg was passed into the Collison atomizer. The flow rate of aerosol through the heated aerosol reactor was maintained at 2.0 l/min using the mass flow controller. The excess aerosol from the atomizer was collected in an aerosol trap before releasing it into the fumehood. The precursor liquid was fed to the atomizer at 35 ml/h by adjusting the speed of the syringe pump. The synthesized particulate aerosol leaving the aerosol reactor was collected on the membrane filter heated to 80 °C. The powders collected on the filter were calcined at 425 °C for 3 h at a heating rate of 1 °C/min to remove the organic template.

5.2.4 Factorial design of experiments

The experimental conditions were obtained by using a 2^4 factorial design containing 2 levels and 4 variables (experimental parameters or factors) [26]. Three variables describe the precursor composition, expressed as molar ratios with respect to TEOS (P123/TEOS, H_2O/TEOS, EtOH/TEOS), and the fourth one is the maximum furnace temperature setpoint (T). The values of these variables are assigned to levels. The actual values of the experimental parameters are given in Table 5.1. The fractional factorial design of experiments involves the combination of these variables at different levels, and is given in Table 5.2. The first 16 experiments involving levels -1 and +1 were used for the determination of the significant variables.

Table 5.1: Experimental conditions

Levels	Factors			
	P123/TEOS, x_1 [-]	T, x_2 [^oC]	H_2O/TEOS, x_3 [-]	EtOH/TEOS, x_4 [-]
-1	0.0095	120	10.1	4.4
+1	0.018	310	34.9	25.6
$\sqrt{2}$	0.0078	80	5	0
$\sqrt{2}$	0.02	350	40	30
0	0.01375	215	22.5	15

The levels of the different factors were selected on the basis of published literature. A value of 0.0095 for the P123/TEOS ratio was typically used to obtain uniform mesopores using the aerosol scheme [7]. A much higher P123/TEOS would increase the pore volume. This led us to choose the maximum value of P123/TEOS as 0.018. Baccile *et al.* [8] showed that a maximum furnace temperature of 350 °C led to ordered mesoporous silica particles. Higher temperatures led to a reduction in structural order. Additionally, a composition of TEOS : surfactant : H_2O : EtOH = 1 : x : 40 : 30, where x ranged from 0.0035 to 0.35, was used

Table 5.2: Fractional factorial design for the four experimental variables, and the corresponding BET surface areas and pore volumes of the products obtained

S.No.	P123/TEOS, x_1 [-]	T, x_2 [^oC]	H_2O/TEOS, x_3 [-]	EtOH/TEOS, x_4 [-]	S_{BET} [m^2/g]	V_t [cm^3/g]
1	0.018	310	34.9	25.6	377	0.55
2	0.018	310	34.9	4.4	377	0.52
3	0.018	310	10.1	25.6	487	0.74
4	0.018	310	10.1	4.4	439	0.56
5	0.018	120	34.9	25.6	410	0.50
6	0.018	120	34.9	4.4	346	0.42
7	0.018	120	10.1	25.6	483	0.59
8	0.018	120	10.1	4.4	387	0.41
9	0.0095	310	34.9	25.6	355	0.70
10	0.0095	310	34.9	4.4	343	0.61
11	0.0095	310	10.1	25.6	406	0.68
12	0.0095	310	10.1	4.4	379	0.68
13	0.0095	120	34.9	25.6	286	0.50
14	0.0095	120	34.9	4.4	290	0.49
15	0.0095	120	10.1	25.6	322	0.53
16	0.0095	120	10.1	4.4	309	0.52
17	0.01375	215	22.5	15	316	0.66
18	0.02	215	22.5	15	388	0.54
19	0.0078	215	22.5	15	278	0.44
20	0.01375	350	22.5	15	305	0.71
21	0.01375	80	22.5	15	240	0.40
22	0.01375	215	40	15	313	0.62
23	0.01375	215	5	15	433	0.50
24	0.01375	215	22.5	30	306	0.53
25	0.01375	215	22.5	0	298	0.59

to generate mesostructures with different surfactants [8]. However, the effect of using a lower relative water or ethanol content or a combination thereof, was not discussed. The present study attempts to investigate these effects.

5.2.5 Material characterization

The calcined samples were analyzed using a Quantachrome™Autosorb-6B sorption analyzer to determine the nitrogen adsorption/desorption isotherms at 77 K. The samples were degassed at 100 °C prior to the measurements. The BET surface areas (S_{BET}) and the total pore volumes (V_t) measured for the products are given in Table 5.2.

Powder X-ray diffraction (XRD) patterns of products obtained were recorded using a Bruker D8 Discover diffractometer with a Cu Kα X-ray source (λ_{Cu} = 0.154 nm). Scanning electron microscopy (SEM) images of samples were obtained with a JEOL JSM 6500F microscope. High-resolution transmission electron micrographs (HRTEM) were made using a Philips CM30T electron microscope with a LaB_6 filament as the electron source, operated at 300 kV. Samples were mounted on a TEM grid consisting of a copper/nickel supported carbon polymer film.

5.3 Results and Discussion

5.3.1 Estimation of significant variables

Effect of variables on BET surface area (S_{BET})

A rigorous statistical analysis was carried out to determine the significant variables by following the procedures laid down by Yates as described in the book by Box *et al.* [22] and Daniels [27]. These methods allow analysis of experimental data in the absence of replicated runs. The first step involved the use of Yates's algorithm [22] to calculate the effects of different factors/variables and their interactions (2, 3 and 4 factors) on the BET surface area (S_{BET}) of the products. The term *effect* refers to the influence of a variable in question on the dependent variable (here being S_{BET}) over all the conditions of the other variables. More literally, it is the difference between the average value of the response (S_{BET}) of the runs at high level and the average value of the response of the runs at low level.

In order to apply Yates's algorithm, the observations given in Table 5.2 are retabulated in a standard order, such that the x_k column ($k = 1, 2, 3, 4$) alternatingly consists of 2^{k-1} times -1, followed by 2^{k-1} times $+1$, as shown in Table 5.3.

Table 5.3: Calculation of Yates's algorithm for S_{BET}

S. No.	Exp.										Divisor	Effect	
	No.	x_1	x_2	x_3	x_4	y	[x_1]	[x_2]	[x_3]	[x_4]		Estimate	Type*
1	16	-1	-1	-1	-1	309	696	1514	2870	5996	16	374.75	Average
2	8	+1	-1	-1	-1	387	818	1356	3126	616	8	77	1
3	12	-1	+1	-1	-1	379	636	1698	228	330	8	41.25	2
4	4	+1	+1	-1	-1	439	720	1428	388	-222	8	-27.75	12
5	14	-1	-1	+1	-1	290	805	138	206	-428	8	-53.5	3
6	6	+1	-1	+1	-1	346	893	90	124	-144	8	-18	13
7	10	-1	+1	+1	-1	343	696	242	-40	-90	8	-11.25	23
8	2	+1	+1	+1	-1	377	732	146	-182	-26	8	-3.25	123
9	15	-1	-1	-1	+1	322	78	122	-158	256	8	32	4
10	7	+1	-1	-1	+1	483	60	84	-270	160	8	20	14
11	11	-1	+1	-1	+1	406	56	88	-48	-82	8	-10.25	24
12	3	+1	+1	-1	+1	487	34	36	-96	-142	8	-17.75	124
13	13	-1	-1	+1	+1	286	161	-18	-38	-112	8	-14	34
14	5	+1	-1	+1	+1	410	81	-22	-52	-48	8	-6	134
15	9	-1	+1	+1	+1	355	124	-80	-4	-14	8	-1.75	234
16	1	+1	+1	+1	+1	377	22	-102	-22	-18	8	-2.25	1234

*1, 2, 3 and 4 refer to the variables x_1, x_2, x_3 and x_4 respectively.

A series of operations are performed on the dependent variable ($S_{BET} = y$) to estimate the effects of the different experimental parameters. The first 8 entries in column [x_1] are obtained by adding the successive pairs of values in column y. For example, the first 2 entries in column [x_1] are obtained as $309 + 387 = 696$ and $379 + 439 = 818$. The second 8 entries in column

$[x_1]$ can be obtained by subtracting the top number from the bottom number of each pair. Thus: $387 - 309 = 78$, and $439 - 379 = 60$, and so on. Using the same procedure, column $[x_2]$ is obtained from column $[x_1]$, column $[x_3]$ from column $[x_2]$ and finally column $[x_4]$ from column $[x_3]$. This can also be expressed mathematically, as follows:

$$[x_k]^j = [x_{k-1}]^{2i} + [x_{k-1}]^{2i-1} \quad (j = 1..8, i = 1..8, k = 1..4) \tag{5.1}$$

$$[x_k]^l = [x_{k-1}]^{2i} - [x_{k-1}]^{2i-1} \quad (j = 9..16, i = 1..8, k = 1..4) \tag{5.2}$$

where $[x_k]^{j \text{ or } i}$ is the j^{th} or i^{th} row element of the x_k column and $[x_o] = y$

The estimate of different effects is obtained by dividing the entries in column $[x_4]$ by values given under the column *divisors*. The first entry of the estimate corresponds to the grand average of all observations. The remaining estimate of the effects corresponds to single and multiple factor (interaction) effects. The type of effect can be identified by locating the "$+1$" entries in the design matrix (columns corresponding to x_1, x_2, x_3 and x_4). There are fifteen effects in all, comprising four main effects (corresponding to 1, 2, 3 and 4), six 2-factor interactions (12, 13, 14, 23, 24 and 34), four 3-factor interactions (123, 124, 134 and 234) and one 4-factor interaction (1234). The main effect of, for example, 1 (P123/TEOS) refers to the effect of P123/TEOS on S_{BET} over all the conditions of the other variables 2, 3 and 4. The value of the effect gives an indication of the extent of the influence of the factor(s) on the dependent variable, while the sign (-/+) indicates a positive or negative influence. However, it would be premature to conclude which of the effects are significant, solely on the basis of their magnitude, because experimental errors have not been accounted for yet.

This problem can be overcome by applying Daniel's technique [27] to determine the significant effects in the absence of duplicate observations. This technique is based on the use of normal probability plots. Suppose, the data had occurred as a result of random variation about a fixed mean, and changes in the levels of the variables had no real effect on the S_{BET} of the products, then the effects of the main variables and their interactions would be roughly normally distributed about zero, and would therefore fall on a straight line on a normal probability paper. The effects that deviate from the straight line are then considered to be the significant ones.

The effects obtained in Table 5.3 are sorted in ascending order (i) on the basis of their estimates as shown in Table 5.4. The percentage probability (P_i) of the occurrence of the i^{th} effect is calculated using $P_i = 100(i - 1/2)/m$ for $i = 1, 2, ...m$, where m is the total number of effects.

These effects and their probabilities are plotted on normal probability paper, as shown in Figure 5.2. Starting from the effects with magnitudes close to zero, ten of the effects cluster together and reasonably fit on a straight line, therefore can be ignored since they appear as a result of noise in the experimental observations.

The effects of any of the individual variables (P123/TEOS, T, H_2O/TEOS and EtOH/TEOS) lie away from the straight line, therefore constitute the significant effects. Here, on the basis of the magnitude of the effects, it can be seen that the order of significance of these effects is P123/TEOS $>$ H_2O/TEOS $>$ T $>$ EtOH/TEOS.

It can also been seen from Figure 5.2 that P123/TEOS, T and EtOH/TEOS have a positive effect on S_{BET}, while H_2O/TEOS has a negative effect on S_{BET} on the basis of the sign of their

Table 5.4: The 15 ordered effects and the probability points, P_i

Order no. i	Effects Estimate	Identity	P_i [%]
1	-53.5	**3**	3.3
2	-27.75	**12**	10.0
3	-18	**13**	16.7
4	-17.75	**124**	23.3
5	-14	**34**	30.0
6	-11.25	**23**	36.7
7	-10.25	**24**	43.3
8	-6	**134**	50.0
9	-3.25	**123**	56.7
10	-2.25	**1234**	63.3
11	-1.75	**234**	70.0
12	20	**14**	76.7
13	32	**4**	83.3
14	41.25	**2**	90.0
15	77	**1**	96.7

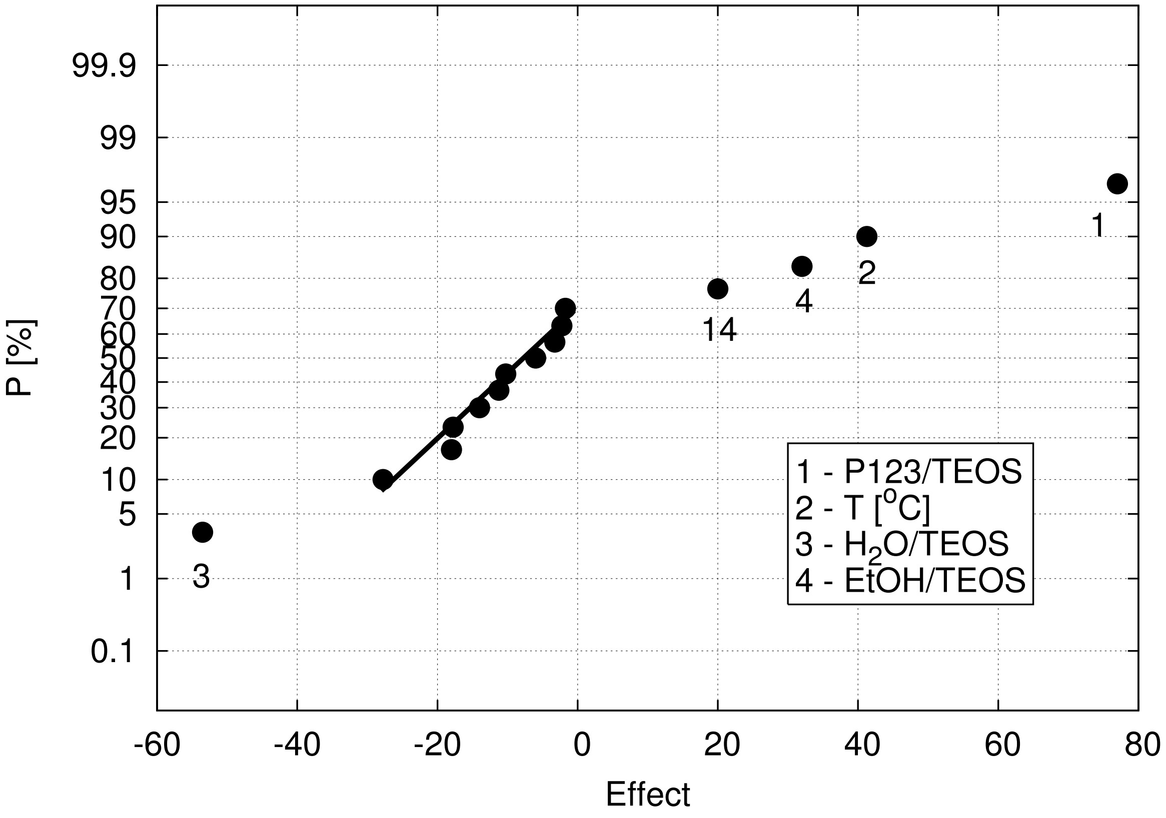

Figure 5.2: Normal probability plot of effects of different factors on S_{BET}

estimates. In other words, increasing P123/TEOS, T and EtOH/TEOS leads to an increase in surface area. On the other hand, increasing H_2O/TEOS leads to a decrease in S_{BET}. If we had to choose the two most significant main effects, they would be P123/TEOS and H_2O/TEOS.

The two-factor interaction represented by P123/TEOS × EtOH/TEOS also deviates from the straight line, hence is significant. This interaction can be represented using the two-way table illustrated in Figure 5.3. The bottom axis corresponds to P123/TEOS with their values (0.0095 and 0.018) representing the end points, while the vertical axis represents EtOH/TEOS with the corresponding values (4.4 and 25.6). The values 330, 387, 342 and 439 are obtained at the particular value of P123/TEOS and EtOH/TEOS averaged over levels of other variables. For example, the value of 330 is obtained by averaging the values of S_{BET} at P123/TEOS=0.0095 and EtOH/TEOS=4.4 over the various levels of T and H_2O/TEOS.

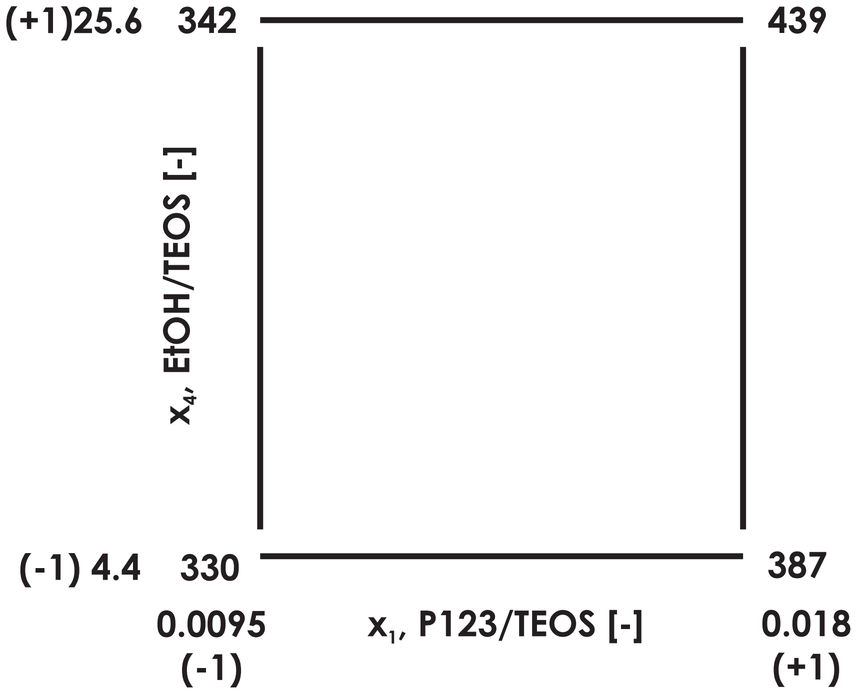

Figure 5.3: Two-way table highlighting the P123/TEOS × EtOH/TEOS interaction on S_{BET}

Generally, high P123/TEOS ratios lead to high S_{BET} values. The interaction between P123/TEOS and EtOH/TEOS occurs because, at high P123/TEOS, an increase in EtOH/TEOS leads to an increase in S_{BET} while, at low P123/TEOS, the increase in S_{BET} is comparatively much lower. This also demonstrates that the effect of EtOH/TEOS on S_{BET} is subject to the P123/TEOS used in the experiment, and one would observe different extents of variation in surface area. Such an analysis allows us to investigate trends in experimental data that are easily missed or overlooked when using the conventional form of experimentation, where the effect of a single variable (keeping other variables constant) is studied, and one is often tempted to accept this as a global variation.

Effect of variables on total pore volume (V_t)

The statistical analysis reported in the previous section was also performed to determine the significant variables with respect to the total pore volume of the products. The effects of different variables calculated using Yates's algorithm are tabulated in Table 5.5. Daniel's method was again applied to determine the significant effects, and the corresponding normal probability plot is shown in Figure 5.4.

Table 5.5: Daniel's technique using normal probability plots

Order no.	Effects		P_i
i	Estimate	Identity	[%]
1	-0.053	**1**	3.3
2	-0.053	**3**	10.0
3	-0.043	**134**	16.7
4	-0.025	**13**	23.3
5	-0.023	**12**	30.0
6	-0.02	**34**	36.7
7	-0.02	**123**	43.3
8	-0.018	**23**	50.0
9	-0.018	**1234**	56.7
10	-0.015	**124**	63.3
11	0.0025	**24**	70.0
12	0.005	**234**	76.7
13	0.045	**14**	83.3
14	0.0725	**4**	90.0
15	0.135	**2**	96.7

The effect of each of the four studied variables (P123/TEOS, T, H_2O/TEOS, EtOH/TEOS) is significant. The effects of T and EtOH/TEOS are positive, indicating that increasing these variables will result in an increase in pore volume. P123/TEOS and H_2O/TEOS, on the other hand, are observed to have a lowering effect on pore volume.

Additionally, there is significant interaction between P123/TEOS and EtOH/TEOS. Since the effects $T \times$ EtOH/TEOS and $T \times H_2O$/TEOS $\times$ EtOH/TEOS have magnitudes close to zero, they can be neglected. There is significant three-way interaction between P123/TEOS, H_2O/TEOS and EtOH/TEOS, denoted as P123/TEOS $\times$ H_2O/TEOS $\times$ EtOH/TEOS. Furthermore, on the basis of the effects' magnitudes, the two most significant variables are T and EtOH/TEOS, which lie farthest away from the straight line.

5.3.2 Effect of experimental parameters on the BET surface area (S_{BET})

A multi-variable regression analysis on the experimental data was performed to relate S_{BET} with the independent variables, using the following quadratic equation with interaction terms:

$$\begin{aligned} S_{BET} = a_0 + a_1x_1 + a_2x_2 + a_3x_3 + a_4x_4 + \\ a_{11}x_1^2 + a_{22}x_2^2 + a_{33}x_3^2 + a_{44}x_4^2 + \\ a_{12}x_1x_2 + a_{13}x_1x_3 + a_{23}x_2x_3 + a_{24}x_2x_4 + a_{34}x_3x_4 \end{aligned} \tag{5.3}$$

where, x_1, x_2, x_3 and x_4 are the experimental variables, and a_i $(i = 1..4)$, a_{jj} $(j = 1..4)$ and

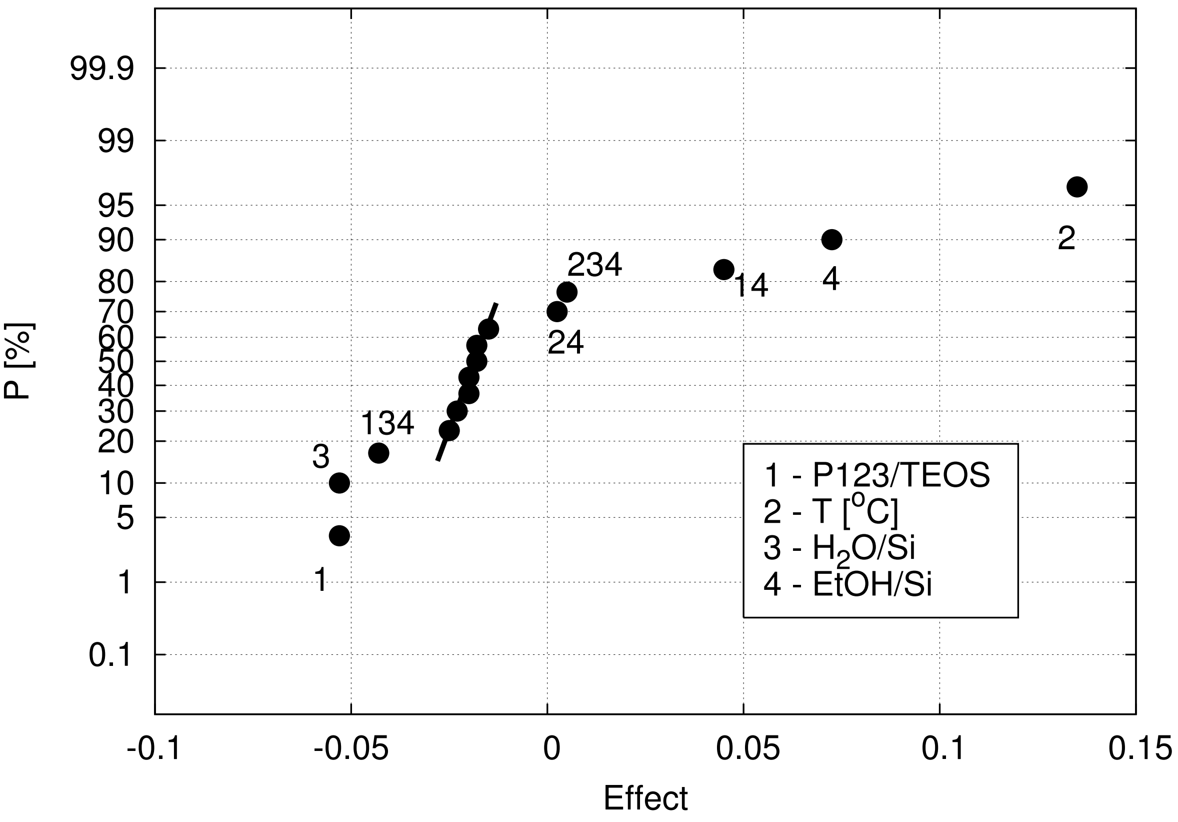

Figure 5.4: Normal probability plot for effects of different factors on V_t

a_{ij} $(i = 1..3, j = i + 1..4)$ are the corresponding coefficients. The regression was performed using a statistical software, NCSS®, to determine the values of the coefficients. The correlation coefficient, R^2, was 0.954. The values of the coefficients were substituted in Equation (5.3), resulting in:

$$\begin{aligned} S_{BET} = {} & 454.44 - 25059.23x_1 + 0.928x_2 - 12.71x_3 - 3.16x_4 \\ & + 1524017x_1^2 - 1.17 \times 10^{-4}x_2^2 + 0.322x_3^2 + 0.122x_4^2 \\ & - 34.36x_1x_2 - 170.78x_1x_3 + 221.98x_1x_4 - 4.78 \times 10^{-3}x_2x_3 \\ & - 5.09 \times 10^{-3}x_2x_4 - 5.32 \times 10^{-2}x_3x_4 \end{aligned} \tag{5.4}$$

Furthermore, Equation (5.4) could be further simplified by substituting x_1 (P123/TEOS) = 0.018 and x_1 (P123/TEOS) = 0.0095 to obtain Equation (5.5) and (5.6), respectively. This equation was used to predict S_{BET} as a function of different experimental conditions.

For x_1 = 0.018

$$\begin{aligned} S_{BET} = {} & 497.17 + 0.31x_2 - 15.78x_3 + 0.83x_4 \\ & - 1.17 \times 10^{-4}x_2^2 + 0.322x_3^2 + 0.122x_4^2 \\ & - 4.78 \times 10^{-3}x_2x_3 - 5.09 \times 10^{-3}x_2x_4 - 5.32 \times 10^{-2}x_3x_4 \end{aligned} \tag{5.5}$$

For x_1 = 0.0095

$$
\begin{aligned}
S_{BET} = {} & 353.92 + 0.6016x_2 - 14.33x_3 - 1.05x_4 \\
& - 1.17 \times 10^{-4}x_2^2 + 0.322x_3^2 + 0.122x_4^2 \\
& - 4.78 \times 10^{-3}x_2x_3 - 5.09 \times 10^{-3}x_2x_4 - 5.32 \times 10^{-2}x_3x_4
\end{aligned}
\tag{5.6}
$$

A code (see APPENDIX-B) developed in MATLAB® 7.3.0 (R2006b) uses a fine mesh grid consisting of the range of values of the independent variables along with the above equations to generate contours of S_{BET}.

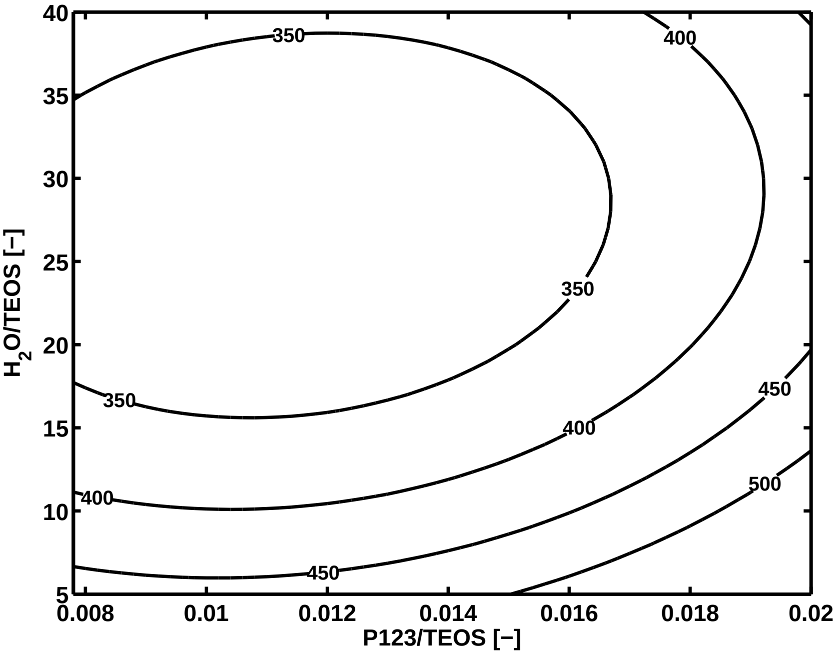

Figure 5.5: Effect of P123/TEOS and H_2O/TEOS on BET surface area at EtOH/TEOS = 25.6 and T = 310 °C

Effect of P123/TEOS on the surface area

Equation (5.4) was used to calculate the BET surface area at T = 310 °C and EtOH/TEOS = 25.6 for different values of P123/TEOS and H_2O/TEOS. The resulting contours are plotted in Figure 5.5 to illustrate the effect of P123/TEOS and H_2O/TEOS on the BET surface area.

It is observed from Figure 5.5 that the contours are elliptical. At H_2O/TEOS = 20, S_{BET}

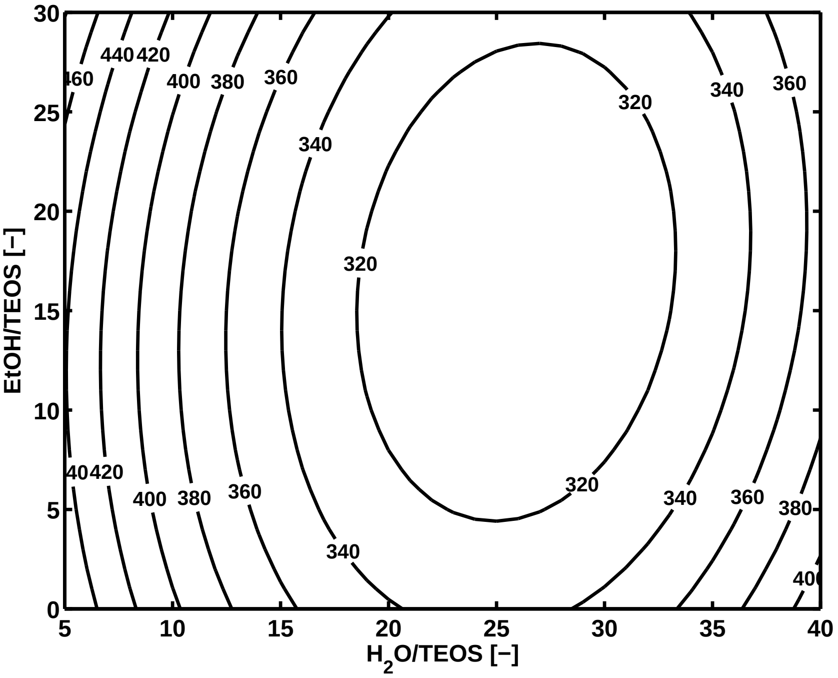

Figure 5.6: Effect of H_2O/TEOS and EtOH/TEOS on BET surface area at P123/TEOS = 0.0095 and T = 310 °C

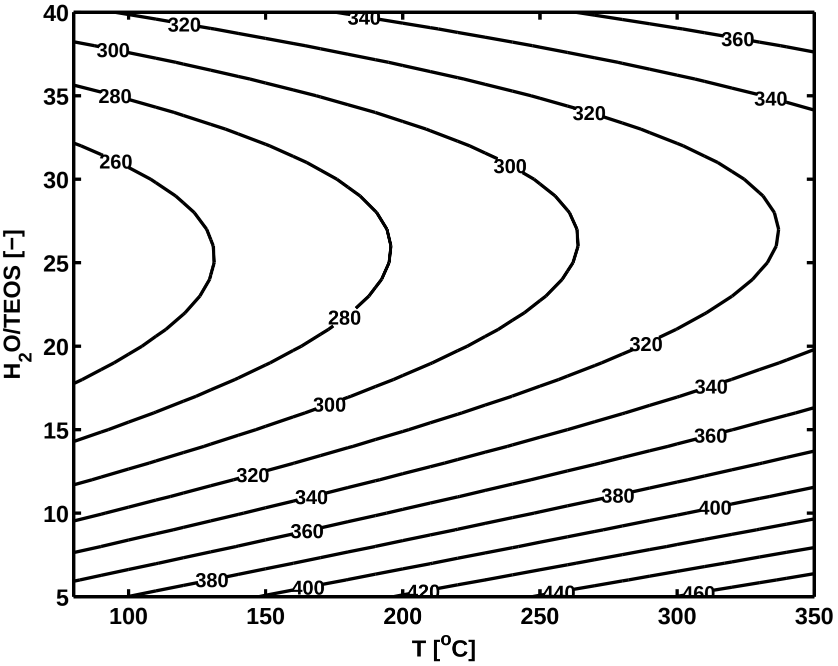

Figure 5.7: Effect of T and H_2O/TEOS on BET surface area at P123/TEOS = 0.0095 and EtOH/TEOS = 25.6

increases from 350 to nearly 450 m^2/g with an increase in P123/TEOS from 0.016 to 0.02. The contours reveal the possibility to achieve the same surface area using distinctly different combinations of P123/TEOS and H_2O/TEOS. For instance, S_{BET} = 350 m^2/g could be achieved

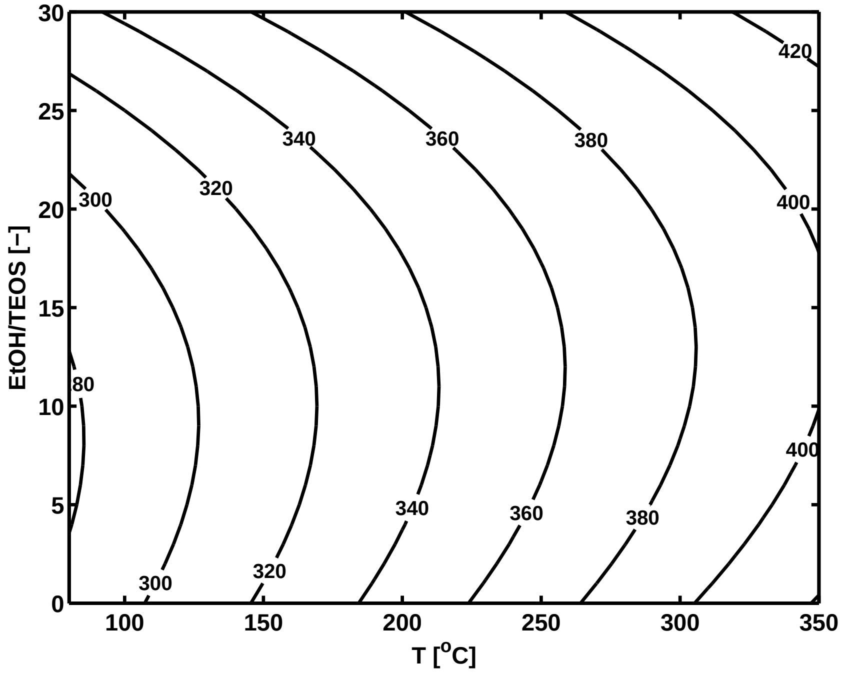

Figure 5.8: Effect of T and EtOH/TEOS on BET surface area at P123/TEOS = 0.0095 and H_2O/TEOS = 10.1

at P123/TEOS = 0.01 and H_2O/TEOS values of both 16 and 37. This surface area could also be achieved at an intermediate value of H_2O/TEOS = 25, by increasing the P123/TEOS ratio close to 0.0163.

From these contour plots, we expect that surface areas in excess of 400 m^2/g could be obtained over the entire range of P123/TEOS, for H_2O/TEOS < 10.

Effect of H_2O /TEOS on surface area

It is observed from Figure 5.5 that, at P123/TEOS = 0.015, S_{BET} decreases with an increase in H_2O/TEOS from 5 to 18, while a marginal increase in S_{BET} for H_2O/TEOS greater than 35 could be predicted. Calculations were carried out using Equation (5.6) and the results are presented in the form of the contours shown in Figure 5.6 and 5.7. It can be inferred from Figure 5.6 that at constant EtOH/TEOS, and from Figure 5.7 that at constant temperature, the surface area is significantly lower with increasing H_2O/TEOS. At an intermediate value of EtOH/TEOS = 15, surface area monotonically decreases from 440 m^2/g to 320 m^2/g, by increasing H_2O/TEOS till 20, beyond which there is a slight rise in surface area. In the range investigated H_2O/TEOS seems to have a predominantly negative influence on the surface area. This was also shown from the statistical analysis, where H_2O/TEOS was determined to be a significant variable with a net negative estimate of its effect on the BET surface area. Water mainly serves as a solvent for dissolving P123 (in addition to EtOH), and the HCl present in the water might be responsible for the effect on the surface area, instead of H_2O itself.

It can be inferred that a lower H_2O/TEOS ratio should be used, irrespective of the EtOH/TEOS ratio, to produce particles with a relatively high BET surface area.

Effect of EtOH/TEOS on surface area

Equation (5.6) is used to study the effect of EtOH/TEOS and T on surface area at constant P123/TEOS = 0.0095 and H_2O/TEOS =10.1. Contours of constant surface area are shown in Figure 5.8 for different combinations of T and EtOH/TEOS.

It is seen from Figure 5.8 that at constant T, and from Figure 5.6 at constant H_2O/TEOS, variation of EtOH/TEOS does not have any significant influence on the surface area. At EtOH/TEOS = 10, one sees an increase in surface area from 280 m^2/g till 400 m^2/g over the entire temperature range. It should be possible to achieve a surface area of 360 m^2/g at low EtOH/TEOS of 5 and T = 250 °C.

From Figure 5.8, it can be inferred that the same surface area could also be obtained at much higher EtOH/TEOS of 25 and with a lower temperature of 200 °C. Additionally, surface areas in excess of 400 m^2/g could be achieved at temperatures higher than 250 °C.

Effect of temperature on surface area

Contour plots are drawn based on Equation (5.6), and are shown in Figure 5.7 and 5.8. The contours of Figure 5.7 reveal that at constant H_2O/TEOS, there is not much variation in BET surface area with temperature, T. At H_2O/TEOS = 25, there is an increase of only 60 m^2/g in spite of increasing the temperature by more than 200 °C. The variation in surface area is less apparent at lower H_2O/TEOS values. At T = 200 °C, an increase in H_2O/TEOS from 5 till 25 leads to a decrease in surface area from 400 m^2/g till 280 m^2/g, and a further increase in H_2O/TEOS only slightly increases the BET area. Surface areas in excess of 400 m^2/g could, however, be achieved for low H_2O/TEOS < 10 and $T > 100$ °C. It is also observed from Figure 5.8 that temperature is less significant compared to the effects of P123/TEOS and H_2O/TEOS, which are more significant than EtOH/TEOS within the studied range.

5.3.3 Effect of experimental parameters on total pore volume (V_t)

A quadratic relation similar in form to Equation (5.3) was used to predict the total pore volume of products:

$$\begin{aligned}V_t = b_0 + b_1x_1 + b_2x_2 + b_3x_3 + b_4x_4 +\\ b_{11}x_1^2 + b_{22}x_2^2 + b_{33}x_3^2 + b_{44}x_4^2 +\\ b_{12}x_1x_2 + b_{13}x_1x_3 + b_{23}x_2x_3 + b_{24}x_2x_4 + b_{34}x_3x_4\end{aligned} \tag{5.7}$$

The regression correlation coefficient, R^2, in this case was 0.934. The estimated coefficients were substituted in Equation (5.7) to obtain:

$$
\begin{aligned}
V_t = {} & 0.239 + 68.39x_1 + 0.00279x_2 + 0.00721x_3 + 0.00302x_4 \\
& - 2567.53x_1^2 - 3.58 \times 10^{-6}x_2^2 - 7.3 \times 10^{-5}x_3^2 - 1.69 \times 10^{-4}x_4^2 \\
& - 0.0279x_1x_2 - 0.237x_1x_3 + 0.499x_1x_4 - 7.43 \times 10^{-6}x_2x_3 \\
& + 1.24 \times 10^{-6}x_2x_4 - 7.61 \times 10^{-5}x_3x_4
\end{aligned} \tag{5.8}
$$

Equation (5.8) was further substituted with x_1 (P123/TEOS) = 0.018 and x_1 (P123/TEOS) = 0.0095 to obtain Equation (5.9) and (5.10) respectively to predict the effect of the experimental parameters on the total pore volume of the synthesized products.

$$
\begin{aligned}
V_t = {} & 0.638 + 0.0023x_2 + 0.0029x_3 + 0.012x_4 \\
& - 3.58 \times 10^{-6}x_2^2 - 7.3 \times 10^{-5}x_3^2 - 1.69 \times 10^{-4}x_4^2 \\
& - 7.43 \times 10^{-6}x_2x_3 + 1.24 \times 10^{-6}x_2x_4 - 7.61 \times 10^{-5}x_3x_4
\end{aligned} \tag{5.9}
$$

$$
\begin{aligned}
V_t = {} & 0.657 + 0.00252x_2 + 4.95 \times 10^{-3}x_3 + 7.76 \times 10^{-3}x_4 \\
& - 3.58 \times 10^{-6}x_2^2 - 7.3 \times 10^{-5}x_3^2 - 1.69 \times 10^{-4}x_4^2 \\
& - 7.43 \times 10^{-6}x_2x_3 + 1.24 \times 10^{-6}x_2x_4 - 7.61 \times 10^{-5}x_3x_4
\end{aligned} \tag{5.10}
$$

Similar to the BET surface area, the trends were represented in the form of contour plots using the Equations (5.9) and (5.10).

Effect of P123/TEOS on pore volume

The most significant variables affecting pore volume, as observed from statistical analysis, are P123/TEOS and T. Hence, calculations were made using Equation (5.8) to estimate various combinations of P123/TEOS and T at a constant pore volume, and the results of these computations are expressed as contours plots, shown in Figure 5.9.

It can be seen from Figure 5.9 that the contours take an elliptical shape. Within the range of the variables studied, the pore volumes from 0.5 cm^3/g till 0.75 cm^3/g can be obtained. No large variations in pore volume with P123/TEOS are observed. At T = 300 °C, it is possible to achieve the same V_t = 0.7 cm^3/g at P123/TEOS = 0.009 and 0.018. Pore volumes as high as 0.75 cm^3/g could, however, be obtained in a narrow range of P123/TEOS lying between 0.0127 and 0.016 and at $T > 275$ °C .

Effect of H_2O /TEOS on pore volume

Equation (5.10) was used to estimate the influence of H_2O/TEOS and T on the total pore volume at fixed P123/TEOS = 0.0095 and EtOH/TEOS = 25.6, and the results of these computations are represented as contours in Figure 5.10.

Again the contours are parts of ellipses. Compared to temperature, H_2O/TEOS has a marginal

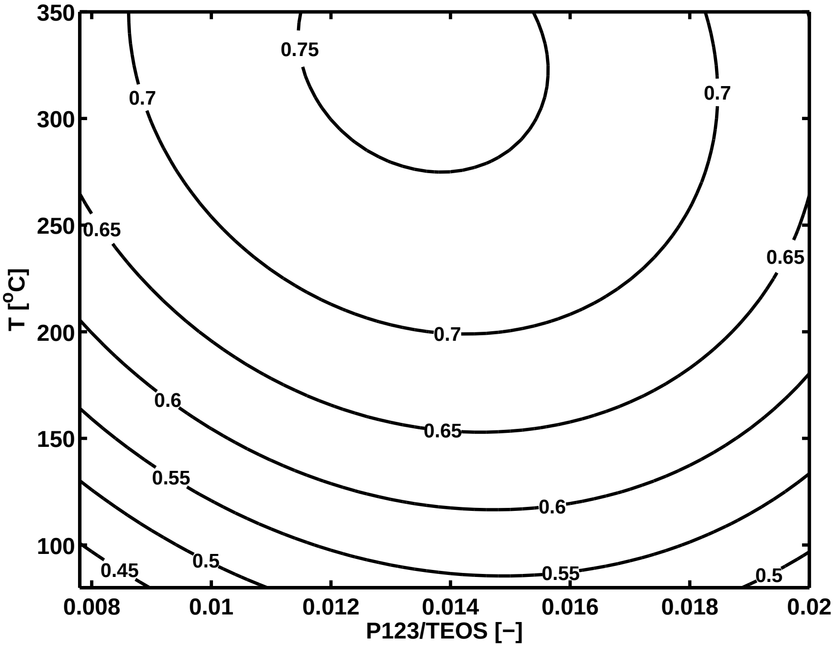

Figure 5.9: Contours of V_t as a function of P123/TEOS and T at H_2O/TEOS = 10.1 and EtOH/TEOS = 25.6

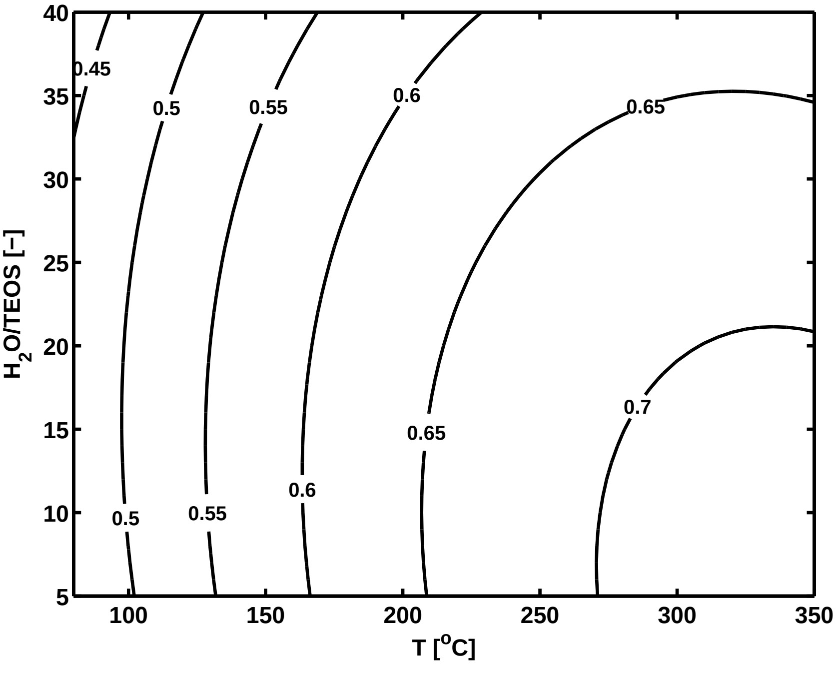

Figure 5.10: Contours of V_t as a function of T and H_2O/TEOS at P123/TEOS = 0.0095 and EtOH/TEOS = 25.6

effect on the pore volume. It is possible to achieve pore volumes of 0.65 cm^3/g at a considerably high temperature of 300 °C and H_2O/TEOS = 35. However, the same pore volume can be obtained at low temperatures close to 200 °C by decreasing the H_2O/TEOS to 15.

This in a way reflects the fact that a lower temperature is sufficient to evaporate droplets with

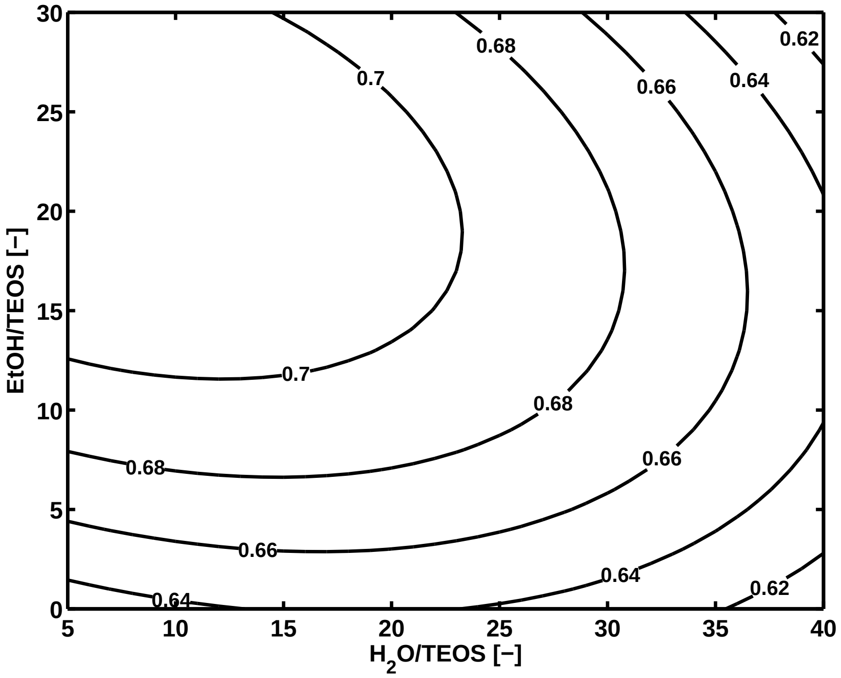

Figure 5.11: Contours of V_t as a function of H_2O/TEOS and EtOH/TEOS at P123/TEOS = 0.0095 and T = 310 °C

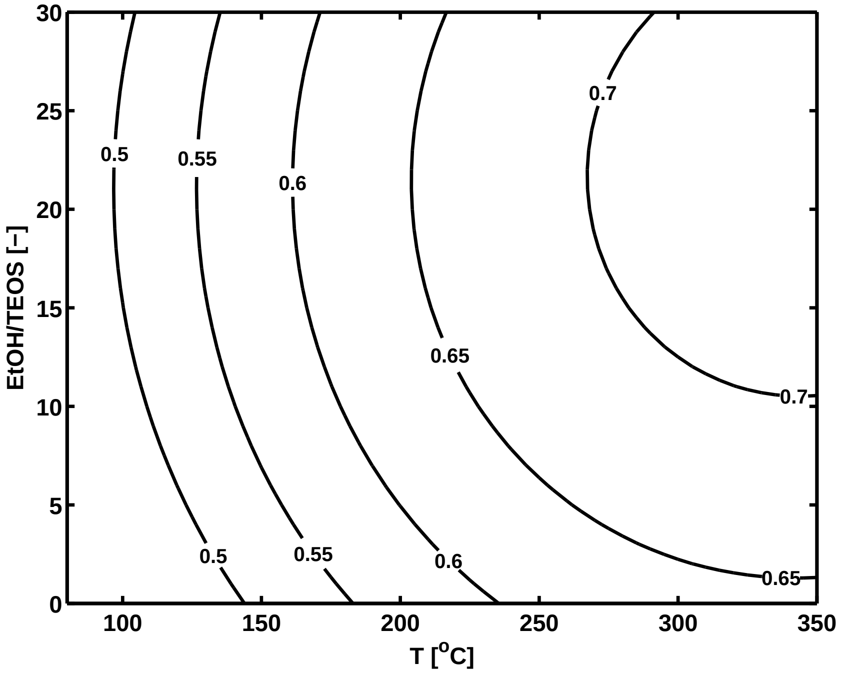

Figure 5.12: Contours of V_t as a function of T and EtOH/TEOS at P123/TEOS = 0.0095 and H_2O/TEOS = 10.1

lower water content. In order to ensure a high pore volume in the final particles, it is recommended to keep a low H_2O/TEOS ratio.

Table 5.6: Prediction of total pore volume and BET surface area

P123/TEOS, x_1 [-]	T, x_2 [^oC]	H_2O/TEOS, x_3 [-]	EtOH/TEOS, x_4 [-]	S_{BET} [m^2/g] Exp.	S_{BET} [m^2/g] Pred.	V_t [cm^3/g] Exp.	V_t [cm^3/g] Pred.
0.01375	350	22.5	15	305	311	0.71	0.70
0.01375	215	40	15	313	340	0.62	0.61
0.01375	215	22.5	0	298	292	0.59	0.58

Effect of EtOH/TEOS on pore volume

The contours shown in Figure 5.11 represent the effect of variations of $\mathrm{H_2O}$/TEOS and EtOH/TEOS on the total pore volume at fixed conditions of P123/TEOS = 0.0095 and temperature, T = 310 °C, on the basis of Equation (5.10). Figure 5.11 indicates that there is no significant effect of EtOH/TEOS and $\mathrm{H_2O}$/TEOS on the pore volume at these conditions. We also observe that at EtOH/TEOS = 20, the total pore volume decreases from 0.70 cm^3/g to 0.62 cm^3/g with increase in $\mathrm{H_2O}$/TEOS. On the other hand, at low $\mathrm{H_2O}$/TEOS=10, increasing EtOH/TEOS results in an increase in pore volume till 0.70 cm^3/g.

Effect of temperature (*T*) on pore volume

Figure 5.9 indicates that, in general, for a constant P123/TEOS, V_t increases with increased T. It is also possible to achieve a pore volume close to 0.7 cm^3/g at a lower temperature of 200 °C for P123/TEOS = 0.014. At much lower temperatures, for $T < 150$ °C, one could synthesize particles with pore volumes close to 0.6 cm^3/g for P123/TEOS $>$ 0.01.

It is observed from Figure 5.9 that the temperature could be used to control the pore volume more significantly. This is in agreement with the statistical analysis, which identified temperature to have the most significant positive effect on the pore volume.

Equation (5.10) was used to generate contours (shown in Figure 5.12) at P123/TEOS = 0.0095 and $\mathrm{H_2O}$/TEOS = 10.1 to illustrate the variation of pore volume simultaneously with temperature, T, and EtOH/TEOS. The contours are elliptical. At EtOH/TEOS = 15, V_t increases from 0.50 till 0.70 cm^3/g when increasing T from 100 till 280 °C. It is possible to achieve the same pore volume using different combinations of EtOH/TEOS and T. It is evident from Figure 5.12 that temperature has a much more pronounced effect on the pore volume as compared to EtOH/TEOS. Here again, at these conditions, in order to achieve a high pore volume of around 0.7 cm^3/g, it is essential to use a high temperature, though this could be achieved at a low EtOH/TEOS of around 10.

The correlations relating the BET surface area and the total pore volume with the experimental parameters (Equations (5.4) and (5.8), respectively) are tested by comparing the predictions using additional experimental datapoints. The results of the predictions are given in Table 5.6. It is clearly seen that there is not much deviation between the experimental and the predicted values, hence the conclusion that the correlations can be used to predict the properties of the materials (S_{BET} and V_t) within the range of experimental conditions studied.

5.3.4 Nitrogen adsorption/desorption isotherms and pore size distributions

The nitrogen adsorption/desorption isotherms were obtained for all calcined products. The corresponding pore size distribution was obtained by applying the BJH model to the adsorption branch of the isotherm. It was observed by comparing all the conditions that the P123/TEOS ratio had the most significant effect on the shape of the isotherm.

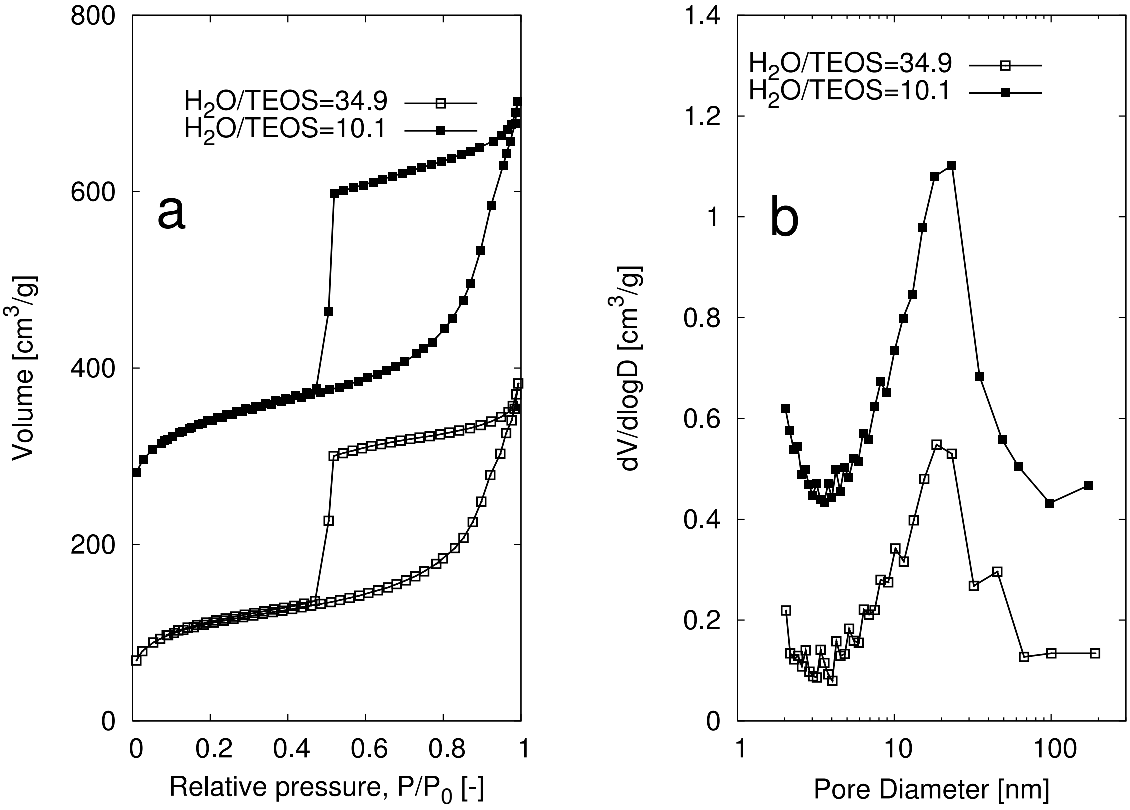

Figure 5.13: (a) Nitrogen adsorption/desorption isotherms, and (b) pore size distribution, based on the adsorption isotherm, of products obtained at constant conditions of P123/TEOS = 0.018, T = 310 °C, EtOH/TEOS = 25.6 (isotherms and pore size distribution corresponding to H_2O/TEOS = 10.1 are offset by 200 cm^3/g and 0.3 cm^3/g respectively for clarity)

Figure 5.13 shows typical adsorption/desorption isotherms and the pore size distribution of products obtained for a high P123/TEOS ratio of 0.018. We observe that the isotherms are type IV with H1 hysteresis [28], and there is a gradual uptake of nitrogen at high relative pressures, indicating a non-uniform pore distribution. This is confirmed by the relatively broad pore size distribution (Figure 5.13b) centered at a large pore size of around 20 nm. Furthermore, we also see that nitrogen gradually desorbs from a relative pressure close to 1.0, while, around P/P_o = 0.5, there is a sharp, rapid desorption, beyond which the desorption branch coincides with the adsorption branch. This suggests the presence of ink-bottle pores, with narrow entrances leading to much broader pores.

At high P123/TEOS ratio, the non-uniformity of the pore system implies that there is no ordered arrangement of pores. This is clearly seen from the absence of sharp diffraction peaks in the

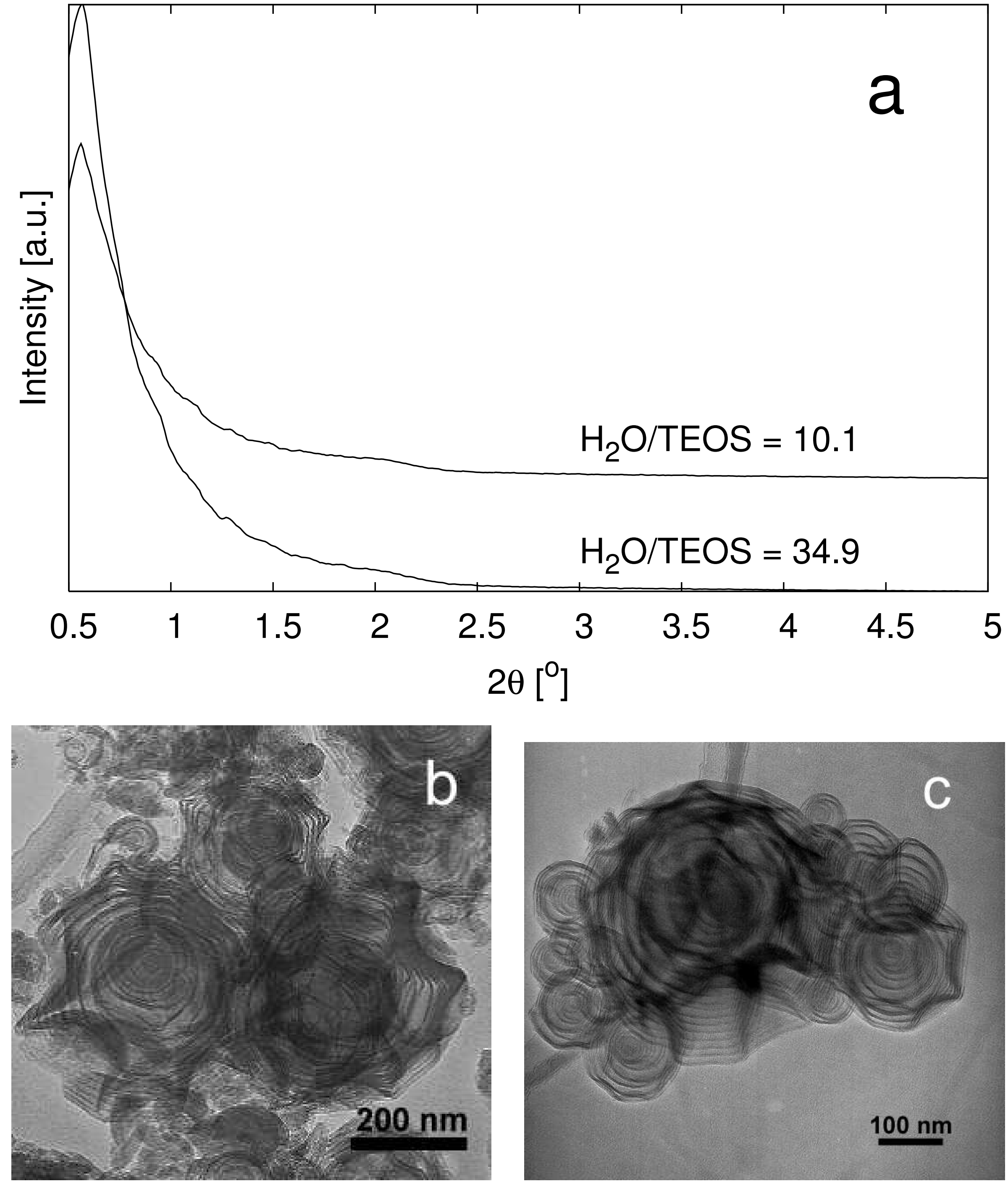

Figure 5.14: (a) X-ray diffraction patterns, (b) and (c) TEM images of calcined products synthesized with P123/TEOS = 0.018, T = 310 °C, EtOH/TEOS = 25.6 and H_2O/TEOS = (b) 34.9, and (c) 10.1

XRD patterns of the calcined samples shown in Figure 5.14 a. The peaks appearing close to $2\theta = 0.5^\circ$ are artificial, as a result of scattering of the X-rays at the beam stop of the diffractometer, corresponding to the detection limit of the instrument.

High-resolution transmission electron micrographs of the particles shown in Figure 5.14 b and c give further insight into the pore structure. We can see that particles synthesized at different H_2O/TEOS ratios of 10.1 and 34.9 show a similar pore structure. The particles contain lamella with a non-uniform layer-to-layer distance.

The spacing between these layers composed of microporous silica corresponds to the non-uniform pore distribution seen from the N_2 adsorption measurements. In some particles, we also see a spiral layer extending near the surface, and then retracting to a few layers inside, taking a form akin to the petals of a flower. These layered structures seem to occur as a result of scaffolding of the surfactant molecules. A high P123/TEOS ratio favors aggregation of the block copolymer micelles, forming layers, and silica condenses around them to form a lamellar pore network.

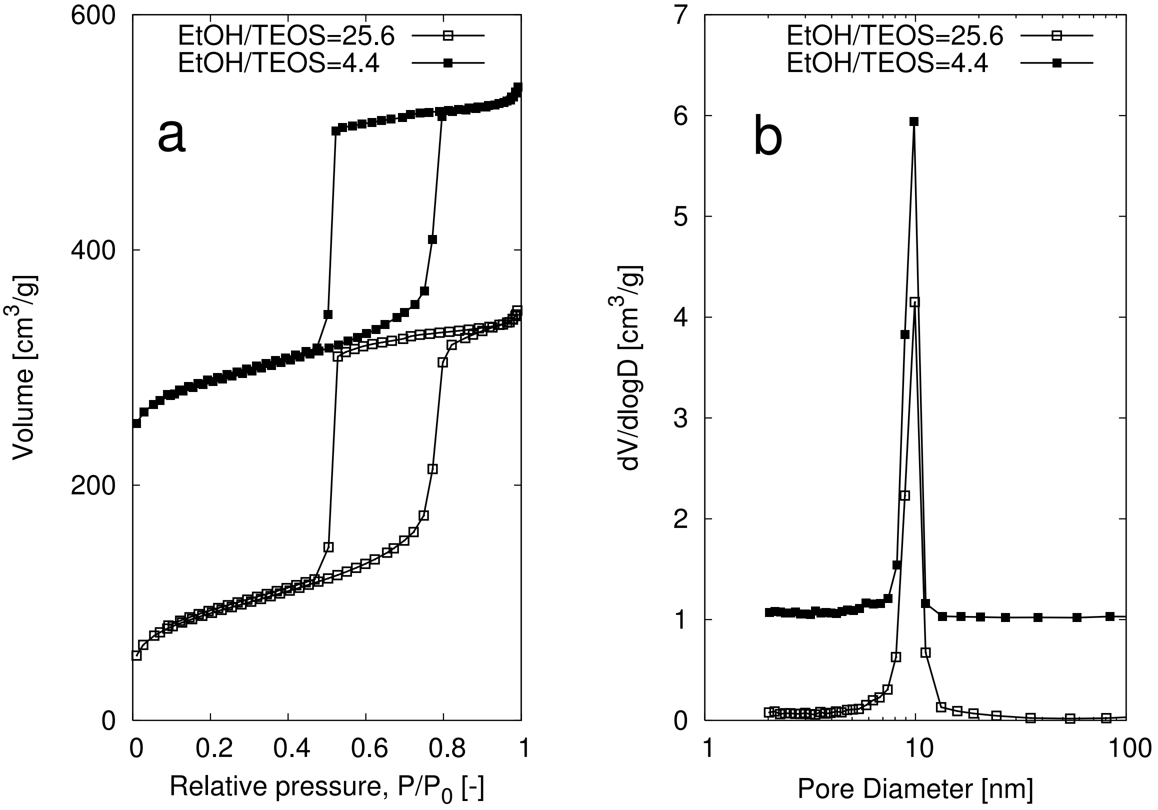

Figure 5.15: (a) Nitrogen adsorption/desorption isotherms, and (b) pore size distribution, based on the adsorption isotherm, of products obtained at constant conditions of P123/TEOS = 0.0095, T = 120 °C, H_2O/TEOS = 10.1 (isotherms and pore size distribution corresponding to EtOH/TEOS = 4.4 are offset by 200 cm^3/g and 1.0 cm^3/g respectively for clarity)

Figure 5.15 a and b show the nitrogen adsorption/desorption isotherms, and the pore size distributions of calcined silica particles synthesized using a comparably lower P123/TEOS = 0.0095. Here, we also observe a typical type IV isotherm with type H1 hysteresis loop, though marked by a sharp uptake in nitrogen at a higher relative pressure indicating a uniform pore size. By applying the BJH model to the adsorption branch of the isotherm, we obtain a pore size distribution centered around 10 nm. It must be noted that that experiments performed at all other conditions of T, H_2O/TEOS and EtOH/TEOS resulted in similar isotherms and pore size dis-

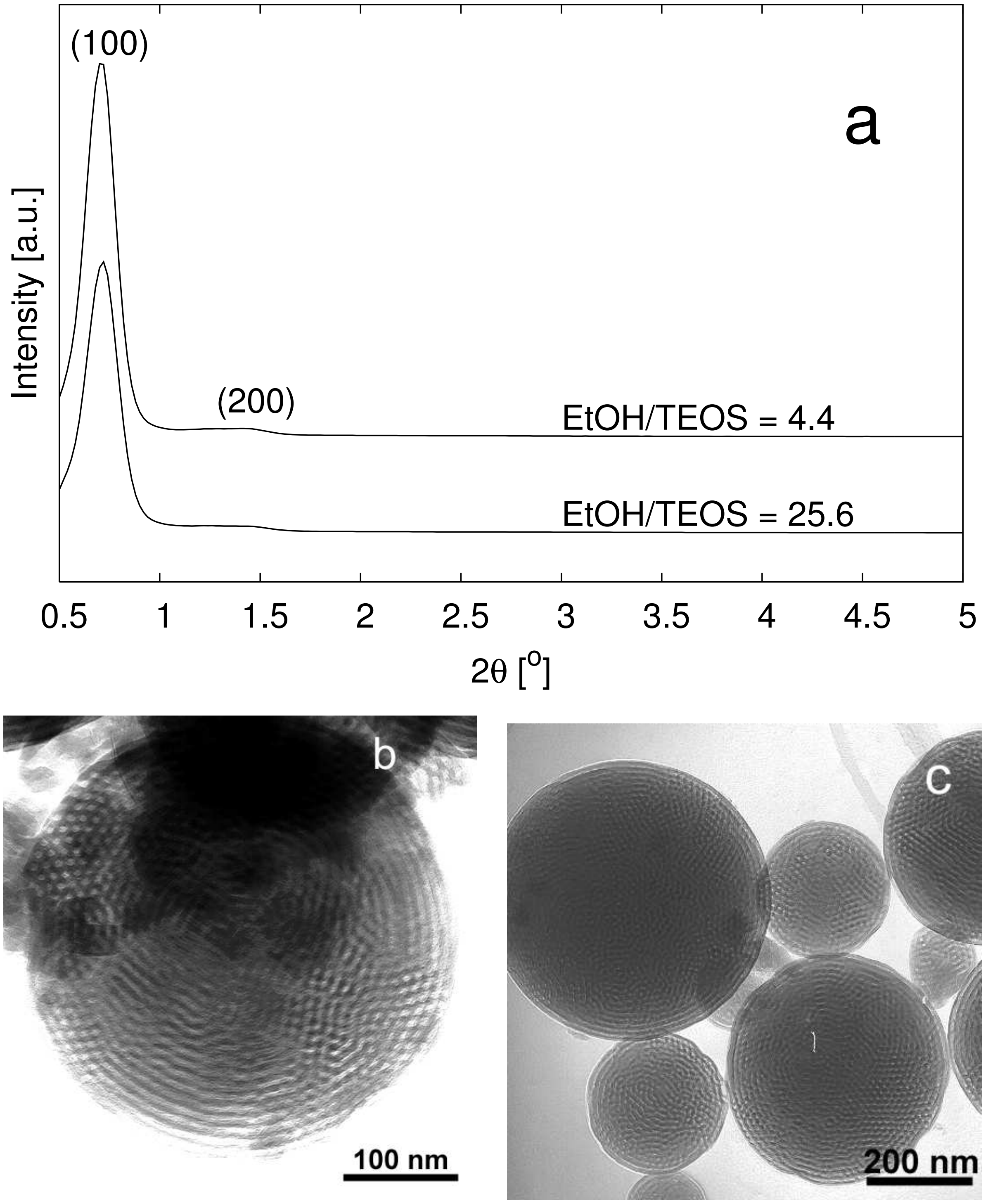

Figure 5.16: (a) X-ray diffraction patterns, (b) and (c) TEM images of calcined products synthesized with P123/TEOS = 0.0095, T = 120 °C, H_2O/TEOS =10.1 and EtOH/TEOS = (b) 25.6, and (c) 4.4

tribution. The only exception was observed for T = 120 °C, H_2O/TEOS = 34.9, EtOH/TEOS = 25.6, which resulted in a slightly wider pore size of 11 nm. We also observe that nitrogen desorbs at a relative pressure close to 0.5, which suggests the presence of an ink-bottle pore structure, with small pores forming the entrance to the inner porosity consisting of uniformly sized large pores.

X-ray diffraction patterns of these particles are shown in Figure 5.16 a. They exhibit a sharp, intense diffraction peak indexed to the (100) plane, followed by a weak (200) reflection, while the (110) peak is absent. The presence of the (100) peak is indicative of good structural order consistent with the presence of a uniform pore structure. The weak higher order reflections refer to the absence of long-range order.

The TEM images (Figure 5.16 b, c) of these particles reveal their internal pore structure. We see a rather complex pore arrangement within each particle. The pores are arranged in a hexagonal manner in certain regions, while in other regions the pores tend to align in layers parallel to the surface of the spherical particles. The latter is most clearly seen near the particle surface. This surface phenomenon is forcibly induced due to the spherical morphology originating from the droplet, and is retained throughout the evaporation process.

5.4 Conclusions

The application of factorial design has been demonstrated to effectively identify the significant variables and interaction between the variables. Using appropriate statistical techniques, it is possible to estimate the order of significance of the variables, and to indicate the positive and negative effects on both surface area and pore volume.

In the evaporation induced self-assembly of silica particles, the variables P123/TEOS and $\mathrm{H_2O}$/TEOS had the most significant effect on the BET surface area of the produced particles. Due to a significant interaction between P123/TEOS and EtOH/TEOS the effect of these variables on the surface area should be considered jointly. The variables T and EtOH/TEOS had the most effect on the total pore volume of the particles. We also observed an interaction between P123/TEOS and EtOH/TEOS, which cautions us against studying effects of these variables independently. A regression analysis was carried out to relate the experimental parameters with the BET surface area and pore volume of the products. The results were represented as contours that allowed quantification of the effects of different operating conditions.

In the field of materials science, it is often encountered that the synthesis involves fine-tuning several experimental variables in order to achieve a desired product. This is usually done by extensive trial and error. An appropriate, statistically aided experimental design could easily avoid such a scenario. By using the techniques described in this paper one can identify and narrow down to the variables, or combinations of variables, that have a significant effect on the property of the material under scrutiny, and this with a minimum of experimental runs. This information could be used as a basis for additional experiments to improve the quality of the material by fine-tuning these significant variables. In addition, the empirical facts derived can serve as a basis of understanding and modeling of a complex process.

References

1. H. Fan, F. Van Swol, Y. Lu, C. J. Brinker, J. Non-Crys. Solids 285 (2001) 71.
2. M. T. Bore, S. B. Rathod, T. L. Ward, A. B. Datye, Langmuir 19 (2003) 256.
3. A. Vinu, T. Mori, K. Ariga, Sci. Technol. Adv. Mater. 7 (2006) 753.
4. C. T. Kresge, M. E. Leonowicz, W. J. Roth, J. C. Vartuli, J. S. Beck, Nature 359 (1992) 710.
5. D. Zhao, J. Feng, Q. Huo, N. Melosh, G. H. Fredrickson, B. F. Chmleka, G. D. Stucky, Science 279 (1998) 548.
6. R. Pitchumani, W. Li, M.-O. Coppens, Catalysis Today 105 (2005) 618.
7. Y. Lu, H. Fan, A. Stump, T. L. Ward, T. Rieker, C. J. Brinker, Nature 398 (1999) 223.
8. N. Baccile, D. Grosso, C. Sanchez, J. Mater. Chem. 13 (2003) 3011.
9. J. E. Hampsey, S. Arsenault, Q. Hu, Y. Lu, Chem. Mater. 17 (2005) 2475.
10. S. Areva, C. Boissire, D. Grosso, T. Asakawa, C. Sanchez, M. Lindn, Chem. Comm. (2004) 1630.
11. M. T. Bore, R. F. Marzke, T. L. Ward, A. K. Datye, J. Mater. Chem. 15 (2005) 5022.
12. M. T. Bore, H. N. Pham, T. L. Ward, A. K. Datye, Chem. Comm. (2004) 2620.
13. Y. Lu, B. F. McCaughey, D. Wang, J. E. Hampsey, N. Doke, Z. Yang, C. J. Brinker, Adv. Mater. 15 (2003) 1733.
14. M. T. Bore, T. L. Ward, A. Fukuoka, A. K. Datye, Catalysis Letters 98 (2004) 164.
15. D. Zhao, P. Yang, N. Melosh, J. Feng, B. F. Chmelka, G. D. Stucky, Adv. Mater. 10 (1998) 1380.
16. Z. Knya, J. Zhu, A. Szegedi, I. Kiricsi, P. Alivisatosa, G. A. Somorjai, Chem. Comm. (2003) 314.
17. P. S.-Winkel, P.Yang, D. I. Margolese, B. F. Chmelka, G. D. Stucky, Adv. Mater. 11 (1999) 303.
18. He Zhang, J. Sun, D. Ma, X. Bao, A. K-Hoffmann, G. Weinberg, D. Su, R. Schlg, J. Am. Chem. Soc. 126 (2004) 7440.
19. X. Y. Bao, X. S. Zhao, J. Phys. Chem. B 109 (2005) 10727.
20. D. Zhao, Q. Huo, J. Feng, B. F. Chmelka, G. D. Stucky, J. Am. Chem. Soc. 120 (1998) 6024.
21. P. Shah, A. V. Ramaswamy, K. Lazarc, V. Ramaswamy, Applied Catalysis A: General 273 (2004) 239.
22. G. E. Box, W. G. Hunter, J. S. Hunter, Statistics for experimenters, John Wiley & Sons, New York (1978).
23. O. L. Davies, The design and analysis of industrial experiments, Oliver & Boyd, London (1954).
24. M. Tagliabue, L.C. Carluccio, D. Ghisletti, C. Perego, Catalysis Today 81 (2003) 405.
25. F. N. Serralha, J.M. Lopes, F. Lemos, F. R. Ribeiro, D. M. F. Prazeres, M. R. Aires-Barros, J.M.S. Cabral, J. Mol. Catalysis B: Enzymatic 27 (2004) 405.
26. G. E. P. Box, R. B. Wilson, J. Roy Statistical Soc. (B) 13 (1954) 1.
27. C. Daniel, Applications of statistics to industrial experimentation, Wiley, New York (1976).
28. M. Kruk, M. Jaroniec, Chem. Mater., 13 (2001) 3169.

Chapter 6

Continuous Synthesis by Spray Drying of Remarkably Stable Mesoporous Silica and Silica-Alumina Catalysts using Industrial Raw Materials

6.1 Introduction

Mesoporous alumino-silicates with high surface areas, pore volumes and well-defined pore networks have attracted much attention, especially in the field of separation and catalysis of large molecules, due to the improved accessibility of the acid sites [1]. Of the class of mesoporous materials, SBA-15, synthesized using a non-ionic surfactant, P123 ($EO_{20}PO_{70}EO_{20}$) under strongly acidic conditions, possesses a broader pore size and thicker pore walls as compared to M41S [2], making them more hydrothermally stable.

We were recently able to synthesize SBA-15 with a tunable morphology - free standing films, fibers, bundles and cakes - by simply controlling the stirring rate. Furthermore, these mesoporous materials were synthesized using a weak acid, H_3PO_4, which also provides additional acid sites in the form of P-O-Si bonds [3]. However, in the laboratory these mesoporous materials are usually synthesized in batch using the well-known sol-gel technique, which takes days to obtain the final product. A novel technique termed “evaporation-induced self-assembly” (EISA) of aerosols [4-6] provides an alternative to continuously synthesize mesoporous silica particles by spraying droplets of the precursor solution through a tubular oven. The process involves the synthesis of mesoporous silica using TEOS as a silica source and different ionic or non-ionic structure-directing agents as templates to induce porosity. The equipment used in this work could be used to produce material amounts in the range of mg/h, however, the delicate nature of the equipment, using a single spraying nozzle, doesn’t necessarily allow a direct step-up to

---

This chapter is based on the following publication:
R. Pitchumani, J. J. Heiszwolf, A. Schmidt-Ott, M.-O. Coppens, Adv. Func. Mater. (2008) *(submitted)*

the industrial production scale.

Furthermore, the key drawback in scaling up most academic work on the synthesis of mesoporous silicas is the use of silicon alkoxides, *e.g.*, tetraethyl orthosilicate (TEOS), as the silica source. First, TEOS is an expensive raw material that prevents cost-effective, large-scale production of the mesoporous materials to replace industrially manufactured catalytic materials like zeolites. Second, during synthesis, the silicon alkoxide hydrolyzes into silicic acid and an alcohol. For example, ethanol released during the hydrolysis of TEOS, is a flammable material that has a wide explosion range in air (3 - 20 %). This means that in an industrial environment, special precautions are needed to prevent unsafe situations. It must be emphasized that spray drying, in which the liquid is evaporated into a large drying chamber, is especially hazardous if flammables are present. In general, catalyst manufacturing plants are designed to process inorganic aqueous mixtures, and are not suited to handle flammable materials. Because of the above considerations, scale-up of TEOS-containing recipes to industrial-scale quantities is far from trivial.

Zeolite-Y, or ultra stabilized Y-zeolite (USY), is the main active component of FCC catalysts. However, due to the small pore size of the zeolite crystal, the cracking of large molecules [7] is hindered by diffusion limitations. Kortunov *et al.* [8] have carried out pulse field gradient NMR measurement of n-octane in both USY crystals and spray dried FCC catalyst particles. They have shown that the diffusivity inside the microporous USY crystals is substantially lower than that of the FCC matrix material which includes meso- and macropores.

As a result, the use of mesoporous zeolite-like material may improve the activity of FCC catalysts by facilitating the transport of bulky molecules of heavy feeds. In this paper we present the synthesis of mesoporous silica/alumina materials having Si/Al ratios corresponding to ZSM-5 and Y-zeolite.

Literature often reports that mesoporous silicas or Al-mesoporous silica (by post-grafting Al onto mesoporous silica) are unattractive due to the amorphous nature of the silica walls leading to low hydrothermal stability and activity. This has led to a shift in focus towards synthesis of mesoporous aluminosilicates by assembling zeolite seeds with non-ionic or cationic surfactants (for a review, see [9]). We show that amorphous silica-aluminas are worthy of being reconsidered. In the present paper, we use a commercial bench scale spray drier (Büchi B-290), which is commonly used in industry. Scale-up from this bench scale unit to spray driers of industrial scale is well established in the catalyst and ceramic industry. Using the Büchi equipment, we have been able to synthesize amorphous silica-aluminas that are remarkably stable in a hot steam environment (quantified by retention of pore volume and BET surface area) and also show considerable activity in pulse probe molecule experiments.

Recently, Pang and Tang [10] and Morales *et al.* [11] have prepared mesoporous materials using sodium silicate, which is a cheap raw material widely used on an industrial scale. A drawback of the use of sodium silicate is that sodium remains present in the synthesized materials. Sodium reduces the acidity of the material and adversely affects its steam stability. Removal of sodium requires an ion exchange and washing unit operation, which will result in increased manufacturing costs.

In the present work, we use stabilized silica sol as the silica source. Although stabilized silica sol is somewhat more expensive than sodium silicate, it has the key advantage that the sodium content is typically low, thus eliminating the need for an extra unit operation. Therefore, it is also used by catalyst manufacturers. After the EISA synthesis, the catalyst may be used as such. Using a triblock co-polymer (P123) as the structure-directing agent, we have been able to assemble solutions of colloidal silica, and of colloidal silica plus peptized Catapal particles (Al_2O_3) into mesoporous silica and silica-aluminas. The spray drying process allows continuous production of these mesoporous materials, which are found to be structurally stable under severe steaming conditions. Furthermore, pulse probe molecule experiments conducted using TiPB (tri-isopropyl benzene) and linear alkanes showed reasonable activity.

6.2 Experimental

6.2.1 Materials used

Nano-sized boehmite material Catapal B (68.4 wt% Al_2O_3, 0.002 wt% Na_2O, remainder is bounded H_2O, surface area 250 m^2/g, crystal size 4.5 nm) from Sasol was used as alumina source. Stabilized colloidal silica (30 wt% SiO_2, 0.6 wt% Na_2O, surface area 190 m^2/g, particle size 16 nm) was used as silica source. P123 (Sigma Aldrich, $EO_{20}PO_{70}EO_{20}$, molar mass 5800 g/mol) was used as the structure-directing agent.

6.2.2 Solution preparation

A typical synthesis involving the system composed of silica, alumina and P123 ($EO_{20}PO_{70}EO_{20}$) is described. A 10 wt% solution of P123 in deionized water was used in the experiments involving the template. Catapal (68.4 wt% Al_2O_3) was peptised to a pH around 2 using HNO_3 in water. Calculated amounts of colloidal silica were added to the P123 solution, and stirred at room temperature to get a metastable solution. The peptised Catapal solution was subsequently added and stirred well to get a homogeneous precursor. These solutions were then sprayed using the Büchi spray drier.

Different solutions were prepared composed of silica sol+P123 and silica sol + P123 + Catapal. Three different loadings of P123 and two different $SiO_2 : Al_2O_3$ (7, 23.4) were used. The solid concentration for the silica sol + P123 + Catapal system was maintained at 10 wt% while the silica sol+P123 system varied from 17.5-25 wt%.

6.2.3 Büchi spray drier operation

The precursor suspension, prepared using the above procedure, was continuously stirred and fed to the spray drier with a peristaltic pump at a feed flow rate of 160 g/min. The liquid was atomized in a two-fluid nozzle using a secondary airflow of 2.5 Nm^3/hr. The liquid spray was fed into a pre-heated primary airflow of 44 Nm^3/hr. The temperature of the spray drier exit gas flow was maintained at 115 °C by controlling the temperature of the gas inlet temperature. Prior to introduction of the silica / alumina suspensions, the spray drier was started up using DI water, and the unit was allowed to reach a steady state by running for 20 minutes on the water feed. Figure 6.1 shows a schematic diagram of the Büchi spray drier type B-290 along with the actual equipment used. The operating conditions are summarized in Table 6.1. After collection

Table 6.1: Operating conditions of the Büchi spray drier

Secondary airflow [Nm^3/h]	2.5
Total airflow [Nm^3/h]	44
Spray drier gas exit temperature setpoint [°C]	115
Peristaltic pump liquid flow rate [g/h] (calibrated for H_2O)	160

of the material from the cyclone of the spray drier, the materials were calcined at 425 °C using a heating rate of 1 °C/min for 3 h to remove the P123 template.

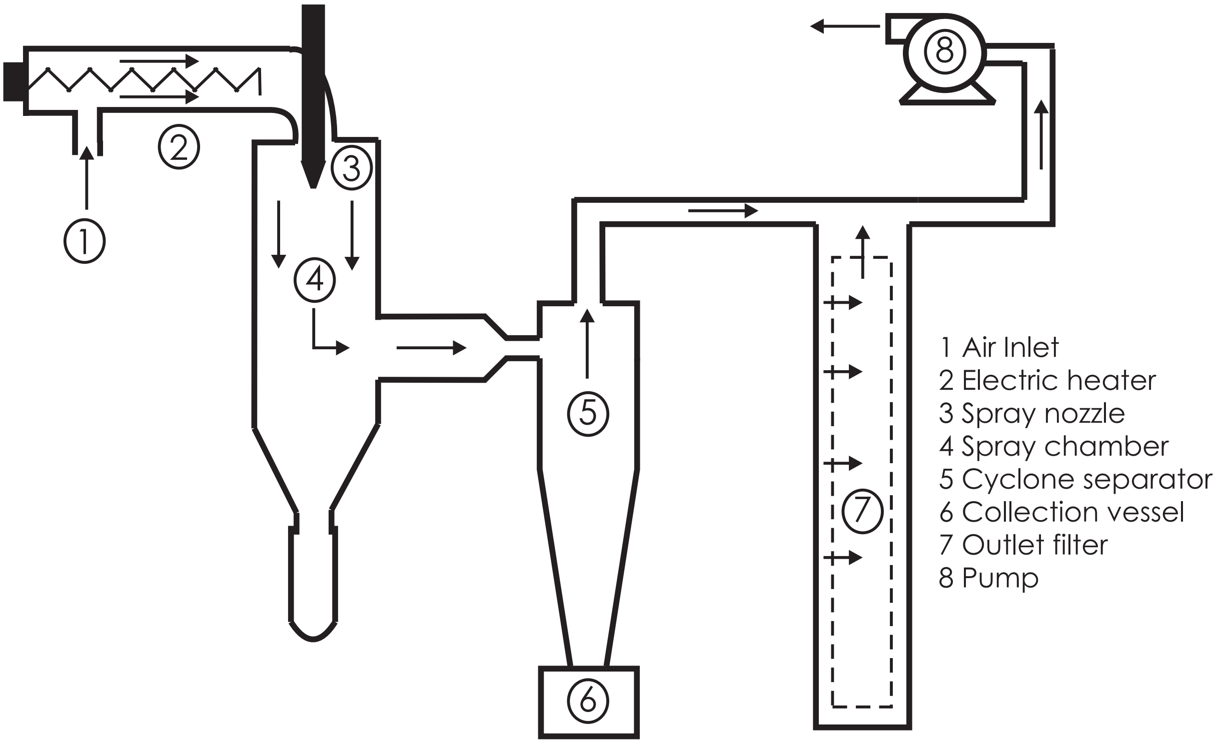

Figure 6.1: Schematic diagram of the Büchi spray drier

6.2.4 Material characterization

N_2 adsorption/desorption isotherms were obtained on a Micromeritics ASAP 2400 at 77 K. Samples were degassed under vacuum at 300 °C overnight prior to the measurements. The pore size distribution was determined by applying the model of Broekhoff and de Boer [12] to the adsorption branch of the isotherm.

6.2.5 Steam stability tests

About 30 mg of the spray-dried and subsequently calcined sample was put into a small quartz cup, which was placed on a tray inside a large quartz tube. Under nitrogen flow, the quartz tube was heated to 788 °C with a heating rate of 5 °C/min. After reaching the set point temperature, the nitrogen flow was switched off and steam from a steam generator was fed to the quartz tube at a rate of 0.5 g/h. The samples were kept in 100 % steam atmosphere for 20 hours followed by cooling down under nitrogen. The steamed samples were analyzed using nitrogen adsorption for surface area, pore volume and pore size distribution.

6.2.6 Probe molecule pulse tests

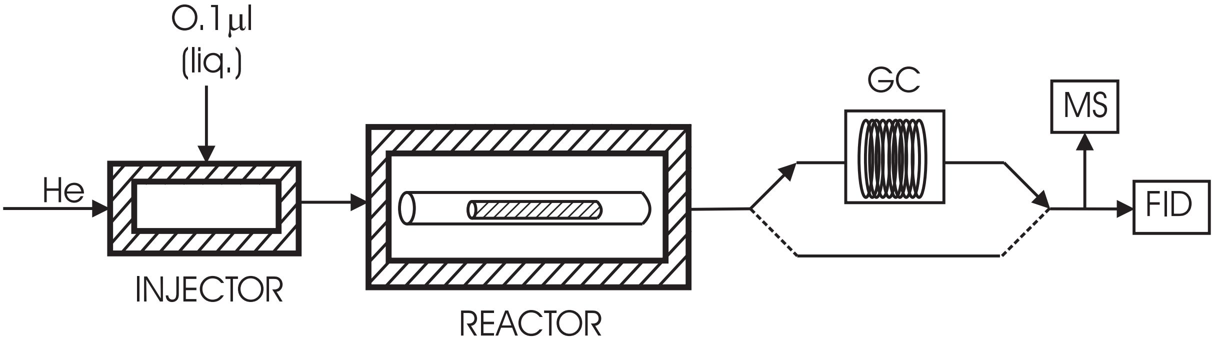

Figure 6.2: Schematic diagram of pulse test equipment

The reactor consists of a quartz tube, with an internal diameter of 2 mm, packed with 20 mg of the steamed material in between two wads of quartz wool. The reactor was placed inside a programmable furnace. On the inlet side, the reactor was connected to an automated GC injection port that can inject a pulse of liquid material into a helium carrier gas flow. The outlet of the reactor may be connected directly, or via a GC column, to a flame ionization detector (FID). In the former configuration the equipment serves as a pulse-response apparatus; in the latter configuration the individual reaction products in the gas stream may be identified. Optionally, the gas stream may be analyzed by a mass spectrometer. The equipment is schematically shown in Figure 6.2.

After installation of the loaded reactor tube into the equipment, the material was conditioned by increasing the temperature to 600 °C at a rate of 5 °C/min under a helium flow of 10 ml/min. After the conditioning step, the reactor tube was brought to the required operating temperature. In the reaction experiments, a pulse of 0.1 µl of liquid reactant was injected into the helium carrier gas flow. For the reactivity of TiPB, reactor temperatures of 400 and 500 °C were used; for $C_{12}H_{26}$ and $C_{14}H_{30}$ a reactor temperature of 600 °C was used. The products were analyzed by GC-FID, and the conversion was calculated from the decrease in GC peak area of the probe molecule fed to the reactor. By conducting a series of sequential pulse experiments, the deactivation of the catalyst may be measured.

6.3 Results and Discussion

6.3.1 Mesoporous silica

For these experiments, calculated amounts of 10 wt% P123 solution and colloidal silica were mixed together to obtain the precursor for the spray dried silica. Figure 6.3 shows the nitrogen adsorption isotherms and pore size distribution of mesoporous silica produced with different P123 content/loading. The N_2 adsorption/desorption isotherms show a typical type IV hysteresis with a type H1 loop. Table 6.2 lists the textural properties of the mesoporous silica synthesized. We can observe that the pore size increases from 10.8 nm till 23.0 nm as we decrease $\mathrm{SiO_2}$: P123 (wt./wt.) from 4.0 to 1.33. Furthermore, there exists a relatively narrow pore size distribution for $\mathrm{SiO_2}$: P123 = 2 or 4, as compared to a more broader pore size network that is obtained using $\mathrm{SiO_2}$: P123 =1.33. This can be explained by the fact that there exists an optimum amount of P123 that could be accommodated within the close packing of silica spheres, the ensemble that determines the final pore structure. The BET surface area of the materials remains constant around 190 m^2/g, while the total pore volume increases from 0.35 till 0.68 cm^3/g with an increase in P123 content (or a decrease in $\mathrm{SiO_2}$: P123 ratio).

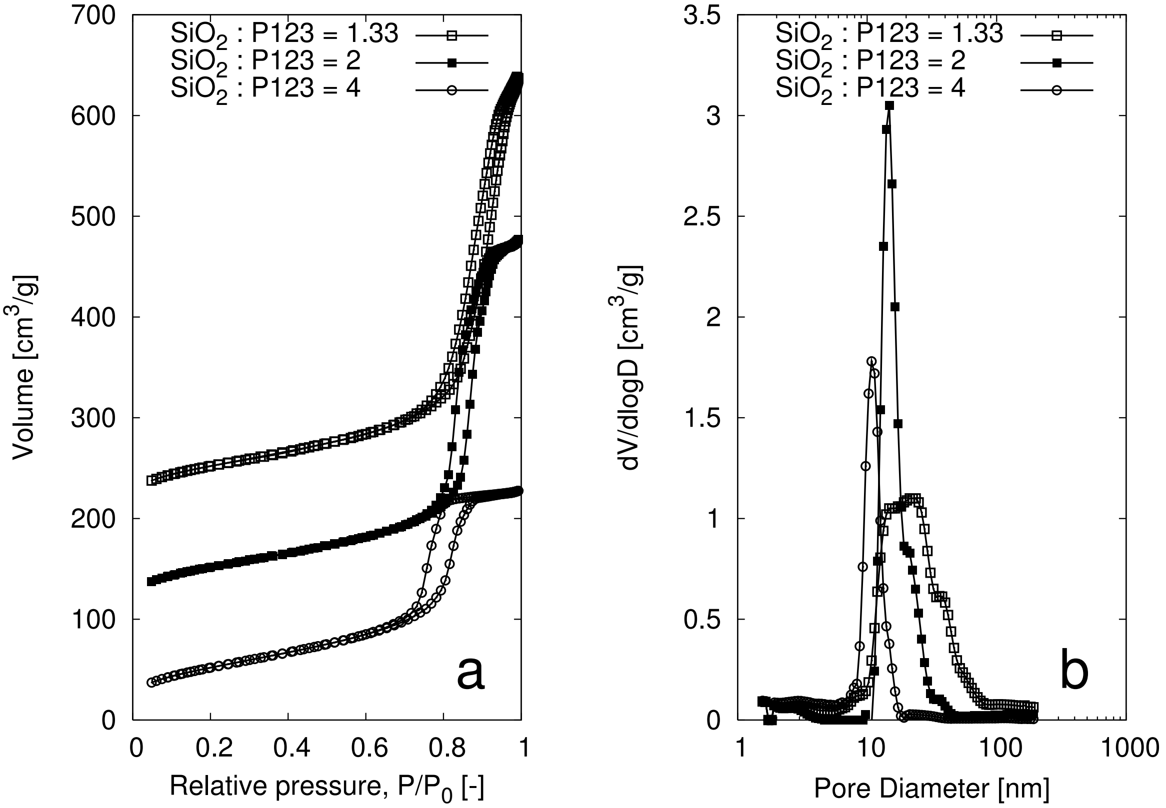

Figure 6.3: (a) N_2 adsorption/desorption isotherms and (b) pore size distribution based on the adsorption branch (model of Broekhoff and de Boer) of mesoporous SiO_2 for different SiO_2 : P123 ratios. Isotherms corresponding to SiO_2 : P123 = 1.33 and 2 have been offset by 200 and 100 cm^3/g respectively for clarity

Table 6.2 also shows the properties of spray-dried silica sol without the structure-directing template. In a structure consisting of packed particles, the pore volume (V_t) can be calculated from:

$$V_t = \frac{\varepsilon_v}{(1-\varepsilon_v)} \frac{1}{\rho_s} \tag{6.1}$$

For silica, we may use a skeletal density of ρ_s = 2.196 g/cm^3, while for the close cubic packing of spheres, a void fraction $\varepsilon_v = 1 - \pi/\sqrt{18} \approx 0.26$ is valid. Substituting these values into

Table 6.2: Textural properties of mesoporous silica

SiO_2 : P123 [wt./wt.]	S_{BET} [m^2/g]	V_t [cm^3/g]	d_{pore} [nm]
1.33 : 1	190	0.68	23.0
2 : 1	190	0.58	14.8
4 : 1	192	0.35	10.8
Silica only	197	0.15	3.1
Alumina only	284	0.31	4.4

Equation (6.1) leads to V_t = 0.16 cm^{3}g, which is very close to the value reported in Table 6.2. We may conclude that spray drying silica sol results in particles that are very closely packed. It is also evident that adding the structure-directing template P123 results in a dramatic increase of the pore volume up to 450%. Since the surface area is not affected by the addition of P123, the increased pore volume must be accompanied by an associated increase in pore diameter. Also this can be well understood by the fact that the surface area corresponds to the surface area of individual silica particles (particle size, d_p =16 nm, ρ_s = 2.196 g/cm^3), estimated to be around 171 m^2/g from:

$$\text{Surface Area} = \frac{6 \times 10^3}{\rho_s d_p} \tag{6.2}$$

This value is close to the measured BET surface area of spray dried silica solution (190 m^2/g) given in Table 6.2. On using P123, the resultant materials are composed of aggregates of silica nanospheres that are decorated around P123 assemblies. Hence, on increasing the P123 content, one observes an increase in pore volume, while the surface area remains unaltered.

6.3.2 Mesoporous silica-aluminas

These samples were prepared from precursors obtained by mixing calculated amounts of colloidal silica, peptised Catapal, and 10 wt% P123 solutions. Figures 6.4 and 6.5 show the nitrogen adsorption/desorption isotherms and the pore size distribution for two different SiO_2 : Al_2O_3 ratios of 7 and 23.4, respectively. The isotherms are of type IV with a hysteresis loop of type H1.

Table 6.3: Textural properties of mesoporous silica-aluminas for different SiO_2:Al_2O_3 ratios

SiO_2 : Al_2O_3	SiO_2 : P123		S_{BET}	V_t	d_{pore}
[mol/mole]	[wt./wt.]	[mole/mole]	[m^2/g]	[cm^3/g]	[nm]
7	1.33 : 1	128.6 : 1	258	0.61	10.8
7	2 : 1	193.3 : 1	262	0.47	10.3
7	4 : 1	386.7 : 1	292	0.34	$\sim$ 5.0
23.4	1.33 : 1	128.6 : 1	210	0.48	10.8
23.4	2 : 1	193.3 : 1	212	0.37	9.7
23.4	4 : 1	386.7 : 1	212	0.27	$\sim$ 7.1

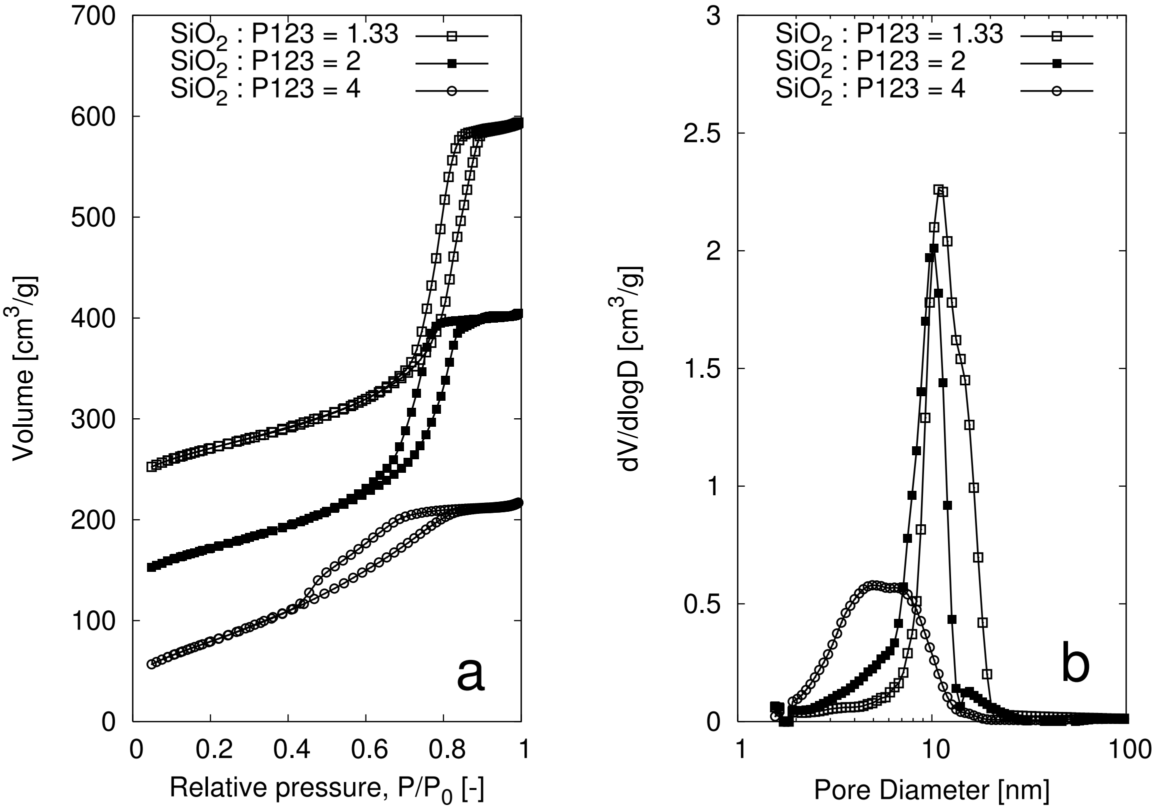

Figure 6.4: (a) N_2 adsorption/desorption isotherms and (b) pore size distribution based on the adsorption branch (model of Broekhoff and de Boer) of mesoporous silica-aluminas with SiO_2 : Al_2O_3 = 7 : 1. Isotherms corresponding to SiO_2 : P123 = 1.33 and 2 have been offset by 200 and 100 cm^3/g respectively for clarity.

From Table 6.3, one can observe that the pore volume decreases with increased SiO_2 : P123 ratio for two different SiO_2 : Al_2O_3 values, just as was observed in Table 6.2 for mesoporous silica. A clear trend with an increase in pore size is seen with a decrease in SiO_2 : P123 for SiO_2 : Al_2O_3 = 23.4. Once again, the pore size distribution is much more narrow for SiO_2 : P123 = 1.33 and 2, as compared to a value of 4. In general, materials synthesized at SiO_2 : Al_2O_3 = 7 have a slightly higher BET surface area and pore volume as compared to SiO_2 : Al_2O_3 = 23.4. It is interesting to note that at sufficiently low SiO_2 : P123 ratios, the *same* mean pore diameter is obtained, irrespective of the SiO_2 : Al_2O_3 ratio.

6.3.3 Steam stability of mesoporous silica-aluminas

Three samples of the silica-alumina materials were selected for steam stability tests. Their textural properties before and after treatment are reported in Table 6.4. One can observe a surface area (SA) retention of over 50 % and a pore volume (PV) retention of 85 % for mesoporous silica-aluminas with SiO_2 : Al_2O_3 = 7. For SiO_2 : Al_2O_3 = 23.4 one can observe a comparable but slightly lower SA and PV retention of the samples prepared using two loadings of SiO_2 : P123. These results signify that the materials are able to retain the pore network to a significant extent. This is clearly supported by the pore size distribution of the samples shown before and

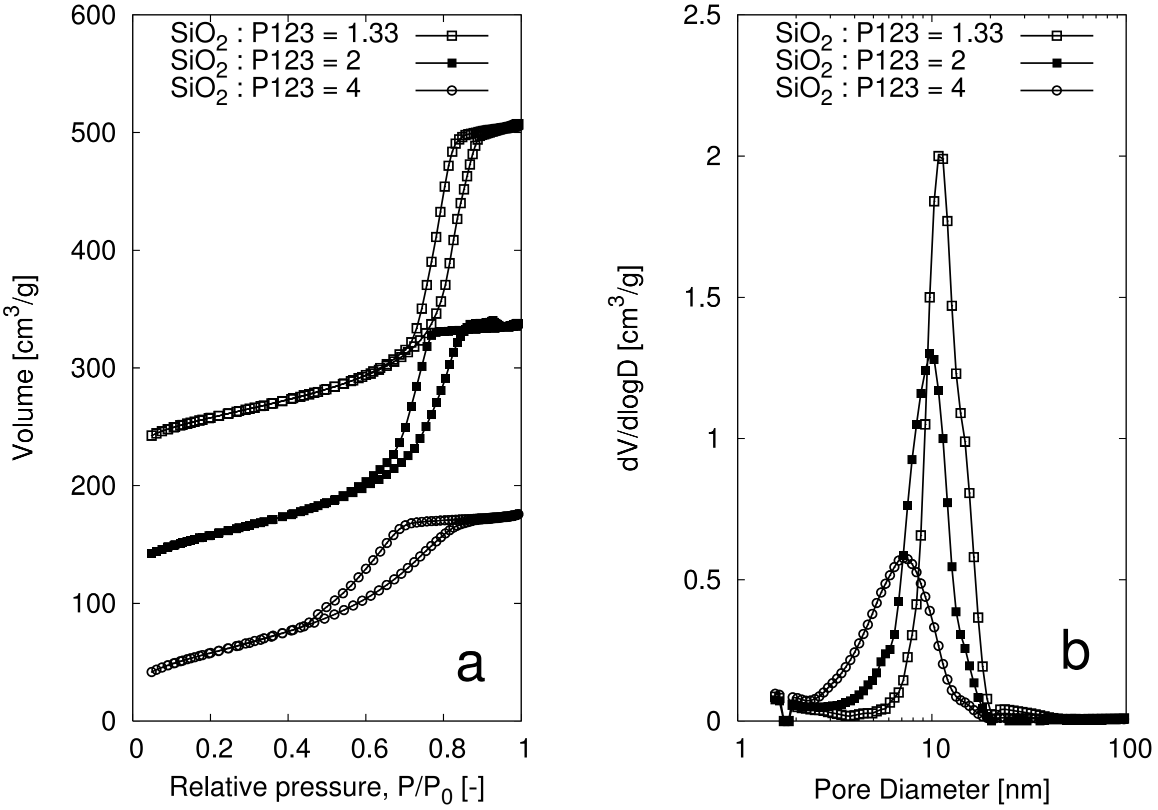

Figure 6.5: (a) N_2 adsorption/desorption isotherms and (b) pore size distribution based on the adsorption branch (model of Broekhoff and de Boer) of mesoporous silica-aluminas with $SiO_2 : Al_2O_3$= 23.4 : 1. Isotherms corresponding to SiO_2 : P123 = 1.33 and 2 have been offset by 200 and 100 cm^3/g respectively for clarity.

Table 6.4: Textural properties of mesoporous silica-aluminas before and after steam treatment

$SiO_2 : Al_2O_3$	SiO_2 : P123		S_{BET} [m^2/g]		V_t [cm^3/g]		SA	PV
[mole/mole]	[wt./wt.]	[mole/mole]	Before steaming	After steaming	Before steaming	After steaming	retention[†] [%]	retention[‡] [%]
7	1.33 : 1	128.6 : 1	258	140	0.61	0.52	54.3	85.2
23.4	1.33 : 1	128.6 : 1	210	102	0.48	0.38	48.5	79.2
23.4	4 : 1	386.7 : 1	212	79	0.27	0.21	37.3	77.8

[†] SA (surface area) retention = $S_{BET,aftersteaming}/S_{BET,beforesteaming} \times 100$

[‡] PV (pore volume) retention = $V_{t,aftersteaming}/V_{t,beforesteaming} \times 100$

after steam treatment in Figure 6.6 and 6.7. Interestingly, the mode of the distribution shifts to a larger pore size after steam treatment.

These extreme stability test conditions (100 % steam, ∼800 °C for 20h) simulate the realistic conditions prevalent in the fluidized bed catalytic cracker [13] and act as a screening prerequisite for potential catalysts. Furthermore, we emphasize that the steaming conditions used here are much more rigorous than those usually reported in literature. Xiao *et al.* [8] have reported the hydrothermal stability of SBA-15 and Al-SBA-15 under boiling water conditions for 120 h and seen a reduction in surface area by nearly 90 %. Han *et al.* [14] also tested their

SBA-15 materials by subjecting it in boiling water (100 °C) for 120 hours and observed SA retentions ranging from 9 to 16 %. They also reported the stability of mesoporous aluminosilicate (MAS) materials consisting of MFI units under similar conditions with surface area retention of 70 %. Ooi *et al.* [15] synthesized SBA-15 and Al-SBA-15, and investigated their hydrothermal stability by passing 100 % steam for a period of 1 h at 800 °C. They observed a reduction in BET surface area of 43 % for SBA-15 and 46-48 % for the Al-SBA-15 samples. Pinnavaia and co-workers [16] steamed their MSU-S materials at 800 °C, 100 % steam for 3 h and observed a retention in surface area of 5-21 % only.

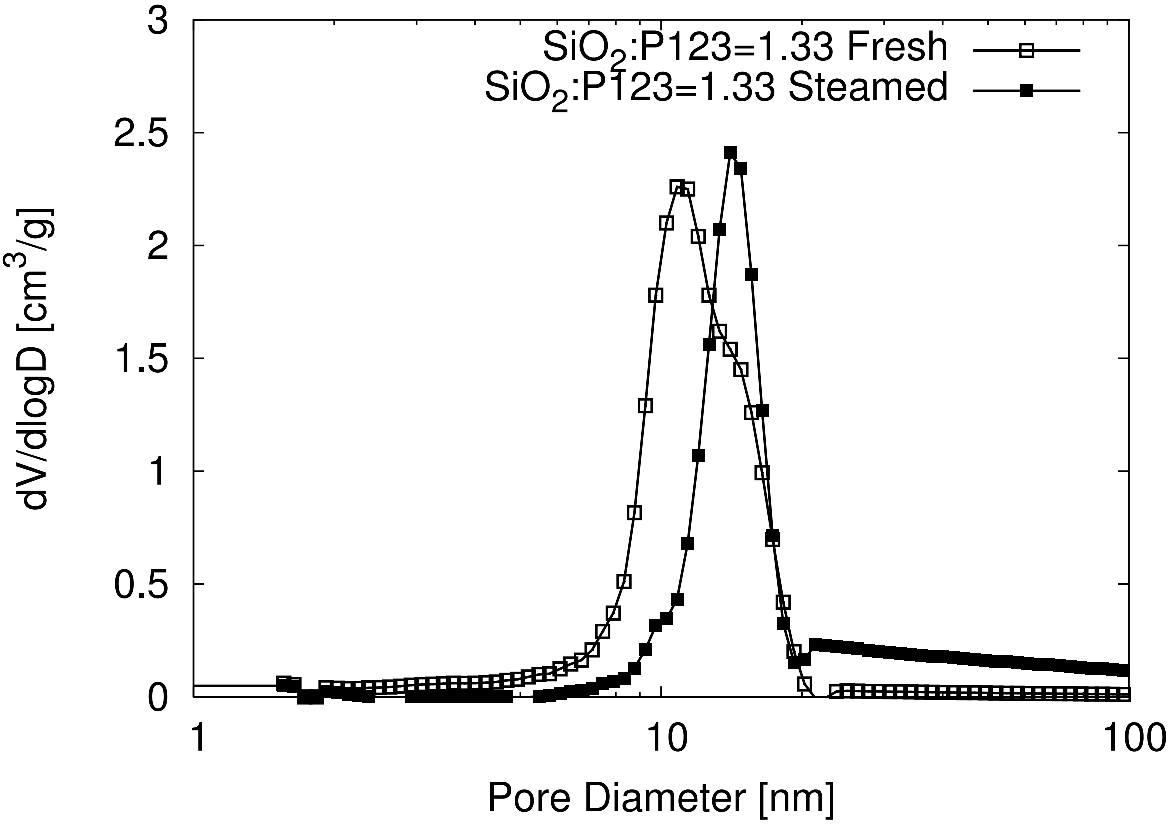

Figure 6.6: Pore size distribution of silica-aluminas (SiO_2 : Al_2O_3 = 7) before and after steam treatment

The high stability of mesoporous silica-alumina materials in the present work can be attributed to the thicker walls of the materials. The walls are composed of packings of silica and alumina nanospheres with particle sizes of 16 and 4.5 nm respectively. Such thick walls would provide the structural stability that allows them to withstand such extreme steaming conditions in comparison to amorphous, mesoporous silica like MCM-41 and SBA-15, which have relatively thin walls around 1 nm and in the range of 3-5 nm, respectively.

6.3.4 Activity tests

In literature, activity tests of mesoporous aluminosilicates are usually carried out on fresh catalyst. In this work we have carried out activity tests on the samples after the severe conditions

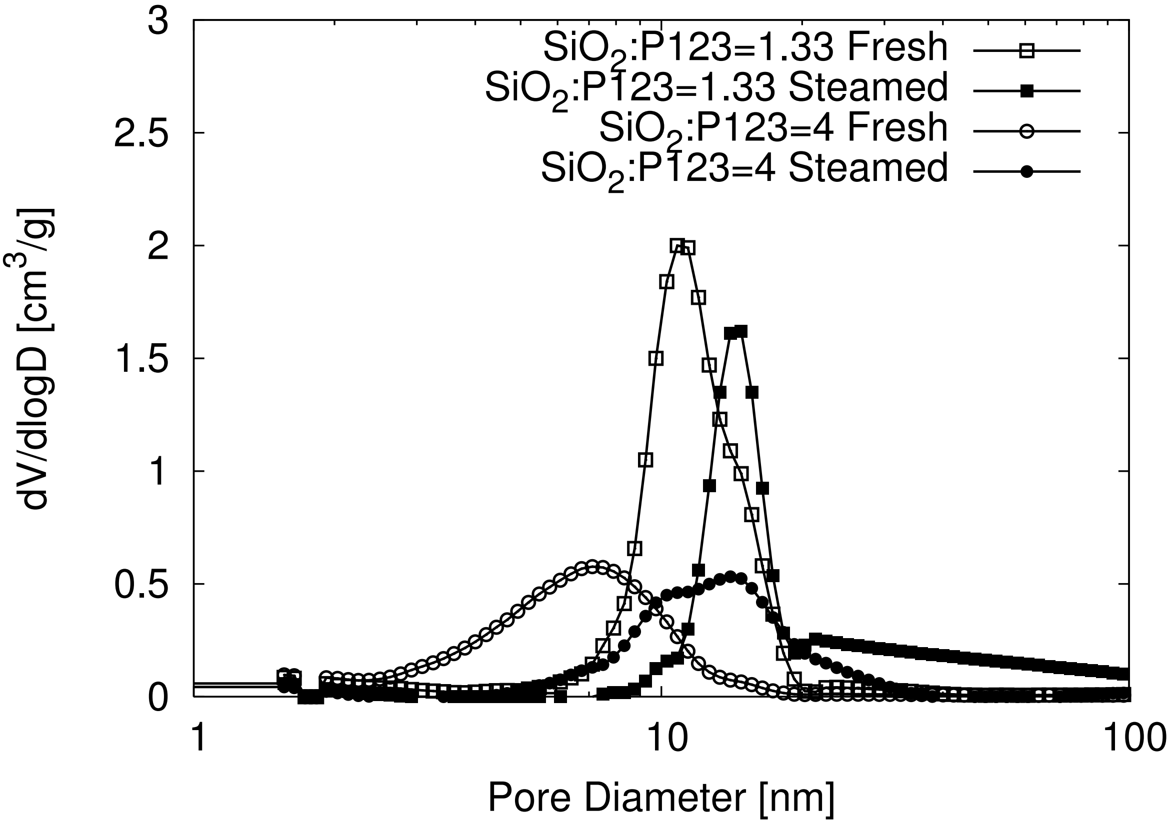

Figure 6.7: Pore size distribution of silica-aluminas ($SiO_2 : Al_2O_3 = 23.4$) before and after steam treatment

of the hydrothermal stability test resulting in loss of their active surface area. This allows us to test the activity of the catalysts after simulated exposure to the conditions representative of a commercial FCC unit.

Table 6.5 gives details on the activity tests performed on selected steamed samples using TiPB (tri-isopropyl benzene) and linear alkanes ($C_{12}H_{26}$ and $C_{14}H_{30}$) as probe molecules. The TiPB probe molecule is typically used to simulate the diffusional constraints expected in the catalytic cracking of gas oil in a FCC catalyst [17]. Initially, a blank experiment was performed to ascertain the extent of conversion as a result of thermal cracking alone. As a reference, a spray-dried sample of Catapal was added to the performance test. Note that this sample was *not* steamed prior to performance testing.

In Table 6.5, the difference in conversion between the second and first pulse gives the extent of deactivation of the catalyst material. Deactivation may be caused by, for example, deposition of coke formed from byproducts of the reaction. Table 6.5 shows that, except for the sample consisting of only alumina (fresh Catapal), no deactivation was observed. The large amount of coke formation in the alumina sample may be explained by the relative high acidity of γ-alumina. Note that the alumina sample was not steam-treated prior to testing it for activity. The reproducibility of the activity tests is shown by the consistent conversion values for the repeated activity tests of the samples with $SiO_2 : Al_2O_3 = 23.4$ and $SiO_2 : P123 = 128.6$.

Except for the sample containing only alumina, the samples do not show considerable acidity

Table 6.5: Probe molecule experiments on steamed samples (Activity tests)

Sample	Conversion of different probe molecules [%]				
	TIPB (T = 400 °C)		TIPB (T = 500 °C)	$C_{12}H_{26}$ (T = 600 °C)	$C_{14}H_{30}$ (T = 600 °C)
	1^{st} pulse	2^{nd} pulse			
Blank*	4	4	4	4	7
$SiO_2 : Al_2O_3$ = 7, SiO_2 : P123 = 128.6	9	9	30	5	8
$SiO_2 : Al_2O_3$ = 23.4, SiO_2 : P123 = 386.7	6	6	16	7	9
$SiO_2 : Al_2O_3$ = 23.4, SiO_2 : P123 = 128.6	6	6	14	4	6
$SiO_2 : Al_2O_3$ = 23.4, SiO_2 : P123 = 128.6 repeat	6	6	15	6	8
Fresh Catapal (68.4 % Al_2O_3)	14	9	33	38	58

* Blank experiment: no catalyst loaded, thermal cracking alone

for the linear alkanes. For the alumina sample, the reported activity numbers are misleading, since the cracking for normal alkanes is non-selective, and results in the formation of coke on the catalyst. All samples show considerable activity for the conversion of TiPB. The sample containing only alumina, which was not steam treated, has a conversion of 33 %, and serves as a reference. Table 6.5 shows that the sample $SiO_2 : Al_2O_3$ = 7 has a nearly equal conversion of 30 %. Comparing the surface area of the alumina sample (Table 6.2, SA = 284 m^2/g) to that of the steamed $SiO_2 : Al_2O_3$ = 7 sample (Table 6.4, SA = 127 m^2/g) shows that the silica-alumina composite has a significantly higher reaction rate per unit surface area than the alumina sample. This may be attributed to the increased accessibility, because of the larger pore diameter created by the synthesis in the presence of P123, and/or the creation of active sites on the interface where the silica and alumina particles touch.

Comparing the activities of the silica alumina samples with $SiO_2 : Al_2O_3$ = 7 and $SiO_2 : Al_2O_3$ = 23 for the same ratio SiO_2 : P123 = 128.6 shows that the conversion of TiPB drops from 30 % to 14 %. Since both silica-alumina composites have approximately the same pore diameter, we must attribute this difference in observed activity to differences in intrinsic activity, *i.e.*, to differences in the properties of the active site on the surface of the material, and not to differences in accessibility. Comparing the surface area of the steamed sample with $SiO_2 : Al_2O_3$ = 23.4 (Table 6.4, SA = 90 m^2/g) to that of the alumina sample (Table 6.2, SA = 284 m^2/g), we conclude that the activity per unit surface area of the silica-alumina composite sample is higher than that of the fresh alumina.

6.4 Conclusions

In conventional zeolite synthesis, microporous crystalline structures are created from inorganic silica and alumina species dissolved in the aqueous phase. The final crystalline product is obtained after prolonged reaction times (several hours). In the synthesis of novel mesoporous materials reported in the literature, mostly silicon alkoxides are used as raw material, and the ordered materials are obtained after long reaction times.

In the present study, we have synthesized novel mesoporous silica-alumina materials by self-assembly of nanosized silica and alumina particles using a structure-directing agent. This process results in a non-crystalline material composed of a packing of silica and alumina nanoparticles. We have shown that the pore size of these materials is governed by the amount of structure-directing agent, and that it is *independent* of the silica-to-alumina ratio of the samples. Severe thermal stability tests (100 % steam at T = 788 °C for 20 hours) showed that the prepared mesoporous materials retain much of their mesoporous structure. This is far superior to usually reported crystalline aluminosilicate mesoporous materials in the literature. Reactivity tests, based on the conversion of TiPB, have shown that the activity of the samples depends on the silica-to-alumina ratio of the materials. Apparently, by using “nanosized building blocks” comprised of silica and boehmite particles, the surface reactivity towards TiPB conversion may be adjusted.

These findings create new, exciting opportunities for the synthesis of catalytic cracking catalysts, because the catalytic activity of the material is apparently *decoupled* from the pore size. A structure-directing agent (*e.g.*, P123 in the present study, but other ones may be applied as well) may be employed to adjust the mesopore size, while the catalytic activity may be adjusted by tuning the silica-to-alumina ratio. With this technique, the accessibility of the catalyst and the reactivity at the catalyst surface might be independently designed to match the requirements of a specific feed.

It was shown that the mesoporosity can be adjusted by adding a structure-directing template. Various formulations of the ethylene oxide / propylene oxide block copolymers are available, leading to different structure-directing templates. It is worthwhile exploring these templates in combination with the industrial silica and alumina raw materials used in the present study. It was shown that the applied silica-to-alumina ratio affects the intrinsic activity as well. We may speculate that this is caused by the formation of catalytically active silica-alumina materials at the boundary where the silica and alumina particles touch. It would be worthwhile to explore different industrially available silica and boehmite sources to investigate their effect on the reactivity of the synthesized materials.

References

1. J.S. Kresge, M.E. Leonowicz, W.J.Roth, J.C. Vartuli, J.S. Beck, Nature 359 (1992) 710.
2. D. Zhao, J. Feng, Q. Huo, N. Melosh, G.H. Fredrickson, B.F. Chemlka, G.D. Stucky, Science 279 (1998) 548.
3. R. Pitchumani, W. Li, M.-O. Coppens, Catal. Today 105 (2005) 618.
4. Y. Lu, H. Fan, A. Stump, T. L. Ward, T. Rieker, C. J. Brinker, Nature 398 (1999) 223.
5. N. Baccile, D. Grosso, C. Sanchez, J. Mater. Chem. 13 (2003) 3011.
6. R. Pitchumani, A. Schmidt-Ott, M.-O. Coppens, Proc. PARTEC Int. Congress, Nuremberg, Germany, March 2007.
7. A. Corma, M.S. Grande, V. Gonzalez-Alfaro, A.V. Orichilles, J. Catal. 159 (1996) 375.
8. P. Kortunov, S. Vasenkov, J. Krger, M. F Ela, M. Perez, M. Stcker, G.K. Papadopoulos, D. Theodorou, B. Drescher, G. McElhiney, B. Bernauer, V. Krystl, M. Kocirik, A. Zikanova,

H. Jirglova, C. Berger, R. Glser, J. Weitkamp, F.W. Hansen, Magnetic Resonace Imaging 23 (2005) 233.

9. F.-S. Xiao, Catal. Surveys from Asia 8 (2004) 151.
10. X. Pang, F. Tang, Micropor. Mesopor. Mater. 85 (2005) 1.
11. J.M. Morales, J. Latorre, C. Guillem, A. Beltrn-Porter, D, Beltrn-Porter, P. Amors, Solid State Sciences 7 (2005) 415.
12. J. C. P. Broekhoff, J. H. de Boer, J. Catal. 9 (1967) 8.
13. X. Dupain, M. Makkee, J.A. Moulijn, Appl. Catal. A. 297 (2006) 198.
14. Y. Han, S. Wu, Y. Sun, D. Li, F. Xiao, Chem. Mater. 14 (2002) 1144.
15. Y.-S. Ooi, R. Zakaria, A. R. Mohamed, S. Bhatia, Catal. Comm. 5 (2004) 441.
16. K. S. Traintafyllidis, A. A. Lappas, I. A. Vasalos, Y. Liu, H.Wang, T. J. Pinnavaia, Catal. Today 112 (2006) 33.
17. E. F. Aguiar, M. L. Murta Valle, M. P. Silva, D. F. Silva, Zeolites 15 (1995) 620.

Chapter 7

Aerosol assisted synthesis of mesoporous ZSM-5 composites

7.1 Introduction

Microporous crystalline aluminosilicates, namely zeolites, are widely employed in a large number of technological applications. Zeolites serve as excellent catalysts in a variety of processes, on account of their uniform micropores (pore size less than 2 nm), most importantly in oil-refining and petrochemical synthesis. In addition, they are increasingly applied in environmental catalysis and in the synthesis of fine chemicals [1, 2].

Despite the vast applications of zeolites, it is often seen that the small pore sizes inherent to these materials lead to severe diffusion limitations that contribute to sub-optimal performance. One way to overcome this is to reduce the size of the zeolite crystals down to nanoscale dimensions. Nanocrystalline zeolites are promising catalytic and adsorbent materials that have high surface areas and reduced diffusion path lengths relative to conventional micrometer-sized zeolites [3]. This also leads to higher accessibility of the catalytic sites on account of the increased external surface area [4]. Nanocrystalline zeolites can be assembled into micropatterned thin films [5], and have potential applications in separation processes (membranes) and chemical sensors [5, 6].

ZSM-5 is a zeolite that is often used as a catalyst in petroleum refining. It has an intersecting pore network composed of straight channels and zigzag channels with pore diameters of around 0.55 nm. Nanocrystalline ZSM-5 has been shown to exhibit increased selectivity in toluene conversion into cresol and significantly decreased coke formation relative to conventional ZSM-5 materials [7].

There are several reports on different strategies to synthesize nanocrystalline ZSM-5. Schoeman *et al.* [8] reported the synthesis of nanocrystalline ZSM-5 using clear solutions in open beakers at low temperature and ambient pressure, in contrast to the conventional hydrothermal routes. These syntheses resulted in the formation of colloidal solutions of zeolites with uniform particle sizes of 100 nm or less. Van Grieken and co-workers [9] reported a similar synthesis for ZSM-5 based on clear solutions under hydrothermal conditions. Jacobsen and co-workers developed a technique in which the zeolite synthesis mixture was impregnated into a porous carbon black material [10]. The zeolite crystal growth was restricted by the pore size of the carbon black matrix. This method was hindered by the fact that the carbon black material is disordered, and, hence, zeolites with a rather broad size and shape distributions were produced.

However, nanosized zeolites cannot be used directly, due to their intrinsically poor stability and due to the much higher pressure drops in packed-bed reactors compared to those obtained with conventional catalysts. Therefore, nanozeolites need to be dispersed and stabilized in a porous matrix. A hierarchical porous system consisting of interconnected micropores and mesopores was obtained by dispersing nanosized beta zeolite in mesoporous TUD-1. This hierarchical porous system showed enhanced cracking activity of n-hexane (per gm of zeolite) as compared to pure beta-zeolite [11]. Several strategies have been reported that combine the advantages of mesoporous materials and those of zeolites. Huang *et al.* [12] reported the synthesis of MCM-41/ZSM-5 composite materials containing an interconnected mesoporous and microporous structure using a dual template method via two-step crystallization. Pinnavaia and coworkers [13] reported the assembly of zeolite seeds (such as zeolite Y, ZSM-5) as precursors or building units into steam stable hexagonal aluminosilicate mesostructures. Kaliaguine and co-workers [14] have reported approaches for preparation of ultrastable and highly acidic mesoporous aluminosilicates via coating of mesoporous materials with zeolite gel or via secondary templated crystallization of zeolites starting from amorphous mesoporous materials. Xia and Mokaya [15] have prepared ZSM-5/MCM-48 aluminosilicate composite materials using a simple two-step crystallization process. The synthesis process involved the assembly of precursor zeolite species, containing ZSM-5 units at various stages of crystallization, into a mesostructured material.

In the present work, an attempt is made to synthesize composites consisting of zeolite nanocrystals embedded in a mesoporous framework using aerosols. This involves synthesizing a precursor consisting of ZSM-5 nanocrystals well dispersed in an aqueous solution. In the aerosol droplets, the zeolite is incorporated into a mesoporous framework whose mesopore size is controlled using a non-ionic surfactant, P123.

7.2 Experimental

Initially, several strategies were employed towards the goal of synthesizing mesoporous ZSM-5 composites. This involved spraying solutions containing ZSM-5 nanocrystals dispersed in distilled water (after separation from the mother liquor obtained by ageing the zeolite precursor) to form agglomerates with porosity arising from the interparticle space. The resultant materials were of limited use, because of their comparatively low external surface area and total pore volume, due to the large zeolite particle size.

In an attempt to develop a one-pot strategy, a highly basic colloidal zeolite nanocrystal solution (also containing unreacted TEOS and TPAOH) was mixed with an aqueous/ethanolic P123 solution. The objective was that the tri-block copolymer, P123, would act as template and interact mainly with the unreacted TEOS to form an amorphous mesostructure (driven by evaporation-induced self assembly) and the zeolite crystals would be embedded in this mesostructure. However, the synthesized materials showed negligible microporosity. The XRD analysis showed no diffraction peaks. This could be due to the fact that P123 no longer functions as a template under such high basic conditions. Additionally, droplet evaporation during the aerosol process

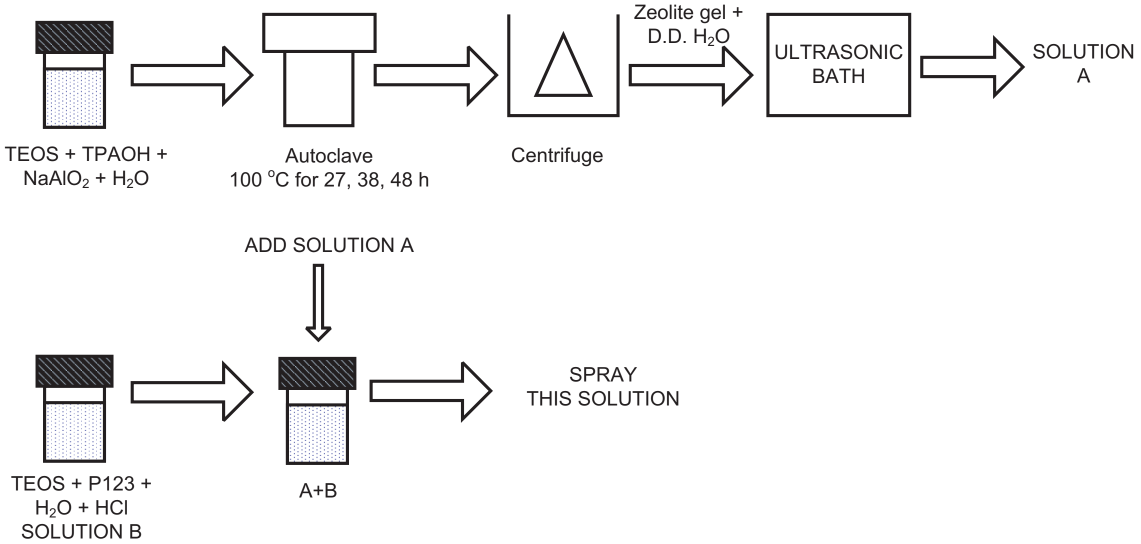

Figure 7.1: Synthesis scheme for producing mesoporous ZSM-5 composites

leads to increased alkalinity, which could dissolve the microporous network of the zeolite.

Therefore, a different synthesis strategy was employed, which showed encouraging results and is illustrated in Figure 7.1.

7.2.1 Precursor preparation

The precursor solution preparation involved several steps.

ZSM-5 precursor solution

1. Dissolve 200 mg $NaAlO_2$ in 20.8 ml H_2O : A1
2. Mix 13.8 ml 20 % TPAOH with 11.2 ml TEOS to get a clear solution : A2
3. Add A1 to A2 and stir to get a clear solution

Molar composition $Al_2O_3 : SiO_2 : Na_2O : (TPA)_2O : H_2O$ = 1 : 50 : 1 : 7 : 1800.

The above solution was aged in an autoclave at 100 °C for different times: 27, 38 and 48 h. The zeolite gel was then separated from the mother liquor by centrifugation.

Zeolite gel dispersion

The zeolite gel, separated from the mother liquor, was well dispersed in 20 ml D.D. H_2O using an ultrasonic bath for 30 minutes. This solution is denoted as A.

P123 + TEOS solution

1. Dissolve 2.15 g P123 in 36 µl 37 wt% HCl + 5.32 ml 100 wt% EtOH + 35.8 ml D.D. H_2O.
2. Add 3.53 ml 98 % TEOS to get a clear solution. This solution is denoted as B.

Final precursor solution

Solution A was then added to Solution B and stirred at room temperature to obtain the final precursor. This solution was composed of 5 wt% P123 and 10 wt% EtOH. The HCl used was added to keep the pH close to 2.

7.2.2 Aerosol equipment and synthesis conditions

The same aerosol equipment as described in Chapter-5 was used in these experiments. The only difference is that a 1-jet nebulizer was used instead of a 6-jet nebulizer. Nitrogen was used as a carrier gas at a flow rate of 2.0 l/min. The temperature of the furnace was maintained at 400 °C. The collection filter was maintained at 80 °C. The as synthesized powders were calcined at 250 °C for 3 h followed by 550 °C for 6 h at a heating rate of 5 °C/min to remove the organic template.

7.2.3 Material characterization

The calcined samples were analyzed using a Quantachrome Autosorb-6B sorption analyzer to measure the nitrogen adsorption/desorption isotherms. Prior to the isotherm measurements, the samples were degassed at 350 °C overnight.

The powder X-ray diffraction patterns were recorded on a Siemens D5005 Crystalloflex diffractometer, which is equipped with an incident beam Cu Kα Ge focussing monochromator and a Braun position sensitive detector.

7.3 Results and discussion

Fig. 7.2 shows the N_2 adsorption/desorption isotherms and the pore size distribution of the synthesized materials obtained using zeolite nanocrystal gels synthesized for different ageing times in the initial sol-gel step. For the purpose of comparison, a sample was also prepared by using the same zeolite precursor, and by synthesizing large zeolite crystals after ageing them for 48 h. This is labeled as *48h sol-gel*. This material was prepared in batch and not by using the aerosol method.

It is clearly seen from the adsorption branches of the isotherms of Figure 7.2 that there is an uptake of nitrogen at a high relative pressure, greater than 0.8. This is reflected in the pore size distribution obtained by applying a BJH pore model to the adsorption branch of the isotherms. The pore size distribution is relatively broad, though centered around 30 nm. On the other hand, one also observes that there is a progressively decreasing desorption isotherm starting from relative pressure, P/P_0 of 1.0 with a distinct desorption step at a relative pressure of 0.5. This could suggest the presence of a pore network consisting of an entrance with an increasing pore width leading to the 30 nm inner mesopore structure. Furthermore, the opening of the entrance is much smaller than the inner pore size, suggesting an ink-bottle pore system.

The textural properties of the synthesized materials are given in Table 7.1. All the synthesized materials (27h, 38h and 48h) possess an external surface area in excess of 150 m^2/g and a very

Table 7.1: Textural properties of the calcined materials

Time [h]	S_{BET} [m^2/g]	S_{ext} [m^2/g]	V_t [cm^3/g]	V_{μ} [cm^3/g]	Crystal size [nm]
27	321	213	0.99	0.049	41
38	285	155	1.00	0.063	50
9	300	163	1.03	0.064	49
48 (sol-gel)	295	104	0.30	0.084	53

high total pore volume of around 1.00 cm^3/g. There is a significant micropore volume 0.049 - 0.063 cm^3/g that is on account of the micropores in the zeolite structure (due to the TPAOH template molecules) and the micropores introduced in the walls of the mesoporous framework due to the EO blocks of the tri-block co-polymer, P123.

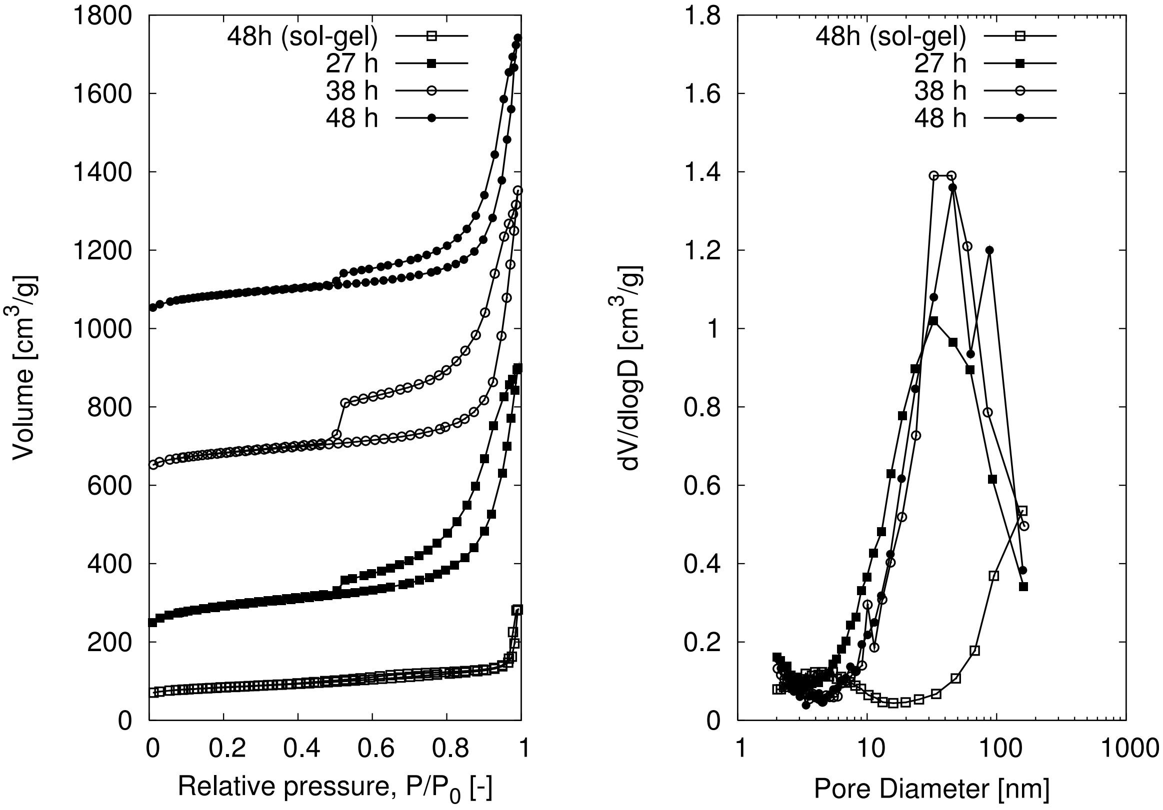

Figure 7.2: N_2 adsorption/desorption isotherms and pore size distribution (by applying the BJH model to the adsorption branch of the isotherm) of synthesized samples (Isotherms of 27 h, 38 h and 48 h offset by 200, 600 and 1000 cm^3/g)

The non-uniform nature of the mesopore network can be attributed to interference of the zeolite crystals during the surfactant-silica self-assembly process. The large mesopore volume of the composite materials is given by V_t - V_{μ}, and is due to pores created by the presence of P123, as can be observed by comparing the “48 sol-gel” sample with the other ones.

Figure 7.3 shows the XRD patterns of the calcined samples. The “48h sol-gel” sample exhibits sharp diffraction peaks corresponding to the MFI crystal lattice group. The peaks corresponding to MFI in the sample synthesized using the gel aged for 27 h are very broad, indicating small nanocrystals. The crystal size estimated from Scherrer's equation is given in Table 7.1. It can be seen that there is not much change in the crystal size with increasing ageing time of the zeolite precursor solution. However, on increasing the ageing time of the gel, the peaks grow in intensity, indicating an increased crystallinity of the samples. In other words, there is an increase in the number of zeolite nanocrystals in the final composite material.

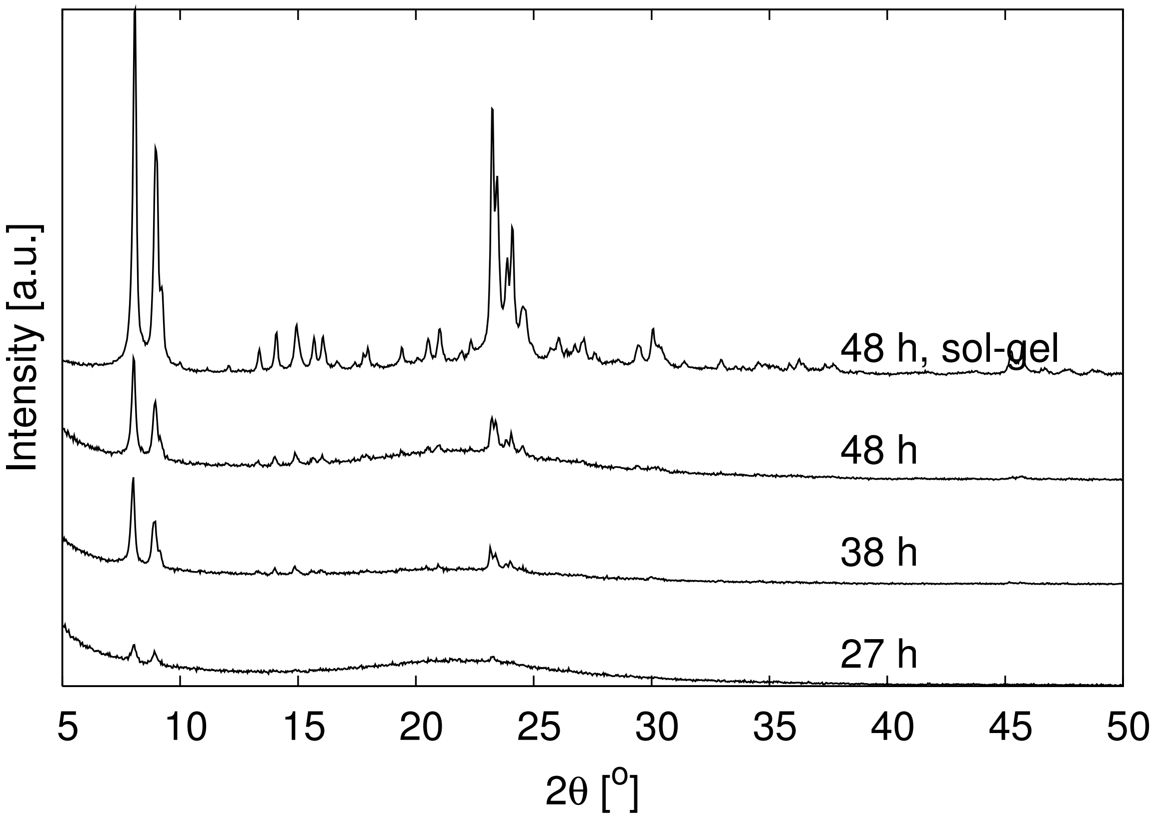

Figure 7.3: X-ray diffraction patterns of the synthesized samples

7.4 Conclusions

The aerosol technique was successfully used to incorporate ZSM-5 nanocrystals inside a mesoporous framework using P123 as the templating agent. The synthesized composites contain large mesopores centered around 30 nm with a rather broad distribution, and have a large pore volume of about 1.0 cm^3/g. XRD patterns confirmed the presence of ZSM-5 in the composite materials. The combination of small zeolite crystallites and wide mesopores should lead to improved accessibility (markedly reduced diffusion limitations) in these materials. These properties, combined with the acidity of the ZSM-5 crystals, make these materials interesting candidates for further catalytic studies, in particular for the cracking of bulky molecules.

References

1. A. Corma, Chem. Rev. 95 (1995) 559.
2. C. Perego, P. Ingallina, Catalysis Today 73 (2002) 3.
3. W. Song, R. E. Justice, C. A. Jones, V. H. Grassian, S. C. Larsen, Langmuir 20 (2004) 8301.
4. M. Yamamura, K. Chaki, T. Wakatusuki, H. Okado, K. Ffujimoto, Zeolites 14 (1994) 643.
5. S. Mintova, T. Bein, Microporous Mesoporous Mater. 50 (2001) 159.
6. L. Huang, Z. Wang, J. Sun, L. Miao, Q. Li, Y. Yan, D. Zhao, J. Am. Chem. Soc. 122 (2000) 3530.
7. B. Vogel, C. Schneider, E. Klemm, Catal. Lett. 79 (2002) 107.
8. B. J. Schoeman, J. Sterte, J.E. Ottstedt, Zeolites 14 (1994) 110.
9. R. Van Grieken, J. L. Sotelo, J. M. Menendez, J. A. Melero, Microporous Mesoporous Mater. 39 (2000) 135.
10. C. J. H. Jacobsen, C. Madsen, T. V. W. Janssens, H. J. Jakobsen, J. Skibsted, Microporous Mesoporous Mater. 39 (2000) 393.
11. P. Waller, Z. Shan, L. Marchese, G. Tartaglione, W. Zhou, J. C. Jansen, T. Maschmeyer, Chem. Eur. J. 10 (2004) 4970.
12. L. Huang, W. Guo, P. Deng, Z. Xue, Q. Li, J. Phys. Chem. B 104 (2000) 2817.
13. Y. Liu, W. Zhang and T. J. Pinnavaia, J. Am. Chem. Soc. 122 (2000) 8791.
14. D. T. On and S. Kaliaguine, Angew. Chem., Int. Ed. 40 (2001) 3248.
15. Y. Xia, R. Mokaya, J. Mater. Chem. 14 (2004) 863.

Summary

Aerosol Assisted Synthesis of Nanostructured Silica

Despite the wide applications of zeolites, especially as fluidized catalytic cracking (FCC) catalysts, there is a need to overcome the problem of diffusion limitations of the reacting bulk molecules, owing to the small pore size of these crystalline aluminosilicates. This has led to the discovery of ordered mesoporous silicas with tunable large mesopore structures, which have been proposed as ideal, rationally designed catalyst supports. They have attracted a great deal of interest amongst the materials community, due to their versatile applications, including catalysis, sensors, low-dielectric constant materials, optical waveguides and micro-fluidic devices.

The initial chapters (Chapter 1 and 2) of the present thesis dealt with the batch sol-gel synthesis of nanostructured SBA-15, which contains hexagonally ordered large mesopores and has better hydrothermal stability than MCM-41, due to its thicker pore walls. We were able to synthesize a variety of unique morphologies by tuning a single parameter, namely the stirring rate during the low temperature hydrothermal treatment step in the presence of a weak acid, $\mathrm{H_3PO_4}$. Under static conditions, free standing films were obtained at the air-water interface, and a hierarchical porous cake (containing mesopores and macropores) composed of closely packed particulate grains simultaneously precipitated. Under slow stirring conditions, bundles were formed extending over several hundred µm in length and with a width of at least 50 µm. The bundles were composed of long thin thread-like structures fused together. Materials prepared under vigorous stirring conditions resulted in fiber-like morphologies, and close examination indicated the presence of several individual segments coupled together along their length. All the materials were well ordered on a nanoscale and had a high BET surface area, as confirmed by X-ray diffraction and N_2 adsorption measurements, respectively. Transmission electron micrographs (TEM) of a microtomed section of the film revealed that the nanochannels were parallel to the surface. Furthermore, it was interesting to note that the bundles were composed of uniform nanochannels oriented along the long axis of the bundles. The different shear rate associated with different stirring conditions influences the shape and aggregation of micelles, as well as the interfacial growth of the silica-surfactant mesophase, resulting in distinct morphologies. The presence of phosphorous in the final calcined materials, as shown by XRF measurements, improved the overall Brønsted acidity of the SBA-15 material, making it a promising selective heterogeneous catalyst for reactions that specifically require Brønsted acidity.

Pulsed field gradient (PFG) NMR measurements were performed on the nanostructured SBA-15 fibers and bundles. These measurements gave further insight into the diffusion properties of these mesostructured materials. It was observed that the displacement of nitrobenzene in the

channel direction within the mesoporous bundles is well described by a model using a constant diffusivity. This means that over the observed displacements of 4 μm, molecular transport in the longitudinal direction is not affected by additional transport resistances that might confine the propagation. The channels are to a certain extent permeable which is consistent with the fact that the walls of the SBA-15 mesopores are microporous. In the bundles, there is a tendency that displacements perpendicular to the mean channel direction proceed at a rate increasing with increasing observation time, which strongly suggests the absence of a perfect channel structure over distances of 1 μm, encouraging propagation perpendicular to the mean channel direction. In the fibers, both diffusivities are found to (slightly) decrease with increasing observation time, which points to a retarded propagation over longer distances, in contrast to what is observed in the bundles. This agrees well with the morphology of the fibers, which are basically composed of short segments joined together, accounting for confinement within a more narrow space than in the bundles.

It should be noted that mesostructured silica is usually synthesized in batch using the sol-gel technique, which requires several days to obtain the final structured product. An alternative, more recent synthesis approach, namely "evaporation-induced self-assembly" (EISA) of aerosols, enables continuous production of porous silica particles with a controlled morphology and pore size within a process time of only a few seconds. An apparatus was constructed consisting of an atomizer to generate a fine aerosol of droplets, which is transported through a heated tubular reactor, in which particles are formed; the product is collected on a membrane filter. The number of experimental parameters that potentially influence the final texture of the materials is very large. The question then is which (combinations of) parameters lead to which morphology, and which ones have the largest influence? In order to probe the high-dimensional experimental parameter space, a rigorous statistical methodology was applied that allows to greatly reduce the number of experiments. A clear, homogeneous acidic precursor solution containing an organosilicate (TEOS) and a triblock copolymer (P123) as the template is atomized into an aerosol that is transported through a heated tubular reactor, as described above. Silica and surfactant micelles self-assemble with simultaneous hydrolysis-condensation of TEOS, resulting in organic-inorganic composites. High-temperature calcination results in nanoporous silica particles consisting of lamellar or hexagonal nanostructures. Experiments were based on a factorial design methodology for a more comprehensive study into the effects of precursor composition and reactor temperature on the texture of the synthesized materials. This methodology allows simultaneous investigation of the influence of multiple parameters, which is advantageous over the traditional form of experimentation in the nanomaterials community, where only one variable is changed at a time. It allows exploration over a wider range of conditions to highlight the true nature (global/local) of trends that are often misinterpreted as a universal occurrence in conventional experimental trials. The analysis showed that all of the following variables were significant: P123/TEOS was identified as having the maximum effect on the BET surface area, followed by H_2O/TEOS, temperature, and EtOH/TEOS. P123 and EtOH have an important combined effect as well. Furthermore, temperature has a maximum influence on the pore volume as compared to other variables. Using contours, this method exclusively determined multiple conditions for achieving a required surface area and pore volume. It also illustrated the variation of these properties over a wider domain of experimental conditions. N_2 adsorption measurements showed that a high P123/TEOS results in particles with a broad pore size distribution. Lower ratios favour formation of a network with uniformly sized pores. The structural order and nanostructure were elucidated by X-ray diffraction (XRD) and transmission electron microscopy (TEM). In the field of materials science, it is often encountered that the synthesis involves fine-tuning several experimental variables in order to achieve a desired product. This is usually done by extensive trial and error. By using the techniques described here, one can identify and narrow down to the variables, or combinations of variables that have a significant effect on the property of the material under scrutiny, and this with a minimum of experimental runs. This information could be used as a basis for additional experiments to improve the quality of the material by fine-tuning these significant variables. In addition, the empirical facts derived can serve as a basis for understanding and modeling of a complex process such as EISA.

A large laboratory spray drier at Albemarle Catalysts was used to synthesize novel mesoporous silica and silica-alumina materials by self-assembly of nanosized silica and alumina particles, using P123 as a structure-directing agent. This process results in an amorphous material composed of a packing of silica and alumina nanoparticles. We have shown that the pore size of these materials is governed by the amount of structure-directing agent, and that it is independent of the silica-to-alumina ratio of the samples. Severe hydrothermal stability tests (100 % steam at T = 788 °C for 20 hours) showed that the prepared mesoporous materials retain much of their mesoporous structure. This is far superior to the crystalline aluminosilicate mesoporous materials that are usually reported in literature. Reactivity tests, based on the conversion of TiPB, have shown that the activity of the samples depends on the silica-to-alumina ratio of the materials. Apparently, by using ”nanosized building blocks” comprised of silica and boehmite particles, the surface reactivity towards TiPB conversion may be adjusted. These findings create new exciting opportunities for the synthesis of catalytic cracking catalysts, because the catalytic activity of the material is apparently decoupled from the pore size. A structure-directing agent (e.g., P123 in the present study, but other ones might be applied as well) may be employed to adjust the mesopore size, while the catalytic activity may be adjusted by tuning the silica-to-alumina ratio. With this technique, the accessibility of the catalyst and the reactivity at the catalyst surface may be independently designed to match the requirements of a specific feed. It is worthwhile exploring these templates in combination with the industrial silica and alumina raw materials used in the present study. It was shown that the applied silica-to-alumina ratio affects the intrinsic activity as well. We may speculate that this is caused by the formation of catalytically active silica-alumina materials at the boundary where the silica and alumina particles touch. It would be worthwhile to explore different industrially available silica and boehmite sources to investigate their effect on the reactivity of the synthesized materials.

Finally, an attempt was made to synthesize composites consisting of zeolite nanocrystals embedded in a mesoporous framework using aerosols. This involves first synthesizing a precursor consisting of ZSM-5 nanocrystals well dispersed in an aqueous solution. When spraying this precursor together with a P123 solution, the zeolite nanocrystals are incorporated into a mesoporous framework in the aerosol phase. The synthesized composites contain large mesopores centered around 30 nm with a rather broad distribution and a large pore volume of 1.0 cm^3/g. XRD patterns confirmed the presence of ZSM-5 features in the composite materials. This should markedly reduce diffusion limitations. These materials with improved accessibility, combined with the acidity of the ZSM-5 crystals, would serve as ideal candidates for cracking bulky molecules.

This thesis demonstrates that the aerosol method dramatically reduces the synthesis time of interesting novel mesoporous and zeolite/mesoporous composite materials, as compared to the sol-gel scheme. One could always use a homogeneous precursor or, for that matter, a well dispersed system to generate a wide array of materials in a matter of seconds. It would be worthwhile to study in greater detail the synthesis of the mesoporous ZSM-5 composites by varying the Si/Al ratio and also tune the mesoporous framework acidity in accordance with the required applications.

Appendix A
Nanoporous silica production by spray drying of colloidal nanoparticle solutions

Introduction

The production of nanostructured materials via spray drying has gained considerable interest, because the produced particles exhibit unique properties that make them potential candidates for use in catalysis, chromatography, fillers, pigments and cosmetics [1]. Spray drying is an established method involving atomizing and spraying suspensions or homogeneous solutions into droplets, which dry to form solid particles [2]. It provides an efficient way to produce particles continuously with a mostly spherical morphology with sizes ranging from below 1 μm to microns. Advantages include the simplicity of the system, its cost effectiveness, and the ability to scale up production to the order of tons. Several authors have reported the synthesis of micrometer-sized particles by using spray drying [2-4]. Iskander *et al.* [4] prepared agglomerated silica powders with a spherical morphology by spray drying different colloidal silica nanoparticle solutions. By changing the primary particle size, the pore size arising due to the interparticle porosity of the agglomerated particles was controlled. It was demonstrated that the final product size could be varied by changing the initial concentration of the colloidal suspension. Additional Eu-doped luminescent silica powders were prepared by incorporating Eu^{3+} into the silica matrix, demonstrating the ease of functionalizing materials using spray drying.

Colloidal silica is a good precursor for spray drying since it is stable, it can be dispersed in water, and the primary particle size can be controlled with nanometer resolution. Ohshima *et al.* [5] prepared silica-titania powders using 15 nm colloidal silica nanoparticle suspensions. The morphological control of nanostructured particles prepared by spray drying of a nanoparticle sol was investigated, and supported by theory [4]. The structural stability of a droplet and the hydrodynamic effects during the drying process play a crucial role in determining the morphology of the final particles. The colloidal particle size in the droplet, droplet size, viscosity, drying temperature, and gas flow rate all influence the final morphology. Spherical particles were obtained under conditions of small droplet size with large and small colloidal particle sizes. On the other hand, toroidal particles were produced from large droplets, at high temperatures and high gas flow rates. Larger colloidal silica sub-micron particle solutions (250 and 500 nm) with high monodispersity have also been spray dried to form spherical agglomerates using small colloidal silica nanoparticles (25 nm) as a binder [6]. This resulted in agglomerates with a bimodal pore size distribution, and increased overall specific surface area. Such particles were used as model carriers in the heterogeneously catalyzed polymerization of ethylene. It was also observed that the prepared model carriers showed similar activities to commercially available polymerization carriers, despite their low surface areas, due to the fact that the polymerization process depends on the geometrical and structural aspects of the carriers rather than on the specific surface area. Agglomerated spherical silica particles have been demonstrated as a more suitable calibration aerosol for testing the performance of high efficiency air filters, substituting the more harmful and expensive dioctylpthalate (DOP) particles [7]. The characteristics of the generated SiO_2 particles in terms of electrical mobility and light scattering were investigated, and were found to satisfy the requirements for a calibration aerosol, with the added advantages of being cheap and environmentally friendly.

Experimental procedure

Pressurized air (1.0 barg) at various specified flow rates was fed into an ultrasonic nebulizer, and the generated droplets were carried out in the form of a fine aerosol (see Figure 4.2 for schematic of the experimental apparatus). This aerosol was subsequently led into a silica-gel drier, and then into a heated aerosol reactor resulting in a fine particle laden aerosol. These fine particles were continuously collected on the collection filter whose housing was maintained at 60 °C to prevent condensation of water. The entire system was operated under constant flow conditions maintained with the help of a membrane pump placed at the end of the collection filter. The powder collected on the filter paper was scraped off for use in further characterization.

Characterization

Nitrogen adsorption-desorption isotherms were measured on a Quantachrome Autosorb-6B sorption analyzer at 77 K. Prior to the isotherm measurements, the samples were vacuum degassed at 150 °C overnight. Scanning electron microscopy (SEM) images were obtained using a JEOL JSM 6500F electron microscope. Transmission electron micrographs (TEM) were recorded using a Philips CM30T electron microscope with a LaB_6 filament as the electron source, operated at 300 kV. A small amount of sample was dispersed in ethanol and samples were mounted on a microgrid carbon polymer, which was fixed on a copper grid.

Results and Discussion

A stable colloidal silica nanoparticle suspension (Ludox SM-30) with average particle size of 7 nm was obtained from Sigma Aldrich. The precursor solution was prepared by diluting the colloidal silica nanoparticle solution with deionized water to concentrations of 0.1 or 1.0 mol/l before spraying.

The experimental conditions and the results of the experiments are given in Table 1. The properties of the products obtained by spray drying the colloidal nanoparticle solution are also given in Table 1.

Table 1: Textural properties of particles produced from spray dried colloidal solutions

S. No.	Conc.	Q$_{air}$	Furnace temperature setpoints [°C]			Textural properties		
	[mol/l]	[l/min]	Zone 1	Zone 2	Zone 3	S_{BET} [m^2/g]	V_t [cm^3/g	d_{BJH} [nm]
NS-1	1.0	2.0	200	200	200	133	0.27	8.3
NS-2	1.0	2.0	200	200	200	130	0.26	8.2
NS-3	0.1	2.0	100	150	200	262	0.36	-
NS-4	0.1	1.5	100	150	200	197	0.30	-
NS-5	0.1	1.0	100	150	200	272	0.32	-

It can be seen from Table 1 that the values of the BET surface area, the total pore volume, and the BJH pore size of samples NS-1 and NS-2 are in good agreement indicating good reproducibility of the results.

Using a precursor concentration of 1.0 mol/l and fixing the furnace temperature at 200 °C resulted in particles with a BET surface area of 133 m^2/g and a total pore volume of 0.27 cm^3/g.

Figure 1 shows the pore size distribution of NS-1 obtained by applying the BJH model to the adsorption branch of the isotherm, which indicated the presence of a uniform pore network with a BJH pore size of 8.3 nm. This pore size can be attributed to the interparticle spacing due to the close packing of the individual nanoparticles. Additionally, the desorption branch of the nitrogen adsorption indicates that the internal pore structure is accessible to the surface through a narrower pore window.

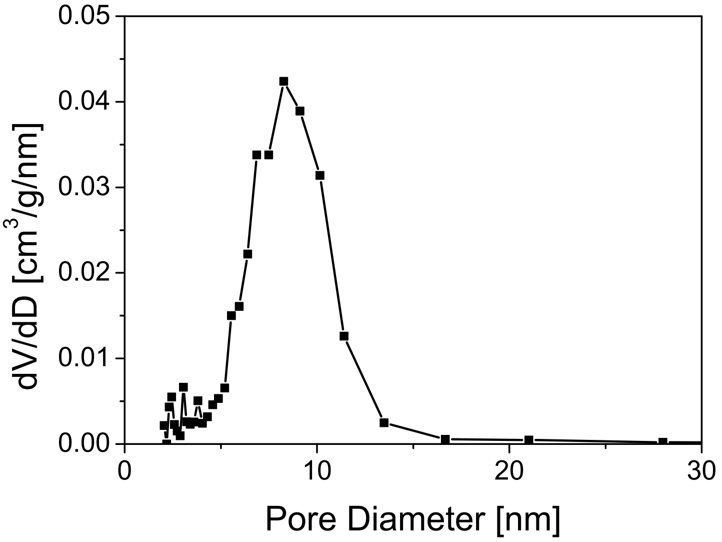

Figure 1: Pore size distribution of NS-1

The concentration of the solution was reduced to 0.1 mol/l to reduce the overall spray dried particle size. This resulted in an increase in BET surface area of the final products to 262 m^2/g (NS-3) and slight increase in the pore volume to 0.36 cm^3/g at similar experimental conditions. Additional experiments were performed by varying the carrier gas (air) flow rate. Decreasing

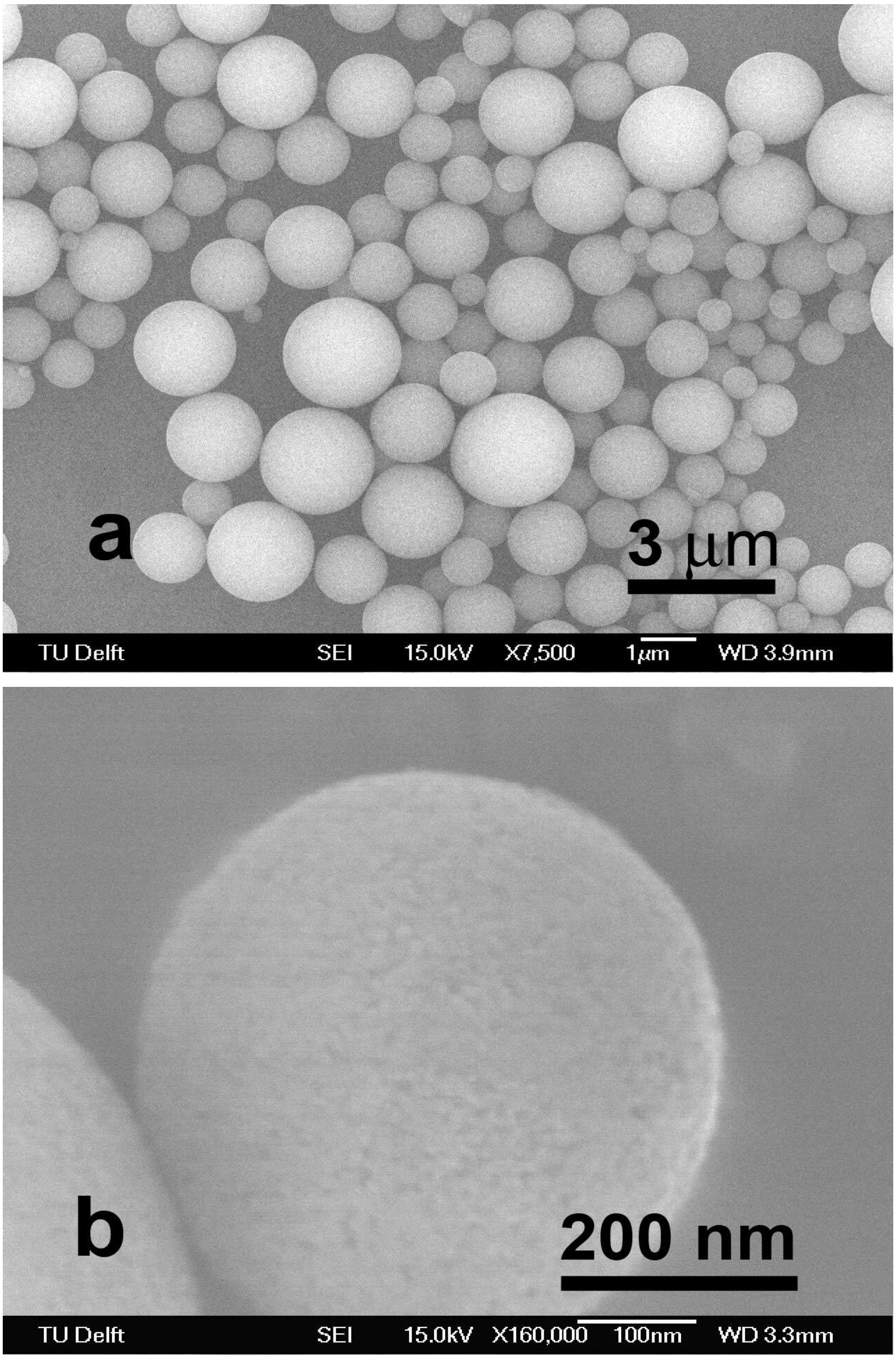

Figure 2: (a) and (b) SEM images of sample NS-1

the flow rate from 2.0 to 1.5 l/min results in a decrease in BET surface area from 262 m^2/g to 197 m^2/g, but then again increases to 272 m^2/g with further decrease in the flow rate to 1.0 l/min. A similar trend is also observed with the total pore volume of the products. Compared to NS-1, the samples synthesized using a low precursor concentration (NS-3 to NS-5), do not possess a uniform pore network, and instead contain a much broader pore size distribution. This

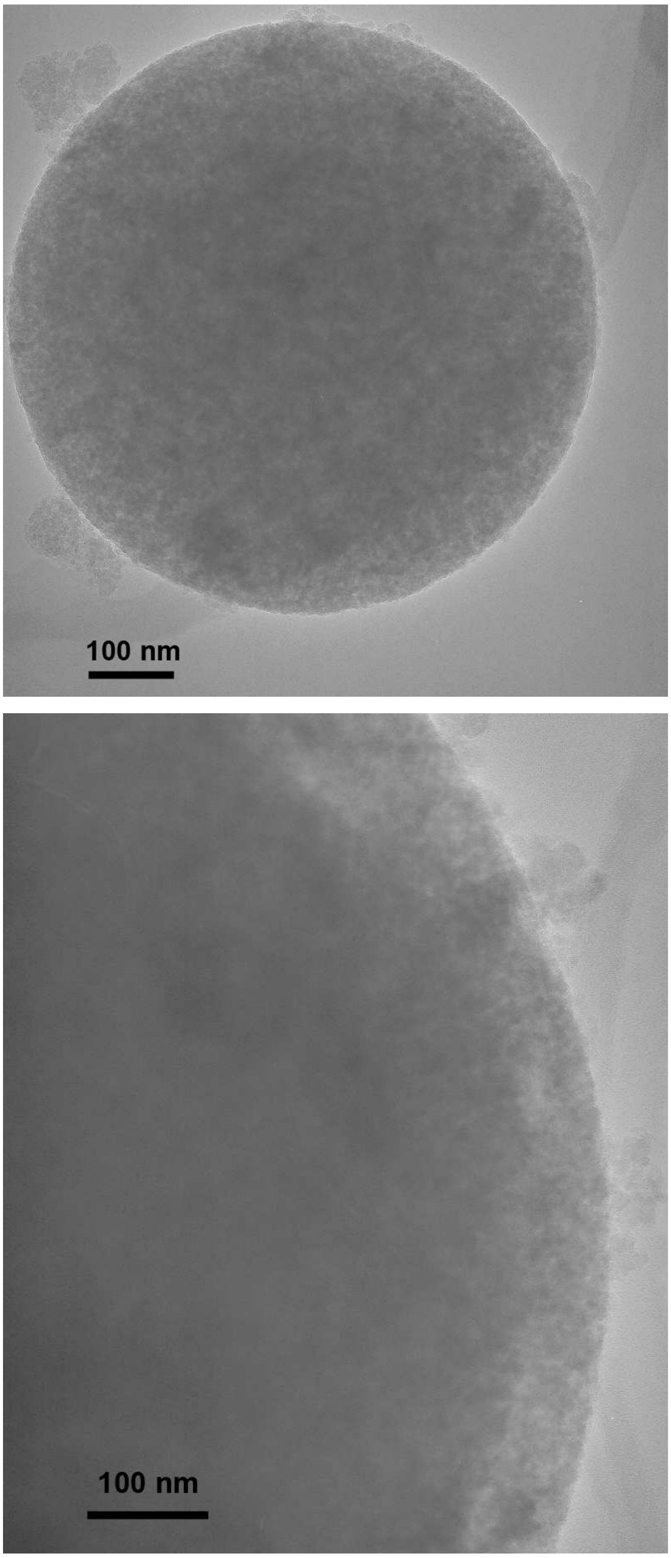

Figure 3: (a) and (b) TEM images of NS-1

may be due to the low density of the agglomerates as a result of a relatively smaller number of particles forming the packing, and leading to a not so well defined pore structure.

The morphology of the agglomerated particles can be seen from SEM images (Figure 2). The particles are mostly spherical in nature with a fairly smooth morphology. This is due to the spherical nature of the droplets, which, on evaporation, each produce particles with the same shape. The size of the produced particles varies from the submicron range to a couple of microns. A size distribution in the final product is observed due to the distribution of droplets generated from the nebulizer. Figure 2b shows the agglomeration of the particles resulting from close packing of primary silica nanoparticles held together by weak Van der Waals forces. Such a close packing leads to the pore network properties measured by nitrogen adsorption. Additionally, the silica surface might contain isolated hydroxyl groups, which, during evaporation, would condense by dehydration, further cross-linking the surface in the form of -Si-O-Si- bonds.

TEM images of a single particle from sample NS-1 are shown in Figure 3. It is hard to clearly see the internal pore structure, due to the thickness of the particles and their irregular internal structure. Figure 3b suggests a concentric thin layer (lighter region) surrounding the comparatively dense inner core (darker region) of the particles, resulting from a relatively lower number of particles contributing to the outer region of the spherical particle, as compared to the inner regions where more particles occupy the available space.

The ultrasonic nebulizer was successfully used to generate aerosols from nanoparticle silica solutions to eventually produce nanoparticle agglomerates with enclosed porosity.

References

1. F. Iskander, L. Gradon, K. Okuyama, J. Colloid & Interface Sci. 265 (2003) 296.
2. K. Master, Spray drying handbook, 5th edn., Longman London (1991).
3. A. D. Maskara, M. Smith, J. Am Ceram. Soc. 80 (1997) 1715.
4. F. Iskander, I. W. Lenggoro, B. Xia, K. Okuyama, J. Nanoparticle Res. 3 (2001) 263.
5. K. Ohshima, K. Tsuto, K. Okuyama, N. Tohge, Aerosol Sci Technol. 19 (1993) 468.
6. C. du Fresne von Hohenesche, K. K. Unger, T. Eberle, J. Mol. Catalysis A : Chemical 221 (2004) 185.
7. F. Iskandar, W. Lenggoro, T.O. Kim, N. Nakao, M. Shimada, K. Okuyama, J. Chem Engg. Japan 34 (2001) 1285.

Appendix B
Matlab program code for generating contour plots for BET surface area

```
Main_BET_Area.m

%Sri Arunachala Shiva
%Sri Narayana Namaha
%BET Surface Area
close all
clear all
clc

%Regression equation
%f = a0 + a1*x1 + a2*x2 + a3*x3 + a4*x4 ...
%       + a11*x1.^2 + a22*x2.^2 + a33*x3.^2 + a44*x4.^2 ...
%       + a12*x1.*x2 + a13*x1.*x3 + a14*x1.*x4 + ...
%       + a23*x2.*x3 + a24*x2.*x4 + a34*x3.*x4;

%Coefficients
%a0  = a(1); a1 = a(2); a2 = a(3); a3 = a(4); a4 = a(5);
%a11 = a(6); a22 = a(7); a33 = a(8); a44 = a(9);
%a12 = a(10); a13 = a(11); a14 = a(12);
%a23 = a(13); a24 = a(14); a34 = a(15);

%Coefficients_Regression1_R2=0.954
a(1)=454.44; a(2)=-25059.23; a(3)=0.928; a(4)=-12.71; a(5)=-3.16;
a(6)=1524017; a(7)=-1.17e-4; a(8)=0.322; a(9)=0.122;
a(10)=-34.36; a(11)=-170.78; a(12)=221.98;
a(13)=-4.78e-3; a(14)=-5.09e-3; a(15)=-5.32e-2;

%Constant values
%x1 = P123/TEOS , x2 = T  [-],
%x3 = H2O/TEOS [-], x4 = EtOH/TEOS [-]
x10=0.0095; x20=310; x30=10.1; x40=25.6;
```

```
x1min = 0.008; x1max = 0.02; x1d = 0.0002;
x1range = [x1min:x1d:x1max];
x2min = 100;   x2max = 350;  x2d = 50;
x2range = [x2min:x2d:x2max];
x3min = 5;     x3max = 40 ; x3d = 1;
x3range = [x3min:x3d:x3max];
x4min = 0;     x4max = 25  ; x4d = 1;
x4range = [x4min:x4d:x4max];

%Different Contour plots

%For  x = P123/TEOS [-], y = T [deg C]
x3 = x30;
x4 = x40;
[x1,x2] = meshgrid(x1range,x2range);
z = RegressEqn(a,x1,x2,x3,x4);
[C,h] = contour(x1,x2,z);
set(h,’ShowText’,’on’,’TextStep’, ...
get(h,’LevelStep’)*2,’LineColor’,’k’)
clabel(C,h,’FontSize’,10,’Rotation’,0,’LabelSpacing’,250)
colormap cool
xlim([x1min x1max])
ylim([x2min x2max])
title([’H_2O/TEOS [-] = ’,num2str(x30), ...
’, EtOH/TEOS [-] = ’,num2str(x40)])
xlabel(’P123/TEOS [-]’)
ylabel(’T [ˆoC]’)
text(0.01,240, ’S_{BET} [mˆ2/g]’)
hold on

%For  x = P123/TEOS [-], y = H2O/TEOS
x2 = x20;
x4 = x40;
[x1,x3] = meshgrid(x1range,x3range);
figure
z = RegressEqn(a,x1,x2,x3,x4);
[C,h] = contour(x1,x3,z,[300:50:500]);
%[450 600 355 377 406 487 500 550 600]
set(h,’ShowText’,’on’,’TextStep’,...
get(h,’LevelStep’)*2,’LineColor’,’k’)
clabel(C,h,’FontSize’,10,’Rotation’,0,’LabelSpacing’,300)
colormap cool
xlim([x1min x1max])
ylim([x3min x3max])
title([’T [ˆoC] = ’,num2str(x20),’,...
EtOH/TEOS [-] = ’,num2str(x40)])
```

```
xlabel('P123/TEOS [-]')
ylabel('H_2O/TEOS [-]')
%text(0.012,25, 'S_{BET} [m^2/g]')
hold on

%For  x=P123/TEOS, y=EtOH/TEOS
x2 = x20;
x3 = x30;
[x1,x4] = meshgrid(x1range,x4range);
figure
z = RegressEqn(a,x1,x2,x3,x4);
[C,h] = contour(x1,x4,z,[300:100:1000, 1000:200:1800]);

set(h,'ShowText','on','TextStep',...
get(h,'LevelStep')*2,'LineColor','k')
clabel(C,h,'FontSize',10,'Rotation',0,'LabelSpacing',250)
colormap cool
xlim([x1min x1max])
ylim([x4min x4max])
title(['T [^oC] = ',num2str(x20),',...
H_2O/TEOS [-] = ', num2str(x30)])
xlabel('P123/TEOS [-]')
ylabel('EtOH/TEOS [-]')
text(0.015,25, 'S_{BET} [m^2/g]')
hold on

%For  x = T [deg C],y = H2O/TEOS
x1 = x10;
x4 = x40;
[x2,x3] = meshgrid(x2range,x3range);
figure
z = RegressEqn(a,x1,x2,x3,x4);
[C,h] = contour(x2,x3,z);

set(h,'ShowText','on','TextStep',...
get(h,'LevelStep')*2,'LineColor','k')
clabel(C,h,'FontSize',10,'Rotation',0,'LabelSpacing',250)
colormap cool
xlim([x2min x2max])
ylim([x3min x3max])
title(['P123/TEOS [-] = ',num2str(x10),',...
EtOH/TEOS [-] = ', num2str(x40)])
xlabel('T [^oC]')
ylabel('H_2O/TEOS [-]')
text(200,25, 'S_{BET} [m^2/g]')
hold on
```

```
%x2 = T [deg C], x4 = EtOH/TEOS [-]
%For  x=x2,y=x4
x1 = x10;
x3 = x30;
[x2,x4] = meshgrid(x2range,x4range);
figure
z = RegressEqn(a,x1,x2,x3,x4);
[C,h] = contour(x2,x4,z);

set(h,’ShowText’,’on’,’TextStep’,...
get(h,’LevelStep’)*2,’LineColor’,’k’)
clabel(C,h,’FontSize’,10,’Rotation’,0,’LabelSpacing’,250)
colormap cool
xlim([x2min x2max])
ylim([x4min x4max])
title([’P123/TEOS [-] = ’,num2str(x10),’,...
H_2O/TEOS [-] = ’, num2str(x30)])
xlabel(’T [ˆoC]’)
ylabel(’EtOH/TEOS [-]’)
text(300,15, ’S_{BET} [mˆ2/g]’)
hold on

%3D Contours
figure
contour3(x2,x4,z)
surface(x2,x4,z,’EdgeColor’,[.8 .8 .8],’FaceColor’,’none’)
grid off
view(-15,25)
colormap cool
hold on

%For  x = H2O/TEOS, y = EtOH/TEOS
x1 = x10;
x2 = x20;
[x3,x4] = meshgrid(x3range,x4range);
figure
z = RegressEqn(a,x1,x2,x3,x4);
[C,h] = contour(x3,x4,z);

set(h,’ShowText’,’on’,’TextStep’,...
get(h,’LevelStep’)*2,’LineColor’,’k’)
clabel(C,h,’FontSize’,10,’Rotation’,0,’LabelSpacing’,250)
colormap cool
xlim([x3min x3max])
ylim([x4min x4max])
```

```
title([’P123/TEOS [-] = ’,num2str(x10),’,...
T [ˆoC] = ’,num2str(x20)])
xlabel(’H_2O/TEOS [-]’)
ylabel(’EtOH/TEOS [-]’)
text(25,15, ’S_{BET} [mˆ2/g]’)
hold on
```

RegressEqn.m

```
function f = RegressEqn(a, x1, x2, x3, x4)

%x1 = X(:,1); x2 = X(:,2); x3 = X(:,3); x4 = X(:,4);

a0  = a(1); a1 = a(2); a2 = a(3); a3 = a(4); a4 = a(5);
a11 = a(6); a22 = a(7); a33 = a(8); a44 = a(9);
a12 = a(10); a13 = a(11); a14 = a(12);
a23 = a(13); a24 = a(14); a34 = a(15);

f = a0 + a1*x1 + a2*x2 + a3*x3 + a4*x4 ...
       + a11*x1.ˆ2 + a22*x2.ˆ2 + a33*x3.ˆ2 + a44*x4.ˆ2 ...
       + a12*x1.*x2 + a13*x1.*x3 + a14*x1.*x4 + ...
       + a23*x2.*x3 + a24*x2.*x4 + a34*x3.*x4;
```

Samenvatting

Aerosol Gebaseerde Synthese van Nanogestructureerd Silica

Ondanks de vele toepassingen van zeolieten, in het bijzonder als krakingskatalysator, is er een duidelijke behoefte om de diffusie van vooral grotere moleculen in deze materialen te versnellen. Het diffusieprobleem is het gevolg van de kleine poriegrootte van de kristallijne aluminosilicaten. Dit heeft geleid tot de ontdekking van geordende mesoporeuze silica's met grotere mesoporiën, waarvan de poriegrootte op een gecontroleerde wijze gevarieerd kan worden. Zij worden daarom soms beschouwd als ideale, rationeel ontwerpbare katalysatordragers. Zij hebben dan ook veel aandacht getrokken van de wetenschappelijke gemeenschap, vanwege veelzijdige toepassingen als katalysatoren, sensoren, materialen met een lage diëlektrische constante, optische golfdragers en microstromingsapparaten.

De eerste hoofdstukken van dit proefschrift (Hoofdstuk 1 en 2) betreffen de sol-gel synthese van nanogestructureerde SBA-15 materialen met hexagonaal geordende grote mesoporiën. Deze materialen hebben door de grotere wanddikte van de porin een betere thermische stabiliteit in de aanwezigheid van water dan MCM-41. Verscheidene materialen met unieke morfologie werden gesynthetiseerd door het variëren van een enkele parameter, namelijk de roersnelheid, tijdens de synthese in aanwezigheid van een zwak zuur, $\mathrm{H_3PO_4}$. Onder statische condities wordt een dunne film materiaal verkregen op het lucht-water grensvlak, terwijl zich op de bodem een hiërarchische poreuze cake vormt met meso- en macroporiën, bestaande uit dichtgepakte deeltjes. Wanneer langzaam geroerd wordt, vormen zich bundels met een lengte van enige honderden micrometers en een dikte van minimaal 50 micrometer. Deze bundels bestaan uit lange draden, welke aan elkaar gehecht zijn. Materialen welke gemaakt zijn onder krachtig roeren, vertonen een vezelachtige morfologie en nadere studie laat zien dat de fibers opgebouwd zijn uit individuele segmenten. Alle materialen zijn geordend op nanoschaal en hebben een hoog specifiek BET oppervlak, zoals bevestigd met respectievelijk XRD en stikstofadsorptie metingen. Transmissie elektronen microscopie (TEM) opnamen van een doorgesneden sectie van de dunne laag tonen aan dat de kleine kanalen parallel aan het oppervlak lopen. Het is daarnaast interessant dat de bundels blijken opgebouwd te zijn uit kleine kanalen welke parallel aan de lange as georiënteerd zijn. De verschillende afschuifspanningen welke optreden tijdens de verschillende roercondities beïnvloeden de vorm en de aggregatie van de micellen, alsook de groei van de mesoporeuze fase aan het silica-surfactant grensvlak. Hierdoor worden verschillende morfologieën verkregen. De aanwezigheid van fosfor in de gecalcineerde SBA-15 materialen, zoals aangetoond met XRF analyses, is verantwoordelijk voor betere Brønsted-zure eigenschappen. Dit maakt deze materialen veelbelovende heterogene katalysatoren voor processen waarin Brønsted-zure eigenschappen vereist zijn.

PFG-NMR metingen uitgevoerd aan de SBA-15 vezels en bundels geven beter inzicht in de diffusie-eigenschappen van deze materialen. De verplaatsing van nitrobenzeen in de mesoporeuze bundels kan goed worden beschreven door een model met constante diffusiviteit. Dit betekent dat over de waargenomen verplaatsing van 4 μm in de lengterichting, de moleculaire verplaatsing niet wordt gehinderd door transportbeperkingen. De kanalen zijn deels doorlaatbaar, wat in overeenstemming is met het feit dat de wand van de SBA-15 mesoporiën microporeus is. In de bundels blijkt de verplaatsingssnelheid loodrecht op de lengterichting van de kanalen toe te nemen bij langere analysetijd. Dit suggereert de afwezigheid van een perfecte poriestructuur over afstanden van 1 μm, waardoor verplaatsingen loodrecht op de lengterichting van de kanalen wordt gestimuleerd. In de vezels blijkt de diffusie in beide gevallen in geringe mate af te nemen met toenemende analysetijd, wat duidt op een vertraagde verplaatsing over grotere afstanden. Dit is in tegenstelling tot de waarnemingen in de bundels. Er is een duidelijke correlatie met de morfologie van de vezels, welke opgebouwd zijn uit korte segmenten waardoor insluiting optreedt in een kleinere ruimte dan in de bundels.

Synthese van silica's met een ordening op “meso-niveau” vindt meestal plaats via de sol-gel techniek, waarbij enkele dagen benodigd zijn om het uiteindelijke gestructureerde product te verkrijgen. Een alternatieve, recentere wijze van synthetiseren is zelfassemblage via verdamping van aerosolen (EISA). Deze techniek maakt de continue productie van poreuze silica deeltjes met een controleerbare morfologie en poriegrootte in slechts enkele seconden mogelijk. Een apparaat is ontworpen en gebouwd bestaande uit een vernevelaar welke kleine aerosoldeeltjes produceert, welke door een verwarmde buisoven worden getransporteerd, waarbij de deeltjes worden gevormd. Het eindproduct wordt verzameld op een membraanfilter. In dit type experimenten is er een groot aantal veranderlijken dat de uiteindelijke eigenschappen van het product mogelijk beïnvloedt. De vraag is vervolgens welke (combinatie van) variabelen tot welke morfologie leiden en welke de grootste invloed hebben? Om deze variabelen te onderzoeken is een nauwkeurige statistische methodologie toegepast, waardoor het aantal experimenten sterk kan worden teruggedrongen. Een heldere, homogene zure oplossing bestaande uit een organosilicaat (TEOS) en een drie-blok copolymeer (P123) als templaat wordt geatomiseerd tot een aërosol, dat vervolgens door de verwarmde oven wordt getransporteerd, zoals hierboven beschreven is. Silica en micellen, opgebouwd uit oppervlakte actieve stof, ondergaan een zelfassemblageproces waarbij gelijktijdige hydrolyse en condensatie van TEOS optreedt. Dit resulteert in een organisch-anorganisch composiet. Calcinering bij hoge temperatuur leidt tot nanoporeuze silica deeltjes met een gelaagde of hexagonale structuur. De experimenten zijn gebaseerd op een factorial design methode, voor een meer gedetailleerde studie naar de effecten van de samenstelling van de beginoplossing en reactortemperatuur op de uiteindelijke eigenschappen van het gesynthetiseerde materiaal. Deze methode maakt het mogelijk om gelijktijdig de invloed van verschillende variabelen te onderzoeken. Dit heeft grote voordelen ten opzichte van de traditionele wijze van experimenteren aan dit type materialen, waarbij slechts één variabele per keer gewijzigd wordt. Hierdoor wordt het mogelijk om een groter bereik aan experimentele condities te onderzoeken om op die manier de werkelijke trends (universeel of lokaal) te belichten welke vaak aan misinterpretatie onderhevig zijn in de conventionele wijze van experimenteren. Deze benadering heeft aangetoond dat de volgende variabelen significant zijn: P123/TEOS blijkt een maximaal effect te hebben op het specifiek BET oppervlak, gevolgd door H_2O/TEOS, temperatuur en EtOH/TEOS. P123 en ethanol hebben ook een belangrijk gecombineerd effect. De temperatuur heeft in vergelijking met andere variabelen een maximale invloed op het poriënvolume. Het gebruik van contours heeft geleid tot de identificatie van meerdere condities voor het verkrijgen van een benodigd specifiek oppervlak en poriënvolume. N_2 adsorptie-experimenten laten zien dat een hoge P123/TEOS verhouding leidt tot deeltjes met een brede poriëndistributie. Lagere verhoudingen bevorderen de vorming van een netwerk met uniforme poriëngroottes. De ordening van de nanostructuur is opgehelderd met behulp van röntgendiffractie (XRD) en transmissie elektronenmicroscopie (TEM). Bij materialenonderzoek blijkt de synthese vaak te bestaan uit een aantal stappen met verschillende experimentele variabelen welke ieder geoptimaliseerd dienen te worden om het gewenste product te verkrijgen. Dit wordt vaak uitgevoerd via een arbeidsintensieve, zogenaamde ‘trial and error’ aanpak. Door gebruik te maken van de hier beschreven technieken kan men het aantal variabelen identificeren en minimaliseren, of combinaties van variabelen vinden welke een significant effect hebben op de eigenschappen van het onderzochte materiaal. Deze informatie kan vervolgens gebruikt worden als basis voor vervolgexperimenten om de kwaliteit van het materiaal te verbeteren, door deze variabelen te optimaliseren. Bovendien kunnen de afgeleide empirische gegevens dienen als basis voor het verder begrip en de modellering van een complex proces zoals EISA.

Een grote sproeidroger bij Albemarle Catalysts is gebruikt om nieuwe mesoporeuze silica en silica-alumina materialen te synthetiseren via zelfassemblage van silica en alumina deeltjes, waarbij P123 als structuurvormer is gebruikt. Dit proces leidt tot een amorf materiaal dat opgebouwd is uit gepakte silica en alumina nanodeeltjes. We hebben laten zien dat de poriëngrootte van deze materialen voornamelijk wordt bepaald door de hoeveelheid structuurvormer en dat de grootte *onafhankelijk* is van de silica-alumina verhouding van de materialen. Stabiliteitstesten bij extreme condities (100% stoom en een temperatuur van 788 °C gedurende 20 uur) toonden aan dat de gesynthetiseerde mesoporeuze materialen hun mesoporeuze structuur grotendeels behouden. Dit is duidelijk beter dan de kristallijne mesoporeuze aluminosilicaten welke gewoonlijk in de literatuur worden beschreven. Katalytische activiteitstesten, gebaseerd op de conversie van tri-isopropyl benzeen (TiPB) hebben aangetoond dat de activiteit van de materialen afhankelijk is van de silica/alumina verhouding. Blijkbaar kan, door gebruik te maken van nanobouwstenen bestaande uit silica en boehmiet, de activiteit van het oppervlak ten aanzien van TiPB aangepast worden. Deze resultaten bieden nieuwe perspectieven voor de synthese van krakingskatalysatoren, aangezien de katalytische activiteit blijkbaar ontkoppelbaar is van de poriegrootte. Een structuurvormer (bijv. P123 in dit onderzoek, maar ook andere kunnen worden gebruikt) kan worden toegepast om de mesoporiëngrootte aan te passen, terwijl de activiteit kan worden beïnvloed door de silica/alumina verhouding te veranderen. Met deze techniek kan de toegankelijkheid van de katalysator en de reactiviteit van het oppervlak onafhankelijk worden ontworpen om op deze wijze tegemoet te komen aan de eisen van een specifieke voeding. Het is zeker de moeite waard om deze templaatmoleculen, gekoppeld aan industriële silica en alumina basismaterialen, te onderzoeken. De toegepaste silica/alumina verhouding blijkt ook de activiteit te beïnvloeden. We speculeren dat dit wordt veroorzaakt door de vorming van katalytisch actieve silica-alumina materialen op het grensvlak waar de silica en alumina deeltjes elkaar raken. Het is waarschijnlijk lonend om verschillende beschikbare industriële bronnen van silica en boehmiet te onderzoeken om zo hun effect op de reactiviteit van de gesynthetiseerde materialen vast te stellen.

Tot slot is een aanzet gemaakt om via een aërosolmethode composieten te synthetiseren bestaande uit zeoliet nanokristallen verankerd in een mesoporeus rooster. Dit omvat eerst de synthese van de precursor bestaande uit ZSM-5 nanokristallen welke in een waterige oplossing zijn gedispergeerd. Indien deze suspensie samen met een P123 oplossing wordt verneveld, leidt dit tot een insluiting van de nanokristallen in het mesoporeuze rooster. De gesynthetiseerde composieten bevatten grote mesoporiën van ca. 30 nm met een relatief brede distributie en een hoog poriënvolume van 1.0 cm^3/g. Röntgendiffractiepatronen bevestigen de aanwezigheid van ZSM-5 eenheden in de composietmaterialen. Dit zou een sterke afname in diffusielimitaties moeten opleveren. Deze materialen met een verbeterde toegankelijkheid, gecombineerd met de zure eigenschappen van ZSM-5 kristallen, zullen serieuze kandidaten zijn om grotere moleculen te kraken.

Dit proefschrift laat zien dat de aërosolmethode de synthesetijd van interessante mesoporeuze materialen en zeoliet/mesoporeuze composieten in vergelijking met de traditionele sol-gel syntheseroute sterk verkort. Een homogene startoplossing, of een gedispergeerde suspensie, kan worden gebruikt om in enkele seconden een brede verzameling aan materialen te produceren. Het is zeker waardevol om in meer detail de synthese van mesoporeuze ZSM-5 composieten te bestuderen door de Si/Al verhouding te variëren en de zuurgraad van het mesoporeuze netwerk te sturen, toegespitst op de vereiste toepassingen.

Acknowledgements

I would first and foremost like to express my deep sense of gratitude to my supervisors Prof. Marc-Olivier Coppens and Prof. Andreas Schmidt-Ott for giving me the opportunity to pursue a Ph.D. research under their able guidance. I had been to TU Delft a couple of times (during the summer) in the years preceding the onset of my Ph.D. research and during one of those visits had the privilege to work under Prof. Schmidt-Ott on aerosol production of metal nanoparticles. I thoroughly enjoyed it and expressed my interest to do a Ph.D. under him. It was my good fortune that the next year (2003), I was offered to do a collaborative project under both Prof. Coppens and Prof. Schmidt-Ott on using aerosols to make nanostructured materials. And so the journey began. I have to say that it has been a wonderful four years. The numerous discussions we had evidently showed the passion you share for science and I hope it rubbed off on me. You have been pillars of formidable knowledge, yet kind friends, philosophers and guides to students like me. Prof. Coppens, by your own driving effort, persistent research and inexhaustible patience, and your own characteristic genius, you have carved a niche for yourself as a remarkable world renowned scientist. You taught me how to write good publications through your numerous and patient revisions. You gave me freedom in finding my own way but at the same time kept me focused on the task at hand. I am thankful to you for keeping faith in me and your constant guidance and encouragement helped me to overcome the obstacles that one encounters during a Ph.D. You have both been the ideal supervisors, any Ph.D. student can hope for and thank you for making my Ph.D. experience a memorable one.

I would like to acknowledge our industrial sponsor, Albemarle Catalysts B.V., and our co-sponsors, NWO (via a CW/PIONIER grant) and Delft University of Technology for providing the financial support. Financial support for the PFG-NMR studies (at the University of Leipzig) by the European Community (NoE INSIDE PORES) as well as by DFG and NWO (International Research Training Group Diffusion in Porous Materials) is also gratefully acknowledged.

I would like to sincerely thank Prof. Jörg Kärger from the University of Leipzig, Germany for taking a keen interest in the nanostructured materials I synthesized and analyzing my samples using PFG NMR to quantify diffusion in the materials. I would also like to acknowledge his students- Sergej Naumov and Rustem Valiullin for conducting the experiments and discussions regarding the same.

Characterization of the materials I synthesized was crucial for my thesis and I could not have accomplished without the help and support of a number of people.
I am deeply grateful to Prof. Henny Zandbergen for providing access to the TEM facilities in his group. I wish to express my profound thanks to Dr. Frans D. Tichelaar for teaching me to use the TEM and his tremendous patience in answering my countless questions regarding the instrument and material characterization. I would like to also thank Dr. Patricia J. Kooyman

and Dr. Charlie Peet for help with the TEM analysis, and Dr. Ulrike Ziese for the beautiful 3-D TEM images that gave us exciting new insights into the pore structure.
I sincerely thank Dr. Johan C. Groen and Sander Brouwer for the N_2 adsorption measurements and the extensive discussions on the same. I would like to also thank Dr. Eduardo Mendes, Niek van der Pers and Pascal Visser for the XRD measurements, Joop Padmos for the XRF measurements, and Kees Kwakernaak, Han Kiersch and Hans Brouwer for the SEM analysis.

I wish to express my gratitude and thank our collaborators at Albemarle Catalysts B.V., Amsterdam - Dr. Johan J. Heiszwolf, Dr. Bart de Graaf, Dr. Leen Gerritsen and Dr. Erik LaHeij for their valuable inputs during the numerous project meetings. I would like to thank them also for arranging the use of lab facilities at Albemarle to synthesize interesting materials, which added an industrial perspective to my work. At Albemarle, I would like to thank Gesina Hoogsteen, André Riezebeek for helping in the lab, Ljiljana Becin for conducting the N_2 adsorption measurements, Dennis Hamstra for the steaming experiments, and Pieter Schreuder and Robert Jonker for the probe molecule pulse test experiments.

Dr. Wenjiang Li, you introduced me to SBA-15 and thank you for helping in the first years in familiarizing with nanostructured materials. I thoroughly enjoyed working with you and admire your instinct for Chemistry, especially in regard to synthesis. A special thanks to Dr. Christian Peineke for all the help in the Nanolab, answering my frequent questions on experimentation inspite of his trademark opening sentence “I don’t know”. Dr. Michael A. Stowers, thank you for your useful advice for developing the aerosol generator and the aerosol reactor. I would like to thank Dr. Johan Groen for his invaluable help and patience in translating the thesis summary and propositions.

Along the way I guided a few students - Claire Tange and Thiebaud. Thank you for your dedication and I had a pleasure being your supervisor.

I wish to sincerely thank Dr. Jan C.M. Marijnissen for giving me access to the aerosol generator and Laser aerosol particle sizer. I would like to thank Dr. Eduardo Mendes, Prof. Stefan Luding, Prof. Jacob A. Moulijn and Dr. Gabriel M.H. Meesters for their support and co-operation.

I would like to express my deep sense of gratitude to the committee members - Prof. Abdelhamid Sayari, Prof. Krijn de Jong, Prof. Freek Kapteijn, Dr. Johan J. Heiswolf, Dr. Jan C.M. Marijnissen and Prof. Stephen Picken for their comments and valuable suggestions which helped me in polishing the thesis. I would like to also thank Prof. Ernst Sudhölter for the valuable discussions on my Ph.D. work.

I would like to specially acknowledge the DelftChemTech Workshop for their excellent services and kind help in constructing my experimental setup - Alex Ploegman, Nico Alberts and Alex Boot. I used to come with just rough sketches and you would readily translate them into reality in an incredible short amount of time. Henk Lukas from the glass workshop as well, for his help in constructing the aerosol reactor.

To all the supporting staff- Nico van Westen, Gerard de Vos, Piet Droppert, and Ben Norder, thank you for your help. I wish to thank the systems group - Ricardo vd Bos, Arno Haket and Bart Boshuizen for their help regarding computer and network issues. I would like to acknowledge the administrative staff - Peggy Stevens, Fieneke Spaans, Mieke Jacobs, Wil Stolwijk and Karin Wilhelm for their help regarding administrative matters.

It was a pleasure working at the PCMT group and would like to thank the present and former group members for their help and co-operation - Dr. Wenjiang Li, Dr. Charlie Peet, Wang Jia, Wang Gang, Dr. Dana O. Christensen, Dr. David Newsome, Vijay Iyengar, Prasant K. Samantaray, Dr. Kourosh Malek, Irina & Dr. Stefan Gheorghiu, Dr. Ton Dammers, Dr. Veronica R. Lupascu and Dr. Alex Kononov, to name a few.

It was equally wonderful being a part of the NSM group and I enjoyed interacting, working with all of you - Dr. Michael A. Stowers, Dr. Christian Peineke, Vincent Vons, Jan van Erven, Bas van Laarhoven, Ineke Kleefsman, Nooshin S. Tabrizi, Tomasz M. Trzeciak, Anna Hubacz, Ajay Galdhar, Nikhil D. Shindgikar, Maria Margarita Vivas, Orion J.P. Mouraille, Yonsuang Arnanthigo, Sjaak Verdoold, Dr. Micha-Klaus Mueller, Corrado Locati, Mario Valvo, Bart van der Graaf, Dr. Andrzej Pekalski and Dr. John F. Zevenbergen. Along the years, apart from discussing science, I enjoyed the BBQ's (which were always very well organized) and the "borrels" to unwind. Attending conferences as a group was always an enjoyable event and I had quite a number of memorable ones.

Lastly but never the least, I would like to thank my family. I would like to remember my late grandmother, a lady of poise and piety who taught me courage, fairplay, a deep sense of right and lessons of life that can hardly go wrong. Amma and Appa, you have both been the pillars of moral support and guidance throughout my life. I am extremely fortunate to have such wonderful parents who have taken such great care of me and have always been there to provide an endless supply of encouragement and support. Dear Amma, how can I forget the amount of time you have spent during my school days helping me learn, do my homework and instilling within me the drive to excel but at the same time not get disheartened by failure and instead use them to improve myself the next time. Dear Appa, you have not only been a great father but an excellent teacher. I owe my interest in chemical engineering, especially for particle technology to you. Right from school through my university days and till today, you have explained me the nuances of science and engineering in the most vividly imaginative ways that still enrapture me immensely. My dear brother, Dr. Ramanan Pitchumani, you have been more a friend than a brother. You have been an inspirational figure in my life and the person I could turn to in times of need. You are indeed a friend, in the truest form of the word. Your grasp of knowledge is amazing and you never hesitate to help me inspite of the tonnes of work you have on your hands. I don't know what I would have done without you- thanks a million for your help whether it was with solving complex math problems, programming, and especially for your extensive help in compiling my thesis into LaTeX. I have always cherished our endless talks on the phone and Skype and your encouraging words have helped me through my Ph.D. years. I hope I have not taken your selfless love and affection for granted for I miss all of you very much when you are not around.

Curriculum Vitae

Raghuraman Pitchumani is geboren op 7th June 1979 te Hyderabad, India.

1984-1990	Delhi Public School, East of Kailash, New Delhi, India
1990-1997	Delhi Public School, R.K. Puram Sector XII, New Delhi, India
1998-2002	Bachelor of Technology, Department of Chemical Engineering, Indian Institute of Technology, New Delhi, India
2002-2003	Master of Technology in Process Engineering and Design, Department of Chemical Engineering, Indian Institute of Technology, New Delhi, India
2003-2007	Ph.D. Research, Physical Chemistry & Molecular Thermodynamics and Nanostructured Materials, DelftChemTech, Faculty of Applied Sciences, Delft University of Technology, Delft, The Netherlands